Institute of Thermoelectricity, Academy of Sciences and Ministry of Education and Science of Ukraine

Journal of THERMOELECTRICITY

International Research

Founded in December, 1993

published 6 times a year

No. 5 *2014*

Editorial Board

International Editorial Board

Founders - National Academy of Sciences, Ukraine
Institute of Thermoelectricity of National Academy of Sciences and Ministry of Education and Science of Ukraine

Certificate of state registration № КВ 15496-4068 ПР

Editorial office manager O. Pugantseva

Approved for printing by the Academic Council of Institute of Thermoelectricity of the National Academy of Sciences and Ministry of Education and Science, Ukraine

Address of editorial office:
Ukraine, 58002, Chernivtsi, General Post Office, P.O. Box 86.
Phone: +(380-372) 90 31 65.
Fax: +(380-3722) 4 19 17.
E-mail: jt@inst.cv.ua
http://www.jt.inst.cv.ua

Signed for publication 25.11.14. Format 70×108/16. Offset paper №1. Offset printing.
Printer's sheet 11.1. Publisher's signature 9.2. Circulation 400 copies. Order 6.

Printed from the layout original made by "Journal of Thermoelectricity" editorial board
in the printing house of "Bukrek" publishers,
10, Radischev Str., Chernivtsi, 58000, Ukraine

CONTENTS

I.V.Hutsul, V.I.Hutsul

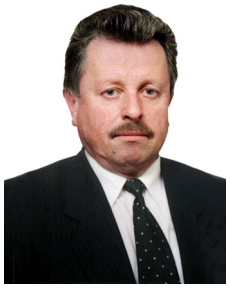

I.V. Hutsul

Yu.Fedkovych Chernivtsi National University
2, Kotsyubinsky Str., Chernivtsi, 58012 Ukraine

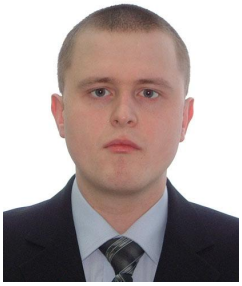

V.I. Hutsul

STUDY OF THE UNSTEADY-STATE DISTRIBUTION OF TEMPERATURE AND THERMOPOWER OF ANISOTROPIC OPTICAL THERMOELEMENT UNDER PARALLEL DIRECTIONS OF RADIANT FLUX AND TEMPERATURE GRADIENT

The solution of the inhomogeneous unsteady-state thermal conductivity equation under parallel directions of temperature gradient and radiant flux of $ZnAs_2$ anisotropic plate with regard to the Bouguer-Lambert law is presented, and the dependence of temperature distribution on coordinates and time is analyzed. The expressions for the transverse thermopower are obtained for the cases of optical transmission and surface absorption.

Key words: anisotropic medium, anisotropic optical thermoelement, thermostat, radiant flux, temperature gradient, transverse thermopower.

Introduction

The prospects of using anisotropic media with different optical transmission values for recording and conversion of high-intensity radiant fluxes give an impetus to a thorough study of their properties. One of the methods of electromotive force generation is a transverse thermoelectromotive force (thermopower). Despite the fact that this effect had been long ago studied by Thomson [1], it was not until nearly a century later that Samoilovich with colleagues succeeded in implementing this idea in the form of anisotropic thermoelement [2]. The absence of conventional junction, availability of only one section, mutual normality of heat flux and thermoelectric field determined their promising outlook and resulted in the appearance of new generations of various instruments and devices having no domestic and foreign equivalents [3-6]. At the present time there are sources whose energy is rather difficult to be recorded and converted by the existing methods. For this purpose, here we use media with different optical transmission values. Such media make it possible to convert the absorbed part of radiant energy by means of thermal pyrocalorimetric effects. Analysis shows that for radiant fluxes of UV, visible and IR regions implementation of this method offers the greatest promise for the case of using the transverse thermopower effect [1-5]. This resulted in the development of anisotropic optical thermoelements (AOT) [7]. The choice of specific AOT and the necessary operating modes is dictated by service conditions and is a function of parameters of materials employed, as well as of mutual directions of radiant and heat fluxes propagation with respect to selected crystallographic orientations of material.

Unsteady-state distribution of AOT temperature and thermopower

Let us consider AOT in the form of a rectangular plate of dimensions a, b, c (Fig. 1), made of material whose thermal conductivity coefficient χ and the Seebeck coefficient α in the laboratory

coordinate system (XYZ) rotated by an angle φ in XOY plane with respect to crystallographic plane (X′Y′Z′) are given by

$$\chi = \begin{vmatrix} \chi_{\parallel}\sin^2\phi + \chi_{\perp}\cos^2\phi & (\chi_{\parallel} - \chi_{\perp})\sin\phi\cos\phi & 0 \\ (\chi_{\parallel} - \chi_{\perp})\sin\phi\cos\phi & \chi_{\parallel}\cos^2\phi + \chi_{\perp}\sin^2\phi & 0 \\ 0 & 0 & \chi_{\perp} \end{vmatrix},$$
$$\alpha = \begin{vmatrix} \alpha_{\parallel}\sin^2\phi + \alpha_{\perp}\cos^2\phi & (\alpha_{\parallel} - \alpha_{\perp})\sin\phi\cos\phi & 0 \\ (\alpha_{\parallel} - \alpha_{\perp})\sin\phi\cos\phi & \alpha_{\parallel}\cos^2\phi + \alpha_{\perp}\sin^2\phi & 0 \\ 0 & 0 & \alpha_{\perp} \end{vmatrix}, \quad (1)$$

where, $\chi_{\parallel}$, $\chi_{\perp}$ and, $\alpha_{\parallel}$, $\alpha_{\perp}$ are tensor components χ and α.

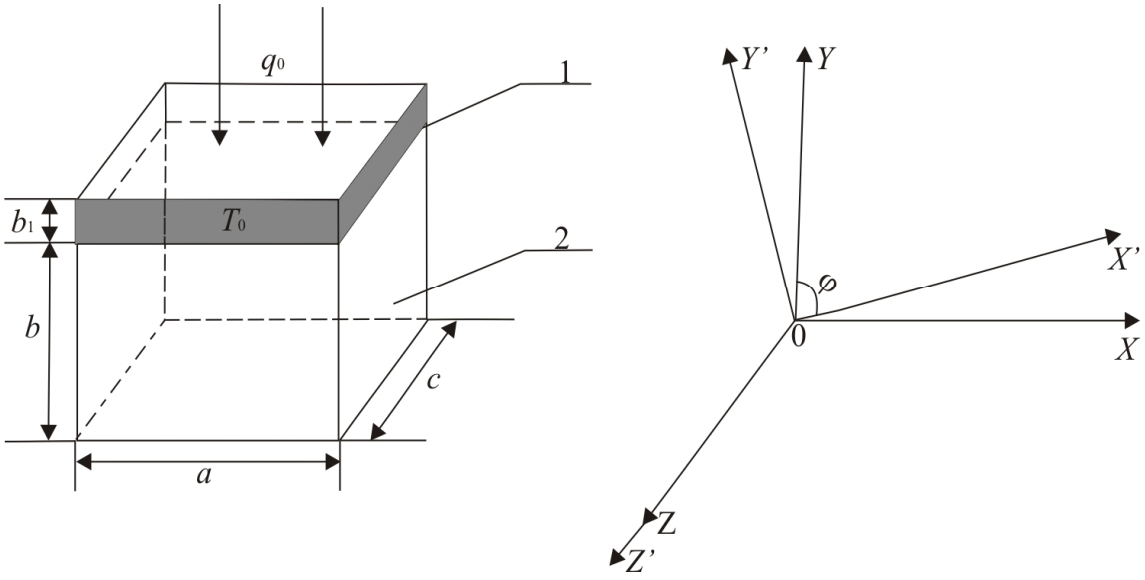

Fig.1. Schematic of AOT: thermostat 1, anisotropic plate 2. To the right – laboratory coordinate system XYZ and orientation of crystallographic axes X'Y'Z' of plate 2.

A uniform monochromatic radiant flux of density q_0 is incident on the upper face of thermostat 1 of thickness b_1 made of optically transparent material in the required wavelength spectrum with absorption coefficient γ_1. The lower face of the thermostat is in thermal optical contact with the upper face 2 of AOT at temperature $T = T_0$. The lateral and lower faces of plate 2 are adiabatically isolated. In so doing, the boundary effects are disregarded ($a = c >> b$) [8]. On passing through such a plate, the uniform monochromatic radiant flux of density q_0 and wavelength λ_0 causes the appearance of temperature gradient and transverse thermoEMF unambiguously related to it.

In the presence of internal heat sources, the unsteady-state temperature distribution in AOT can be found from the basic Fourier conduction law [9]

$$\frac{\partial T}{\partial t} = \frac{1}{d\,C_0}\sum_{i,k=1}^{3}\chi_{ik}\frac{\partial^2 T}{\partial x_i \partial x_k} + \frac{q_v}{d\,C_0}, \quad (2)$$

where d is AOT material density, C_0 is specific heat, χ_{ik} are corresponding components of thermal conductivity tensor found from another relation of system (1), q_v is the amount of heat released by internal sources in unit volume per unit of time and defined by the Bouguer-Lambert law.

For the unsteady-state temperature distribution in the approximation

$$\frac{\partial T}{\partial \mathrm{x}} = \frac{\partial T}{\partial \mathrm{z}} = 0, \quad \chi_{12} < \chi_{22}$$

thermal conductivity equation (2) is of the form

$$\frac{\partial T}{\partial t} = R^2 \frac{\partial^2 T}{\partial y^2} + P e^{-\gamma(b-y)}, \tag{3}$$

where $R^2 = \frac{\chi_{22}}{C_0 d}$, $P = \frac{q_0 \gamma}{C_0 d} \exp\left[-\gamma_1 b_1\right]$, γ is absorption coefficient of AOT material.

Solution of inhomogeneous equation (3) under the boundary and initial conditions

$$\left.\frac{\partial T}{\partial y}\right|_{y=0} = 0; \quad T\big|_{y=b} = T_0; \; T\big|_{t=0} = T_0 \tag{4}$$

will be sought for as

$$T(y,t) = T_0 + V(y,t). \tag{5}$$

Substituting (5) into (3), we will obtain the thermal conductivity problem

$$\frac{\partial V}{\partial t} = R^2 \frac{\partial^2 V}{\partial y^2} + P e^{-\gamma(b-y)} \tag{6}$$

for function $V(y,t)$ under the homogeneous boundary and initial conditions

$$\left.\frac{\partial V}{\partial y}\right|_{y=0} = 0; \; V\big|_{y=b} = 0; \; V\big|_{t=0} = 0. \tag{7}$$

General solution of inhomogeneous equation (6) will be found as a sum of general solution of the homogeneous and partial solution of the inhomogeneous solutions (6), i.e.

$$V(y,t) = V_{\text{hom}}(y,t) + V_{\text{in hom}}(y,t). \tag{8}$$

General solution of homogeneous equation (6) under zero boundary conditions (7) results in Sturm-Liouville problem that has the eigenfunction $\cos\left[\frac{(2n+1)\pi}{2b} y\right]$ corresponding to the eigenvalues $\lambda_n = \frac{(2n+1)\pi}{2b}$, where $n = 0,1,2,\ldots$. Partial solution of inhomogeneous equation (6) will be sought for as expansion into a Fourier series in terms of eigenfunctions $\cos\left[\frac{(2n+1)\pi}{2b} y\right]$ of homogeneous:

$$V(y,t)=\sum_{n=0}^{\infty}\Phi_n(t)\cos\left[\frac{(2n+1)\pi}{2b}y\right]. \tag{9}$$

Substituting (9) and the expansion of thermal conductivity equation (6) inhomogeneity into a Fourier series in terms of eigenfunctions of homogeneous problem, we obtain an equation for determination of $\Phi_n(t)$

$$\sum_{n=0}^{\infty}\left\{\Phi_n{}'(t)+\left[\frac{(2n+1)\pi}{2b}R\right]^2\Phi_n(t)-\varphi_n\right\}\cos\left[\frac{(2n+1)\pi}{2b}y\right]=0, \tag{10}$$

where $\varphi_n=\frac{2}{b}\int_0^b Pe^{-\gamma(b-y)}\cos\left[\frac{(2n+1)\pi}{2b}\mathrm{y}\right]dy$. The resulting equality can be considered as zero function expansion into a Fourier series in terms of eigenfunctions $\cos\left[\frac{(2n+1)\pi}{2b}y\right]$. Substituting $\Phi_n(t)$ into equation (9), we obtain a solution of thermal conductivity problem (6)-(7) as below

$$V(y,t)=\int_0^t d\tau\int_0^b\left[\frac{2}{b}\sum_{n=0}^{\infty}\exp\left[-\left[\frac{(2n+1)}{2b}R\right]^2(t-\tau)\right]\cos\left[\frac{(2n+1)\pi}{2b}y\right]\cos\left[\frac{(2n+1)\pi}{2b}y\right]\xi\right]Pe^{-\gamma(b-\xi)}d\xi. \tag{11}$$

Let us introduce the influence function of instantaneous point heat source

$$G(y,\xi,t-\tau)=\frac{2}{b}\sum_{n=0}^{\infty}\exp\left[-\left[\frac{(2n+1)}{2b}R\right]^2(t-\tau)\right]\cos\left[\frac{(2n+1)\pi}{2b}\mathrm{y}\right]\cos\left[\frac{(2n+1)\pi}{2b}\xi\right]. \tag{12}$$

Then solution of (11) will acquire the form

$$V(y,t)=\int_0^t d\tau\int_0^b G(y,\xi,t-\tau)Pe^{-\gamma(b-\xi)}\mathrm{d}\xi. \tag{13}$$

Substituting (13) into (5), upon integration we obtain final expression for the unsteady–state temperature distribution

$$\begin{aligned}T(y,t)=T_0+\frac{2q_0\gamma}{b\chi_{22}}\exp\left[-\gamma_1 b_1\right]\sum_{n=0}^{\infty}\frac{\left[(-1)^n\frac{(2n+1)\pi}{2b}-\gamma e^{-\gamma b}\right]}{\left[\gamma^2+\left(\frac{(2n+1)\pi}{2b}\right)^2\right]\left(\frac{(2n+1)\pi}{2b}\right)^2}\times\\ \times\left[1-\exp\left(\frac{-(2n+1)^2\pi^2}{4}\frac{\chi_{22}}{C_0 d b^2}\mathrm{t}\right)\right]\cos\left(\frac{(2n+1)\pi}{2b}y\right).\end{aligned} \tag{14}$$

From relation (14) it is seen that unsteady-state temperature distribution of AOT depends on the absorption coefficients of thermostat and thermoelement materials and the anisotropy of thermal conductivity coefficient. Moreover, temperature distribution is a function of thermoelement and thermostat geometry and has a complex nonlinear dependence on coordinate *y* and time *t*.

Fig. 2 shows a plot of temperature field distribution $\Delta T(y,t)=T(y,t)-T_0$ for AOT made of $ZnAs_2$ in the case of optical transmission ($\gamma b<<1$), and Fig. 3 – in the case of surface absorption ($\gamma b>>1$).

Components of thermoelectric field intensity E_i^T are defined by the following relation

$$E_i^T = \sum_{k=1}^{3} \alpha_{ik} \frac{\partial T}{\partial x_k}, \quad (i = 1, 2, 3). \tag{15}$$

Substituting (14) into (15) we obtain

$$E_x^T = -\frac{2 q_0 \gamma \alpha_{12}}{b \chi_{22}} \exp\left[-\gamma_1 b_1\right] \sum_{n=0}^{\infty} \frac{\left[(-1)^n \frac{(2n+1)\pi}{2b} - \gamma e^{-\gamma b}\right]}{\left[\gamma^2 + \left(\frac{(2n+1)\pi}{2b}\right)^2\right] \frac{(2n+1)\pi}{2b}} \times$$
$$\times \left[1 - \exp\left(\frac{-(2n+1)^2 \pi^2}{4} \frac{\chi_{22}}{C_0 d b^2} t\right)\right] \sin\left(\frac{(2n+1)\pi}{2b} y\right). \tag{16}$$

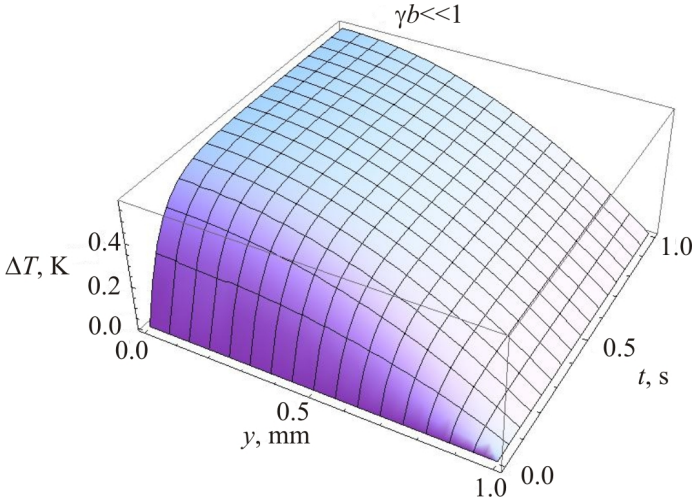

Fig.2. Temperature field distribution of $ZnAs_2$ AOT in the case of optical transmission.

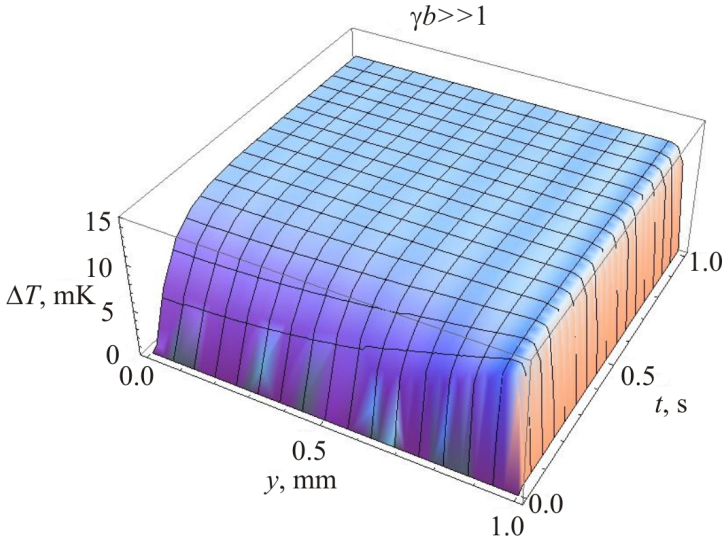

Fig.3. Temperature field distribution of $ZnAs_2$ AOT in the case of surface absorption.

According to [10], the transverse thermopower ε_x is defined by the following relation

$$\varepsilon_x = \frac{1}{b\,c}\int_0^b dy \int_0^c dz \int_0^a E_x^T dx\,. \tag{17}$$

Substituting (16) into (17), upon integration we obtain the expression for the transverse thermoelectromotive force ε_x of AOT at hand in the form

$$\varepsilon_x(t) = -\frac{2q_0\,\gamma\,a\alpha_{12}}{\chi_{22}}\exp\left[-\gamma_1 b_1\right]\sum_{n=0}^{\infty}\frac{\left[(-1)^n\,\dfrac{(2n+1)\pi}{2b} - \gamma\,e^{-\gamma b}\right]}{\left[\gamma^2 + \left(\dfrac{(2n+1)\pi}{2b}\right)^2\right]\left(\dfrac{(2n+1)\pi}{2b}\right)^2}\times$$
$$\times\left[1-\exp\left(\frac{-(2n+1)^2\pi^2}{4}\,\frac{\chi_{22}}{C_0\,d\,b^2}\,\mathrm{t}\right)\right]. \tag{18}$$

Figs. 4 and 5 show the plots of transverse thermopower ε_x versus b of AOT and time t for optical transmission ($\gamma b << 1$) and surface absorption ($\gamma b >> 1$), respectively.

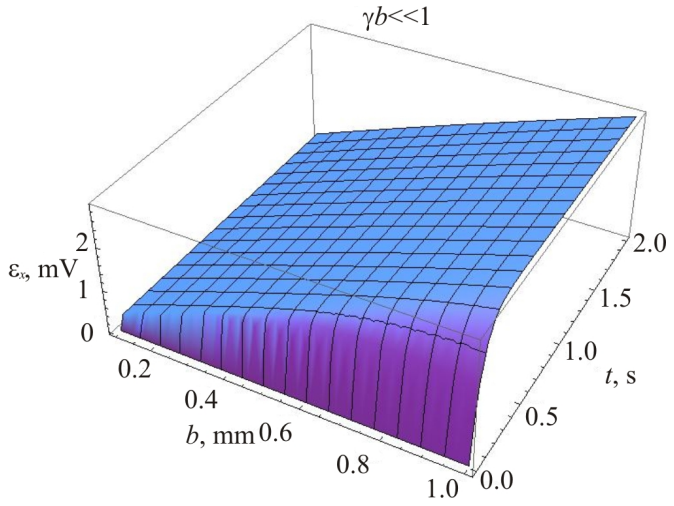

Fig.4. Transverse thermopower ε_x of $ZnAs_2$ AOT in the case of optical transmission versus time t and height b of thermoelement at thermostating of the upper working face.

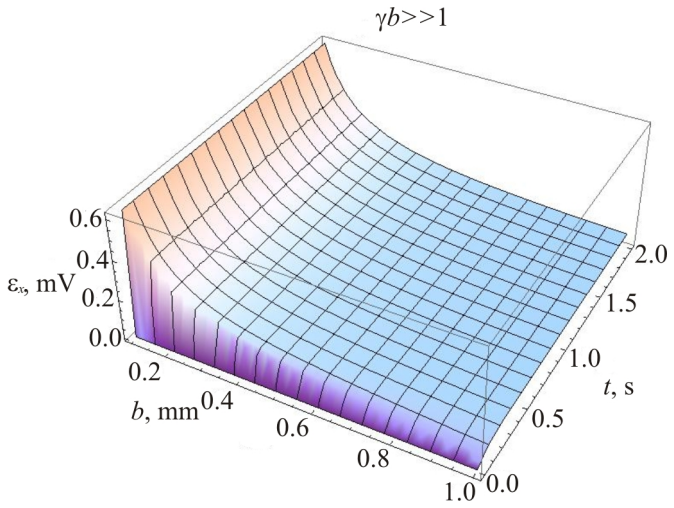

Fig.5. Transverse thermopower ε_x of $ZnAs_2$ AOT in the case of surface absorption versus time t and height b of thermoelement at thermostating of the upper working face.

It has been established that with increasing time t, both in the case of optical transmission and surface absorption the transverse thermopower grows and at certain value of t it becomes constant. From the plots it is seen that with increasing AOT height, the transverse thermopower has a complex nonlinear dependence at the initial time instants both for optical transmission and surface absorption. At later time instants, the complex nonlinear height dependence is retained for surface absorption and for optical transmission there is a quasilinear dependence of the transverse thermopower on AOT height b.

Conclusions

The expressions for the transverse thermopower of $ZnAs_2$ AOT under thermostating of the upper working face for the cases of optical transmission and surface absorption have been studied. The AOT considered make it possible to record and control radiant fluxes in a wide spectral range.

References

1. W.Thomson, On Thermoelectric Currents in Linear Conduction Crystalline Substance, *Math. Phys. Pap.* – 1882. – № 1. – P. 266-273.
2. I.M.Pilat, A.G.Samoilovivh, and L.I.Anatychuk, Thermoelement, USSR *Certificate of Authorship 230915,* Publ.in Bulletin of Inventions, №3, 1970.
3. L.I.Anatychuk, Thermoelements and Thermoelectric Devices (Kyiv: Naukova Dumka, 1979), 767p.
4. L.I.Anatychuk, O.J.Luste, Eddy Thermoelectric Currents and Eddy Thermoelements, *Semiconductors* **10**(5), 817-831(1976).
5. A.A.Snarskii, A.M.Palti, A.A.Ashcheulov, Anisotropic Thermoelements (Review), *Semiconductors* **31**(11), 1281-1298 (1997).
6. A.A.Ashcheulov, I.M.Rarenko, and N.K.Voronka, Optimized Materials Based on Cadmium Antimonide and their Application, *J. Thermoelectricity* – 1995. – № 3. – P. 73-88.
7. A.A.Ashcheulov, I.V.Gutsul, Anisotropic Optical Thermoelectric Elements, *J. Thermoelectricity* – 1997. – № 3. – P. 81-89.
8. V.N.Slipchenko, A.A.Snarskii, Effect of Thermal Conductivity Anisotropy on Transverse Thermopower, *Semiconductors* **8**(10), 2010-2012 (1974).
9. A.V.Lykov, Theory of Thermal Conductivity (Moscow: Vysshaya Shkola, 1967), 600 p.
10. A.A.Snarskii, EMF of Thermoelements Using Thermopower Anisotropy. I. Rectangular Anisotropic Thermoelements, *Semiconductors* **11**(10), 2053-2055 (1977).

Submitted 02.12.2014.

V.A.Romaka[1,2], P.Rogl[3], Yu.V.Stadnyk[4], L.P.Romaka[4], D. Kaczorowski[5], V.Ya. Krayovskyy[2], R.O.Korzh[2], A.M.Horyn[4]

[1] Ya. Pidstryhach Institute for Applied Problems of Mechanics and Mathematics National Academy of Sciences of Ukraine, 3-b, Naukova Str., Lviv, 79060, Ukraine;
[2] National University "Lvivska Polytechnika", 12, S.Bandera Str., Lviv, 79013,Ukraine;
[3] Universität Wien, 42, Währinger Str., A-1090, Wien, A-1090, Österreich;
[4] Ivan Franko National University of Lviv, 6, Kyryla and Mefodiya Str., 79005, Lviv, Ukraine;
[5] W.Trzebiatowski Institute of Low Temperature and Structural Research Polish Academy of Sciences, 2, Okolna St., Wroclaw, 50-950 Poland

FIATURES OF THE ELECTRON STRUCTURE AND CONDUCTION MECHANISMS IN THE $Zr_{1-x}Ce_xNiSn$ THERMOELECTRIC MATERIAL

The crystal and electronic structures, the temperature and concentration dependencies of the magnetic susceptibility, resistivity, and the Seebeck coefficient of the $Zr_{1-x}Ce_xNiSn$ thermoelectric material in the ranges: T = 80 – 400 K, x = 0.01 – 0.10 were studied. Increasing values of the thermoelectric power factor Z(x) were for the first time observed in n-ZrNiSn doped with Ce atoms in Ce^{4+} valence state. This leads to the generation of donor defects in the crystal and makes $Zr_{1-x}Ce_xNiSn$ solid solution a promising thermoelectric material.*

Key words: electronic structure, resistivity, Seebeck coefficient.

Introduction

Attempts to obtain thermoelectric materials with high efficiency of thermal into electric energy conversion [1] by doping of *n-ZrNiSn* semiconductor with the atoms of rare-earth metals (*R*) were unsuccessful [2-4]. In [5] it is shown that with substitution of *Zr* by *R* atoms structural defects of acceptor nature are formed in crystal, causing a drift of the Fermi level ε_F from conduction band and leading to increase in the values of resistivity and decrease in the Seebeck coefficient.

The point is that at formation of solid solutions with participation of *R* atoms, their valence electrons go into formation of chemical bonds or pass to conduction band, and electrons of partially filled 4*f*- shell due to their small size (~0.04 nm) remain localized on the ion core. A typical valence value of rare-earth metal is 3+ (R^{3+}). It means that *R* atom is left by 3 valence electrons, their 4*f*-shell is filled only partially, and a defect generated in $Zr_{1-x}R_xNiSn$ is of acceptor nature. In all previously investigated $Zr_{1-x}R_xNiSn$ solid solutions [6] the valence of *R* atoms was 3+, and for 4*f*- electrons the case of maximum localization was always realized, namely the respective electron shells behaved as atomic ones and were characterized by the same quantum numbers *L, S, J* as the states of the respective isolated ion.

In a series of rare-earth metals, such as *Ce* and *Sm*, *Eu*, *Yb,* the valence, alongside with 3+, can acquire the values of 4+ and 2+ , respectively (abnormal valence) [7]. Thus, in the case of Ce^{3+}, the 4*f*-shell comprises 1 uncoupled electron ($4f^1$) and is vacant ($4f^0$) in case of Ce^{4+} valence (*Ce* atom leaves 4 valence electrons). As a result, for the respective atoms different valence states are energetically close, and atoms of rare-earth elements can possess the average fractional number of 4*f*-electrons

(intermediate valence) [7]). In compounds with participation of *R* metals that are semiconductors, the 4*f*- level is located close to conduction band (ε_c).

That is, it can be expected that in the case of doping of *n-ZrNiSn* semiconductor, for instance, with *Ce* atoms their 4*f*-shell can lose stability. Hence the idea to use the property of *Ce* to change valence at doping of *n-ZrNiSn*, which can bring about the generation in crystal of structural defects, this time of *donor* nature, and meet the condition of producing material with high efficiency of thermal into electric energy conversion [8]. In turn, research on the magnetic susceptibility of *Ce* compounds allows in paramagnetic area to identify the degree of occupancy of 4*f*-shell [9]. *The purpose* of this work is to study the conductivity mechanisms of *n-ZrNiSn* doped with *Ce* which will permit to predict the behaviour of the kinetic characteristics of $Zr_{1-x}Ce_xNiSn$ and study the conditions of producing material with high efficiency of thermal into electric energy conversion.

Investigation procedures

The object to be investigated included crystalline structure, electron density distribution (DOS), the magnetic, electrokinetic and energy characteristics of $Zr_{1-x}Ce_xNiSn$. The samples were synthesized in the laboratory of Institute for Physical Chemistry, Vienna University. The X-ray structural analysis (powder method) was used to obtain the data arrays (diffractometer Guinier-Huber image plate system, $CuK\alpha_1$), and Fullprof program [10] was employed for the calculation of structural characteristics. The chemical and phase compositions of samples were controlled by microprobe analyzer (EPMA, energy-dispersive X-ray analyzer). The electronic structure calculations were performed by the Korringa-Kohn-Rostoker (KKR) method in coherent potential approximation (CPA) and local density approximation (LDA) [11] with the use of Moruzzi-Janak-Williams exchange-correlation potential [12]. The accuracy of calculating the position of the Fermi level ε_F is ±8 meV. The temperature and concentration dependences of the electrical resistivity (ρ) and the Seebeck coefficient (α) were measured with respect to copper and magnetic susceptibility (χ) (Faraday method) of $Zr_{1-x}Ce_xNiSn$ samples in the ranges: T = 80–400 K, $N_D^{Ce} \approx 1.9\cdot10^{20}$ cm^{-3} ($x = 0.01$)÷$1.9\cdot10^{21}$ cm^{-3} ($x = 0.10$) and the magnetic field intensity $H \leq 10$ кЕ.

Structural research on $Zr_{1-x}Ce_xNiSn$

The microprobe analysis of the concentration of atoms on the surface of $Zr_{1-x}Ce_xNiSn$ samples has shown their conformity to the initial charge compositions, and the X-ray phase and structural analyses have revealed no traces of other phases. As was expected, replacement of smaller-size *Zr* atoms (r_{Zr} = 0.1602 nm) by larger-size *Ce* atoms (r_{Ce} = 0.172 nm) leads to increase in the values of unit cell period *a(x)* of $Zr_{1-x}Ce_xNiSn$ (Fig. 1).

Refinement of $Zr_{1-x}Ce_xNiSn$ crystalline structure by powder method with a simultaneous refinement of the isotropic parameters of atomic substitution and occupancy of (4*a*) crystallographic position of *Zr* has shown that the lowest value of coefficient of mismatch between a model of crystalline structure and an array of Bragg reflections was obtained for a model where the occupancy of position of *Zr*(*Ce*) atoms for $x \geq 0.01$ is 100%. In other words, like in the previous cases of $Zr_{1-x}R_xNiSn$ [6], *ordering* of crystalline structure makes it resistant to temperature and time changes, which creates prerequisites for preparation of material with stable characteristics. Recall that *n-ZrNiSn* structure is disordered by virtue of partial, up to ~1% ($y \approx 0.01$), occupancy by *Ni* ($3d^8 4s^2$) atoms of 4*a*

position of *Zr* ($4d^25s^2$) atoms, which creates donor structural defects and accounts for the nature of electron conductivity type, and the compound formula is $(Zr_{1-y}Ni_y)NiSn$ [6].

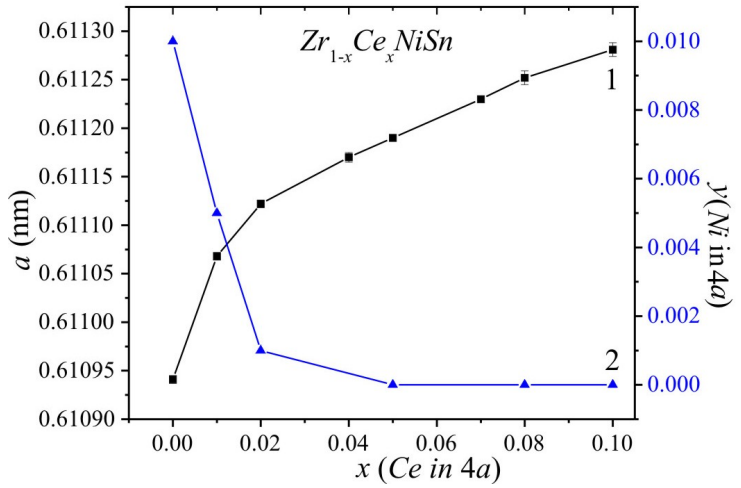

Fig. 1. Change in the values of unit cell period a(x) (1) and concentration of Ni atoms in 4a position of Zr atoms (2) in $Zr_{1-x}Ce_xNiSn$

On the other hand, *ordering* of $Zr_{1-x}Ce_xNiSn$ crystalline structure for $x > 0.01$ testifies that in the area of $x = 0$–0.02 *Ni* atoms leave the position of *Zr* atoms (4*a*) (Fig. 1): there is "healing" of donor structural defects which is accompanied by a reduced concentration of donors. Simultaneously, in the same 4*a* crystallographic position with substitution of *Ce* for *Zr* atoms, either acceptor structural defects can be generated, when the valence state of Ce^{3+}, or donor defects, when the valence state of Ce^{4+}.

Therefore, doping of *n-ZrNiSn* with the atoms of rare-earth metal *Ce* by substitution of *Zr* is accompanied by a simultaneous reduction of donor defects (*Ni* atoms in 4*a* position of *Zr* atoms) and generation in the same position of donor or acceptor defects depending on the valence state of *Ce*. This raises the question as to what is the valence of *Ce* in $Zr_{1-x}Ce_xNiSn$ and whether it will be influenced by a change in concentration. After all, these are key parameters for the calculation of the electron structure of solid solution. Therefore, determination of the valence state of *Ce* in $Zr_{1-x}R_xNiSn$ is a prerequisite for understanding the conduction mechanisms of semiconductor.

Research on the magnetic state of *Ce* in $Zr_{1-x}Ce_xNiSn$

Doping of *n-ZrNiSn* weak diamagnetic ($\chi = -0.07\cdot10^{-6}$ cm^3/g) [6] with the lowest in our experiment concentration of *Ce* ($x = 0.01$) causes the origination of paramagnetic state, and low values of magnetic susceptibility ($\chi = 0.23\cdot10^{-6}$ cm^3/g), independence of magnetic field intensity and temperature are indicative of Pauli paramagnetism (Fig. 2).

In this case, the magnetic susceptibility of $Zr_{1-x}Ce_xNiSn$ is defined by free electrons, and its values are proportional to the electron density of states at the Fermi level $g(\varepsilon_F)$ (for Pauli paramagnetic $\chi \sim g(\varepsilon_F)$). Taking into account that in the concentration $x = 0$–0.08 the dependence $\chi(x)$ in $Zr_{1-x}Ce_xNiSn$ increases, one can state that structural defects of donor nature are generated in the crystal. The absence of a magnetic moment in $Zr_{1-x}Ce_xNiSn$ samples (Pauli paramagnetism) results from the absence of uncoupled electron on 4*f*- shell (it is vacant ($4f^0$)), therefore the valence state of Ce^{+4}. Incomprehensible is the reduction of $\chi(x)$ values of $Zr_{1-x}Ce_xNiSn$ at $x > 0.08$, pointing to the reduction of $g(\varepsilon_F)$. One of the reasons for such $\chi(x)$ behaviour can be

generation in the crystal of *acceptors* by the mechanism unknown so far, but this calls for a detailed investigation.

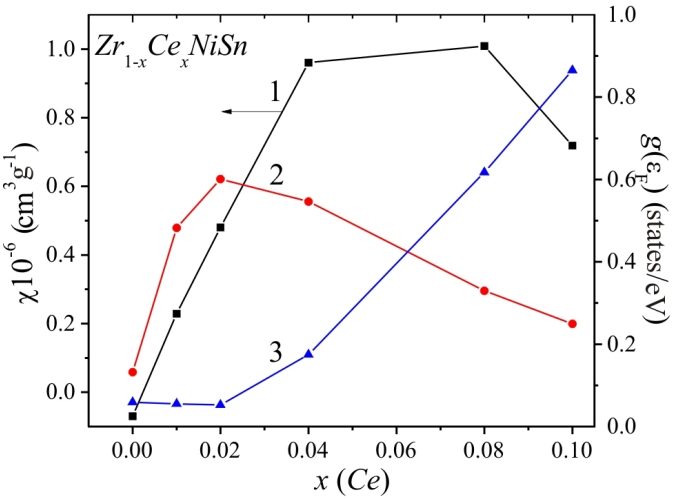

Fig. 2. Change in the values of magnetic susceptibility χ at T=276 K (1) and the electron density of states at the Fermi level $g(\varepsilon_F)$ in $Zr_{1-x}Ce_xNiSn$ for the valence of Ce^{4+} (2) and Ce^{3+} (3)

Thus, research on the magnetic susceptibility of $Zr_{1-x}Ce_xNiSn$ has shown that *Ce* atoms do not possess local magnetic moment in the area of concentrations $x = 0$ –0.08, and the generated structural defects are of donor nature.

Research on the electron structure of $Zr_{1-x}Ce_xNiSn$

To predict the behaviour of the Fermi level ε_F, the energy gap ε_g and the kinetic characteristics of *n-ZrNiSn* doped with *Ce*, the electron density of states (DOS) was calculated for the case of ordered structure and valence states of Ce^{3+} and Ce^{4+} (Fig. 3).

As was expected, in the case of Ce^{3+} the acceptor-nature structural defects are generated in the crystal, and so, with increasing impurity concentration, the Fermi level ε_F moves from the edge of the conduction band ε_C to the valence band of ε_V $Zr_{1-x}Ce_xNiSn$ and will cross it at $x \approx 0.05$. Instead, in the case of Ce^{4+} the conduction band ε_C is reconstructed, the energy gap is reduced, and the Fermi level ε_F is fixed close to the conduction band by virtue of the donor nature of defects generated in the crystal.

In this context, it is interesting to compare the results of change in the magnetic susceptibility values of $Zr_{1-x}Ce_xNiSn$ Pauli paramagnetic and the electron density of states at the Fermi level $g(\varepsilon_F)$ of $Zr_{1-x}Ce_xNiSn$ for the valence states of Ce^{3+} and Ce^{4+} (Fig. 2). Calculations show that in the case of Ce^{3+}, when acceptors are generated in a crystal, the density of states $g(\varepsilon_F)$ slightly decreases in the area $x = 0$–0.02, passing through the minimum at $x \approx 0.02$ related to crossing the midgap by the Fermi level ε_F . At $x > 0.02$, the semiconductor is recompensated, the holes become the main charge carriers, and the Fermi level approaches the valence band and will cross it at $x \approx 0.06$, which is accompanied by increasing values of density of states at the Fermi level $g(\varepsilon_F)$. That is, a change in the density of states at the Fermi level $g(\varepsilon_F)$ of $Zr_{1-x}Ce_xNiSn$ for the case of Ce^{3+} is not matched with the behaviour of magnetic susceptibility $\chi(x)$ which within the concentration $x = 0.06$ passes through the maximum and slightly decreases thereafter.

Instead, the pattern of change in the values of density of states at the Fermi level $g(\varepsilon_F)$ of $Zr_{1-x}Ce_xNiSn$ for the case of Ce^{4+}, when donors are generated in a crystal, is close to dependence $\chi(x)$ (Fig. 2), which proves the earlier conclusion on the valence state of Ce^{4+}. We call attention to the fact of splitting the conduction band ε_C in the case of Ce^{4+} which becomes apparent at $x \approx 0.05$ (Fig. 3*b*) as two extremes

pointing to the reduction of the electron density of states at the Fermi level. One may state that decay of dependence $\chi(x)$ at $x > 0.08$ reflects the fact of reconstruction of the electronic structure of $Zr_{1-x}Ce_xNiSn$ and is not related to generation of acceptor structural defects.

The results of the kinetic investigations of $Zr_{1-x}Ce_xNiSn$ will further permit to determine the valence state of *Ce*, as well as the nature of generated defects and their effect on the compensation degree of a semiconductor.

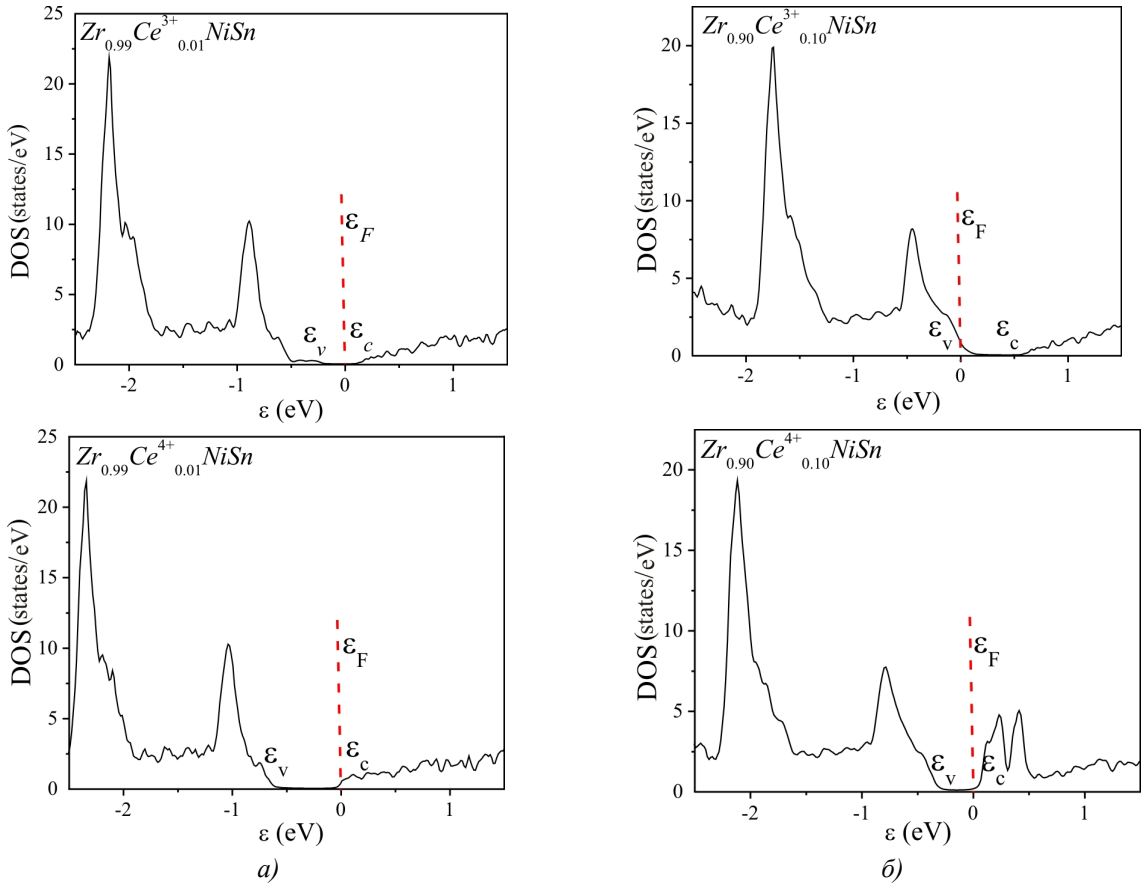

Fig. 3. Calculation of the electron density of states DOS of $Zr_{1-x}Ce_xNiSn$ for Ce^{+3} (a) and Ce^{+4} (b)

Research on the electrokinetic and energy characteristics of $Zr_{1-x}Ce_xNiSn$

The temperature and concentration dependences of the electric resistivity ρ and the Seebeck coefficient α for $Zr_{1-x}Ce_xNiSn$ samples are given in Figs. 4 and 5. The temperature dependences ln ρ(1/T) and α(1/T) are typical of doped semiconductors with high- and low-temperature activation areas [13] used to calculate the energy parameters of semiconductor. Thus, the activation areas of dependences ln ρ(1/T) were used to calculate the values of activation energies from the Fermi level ε_F to percolation level of the conduction band ε_1^ρ and electron jumps ε_3^ρ in the states with energies close to the Fermi level, and the activation areas of dependences α(1/T) were used to calculate the values of activation energies ε_1^α and ε_3^α which yield, respectively, the values of modulation amplitude of continuous energy bands and small-scale fluctuation of doped and compensated semiconductors [6,13].

Introduction to *n-ZrNiSn* of the lowest concentration of *Ce* atoms does not lead to a change in conduction type of $Zr_{1-x}Ce_xNiSn$, as it was in the previous cases of semiconductor doping with atoms of rare-earth metals [6], and the Seebeck coefficient values remain negative for all values of

temperature and *Ce* concentration (Fig. 4*b*, 5*b*). Thus, at 80 K, the Seebeck coefficient values vary from $\alpha(x=0)=-14$ μV·K^{-1} to $\alpha(x=0.01)=-106.5$ μV·K^{-1} and $\alpha(x=0.10)=-8$ μV·K^{-1}. Such a behaviour of $\alpha(x)$ allows stating that structural defects formed in the crystal are of donor nature, which is possible only with the valence of Ce^{4+}.

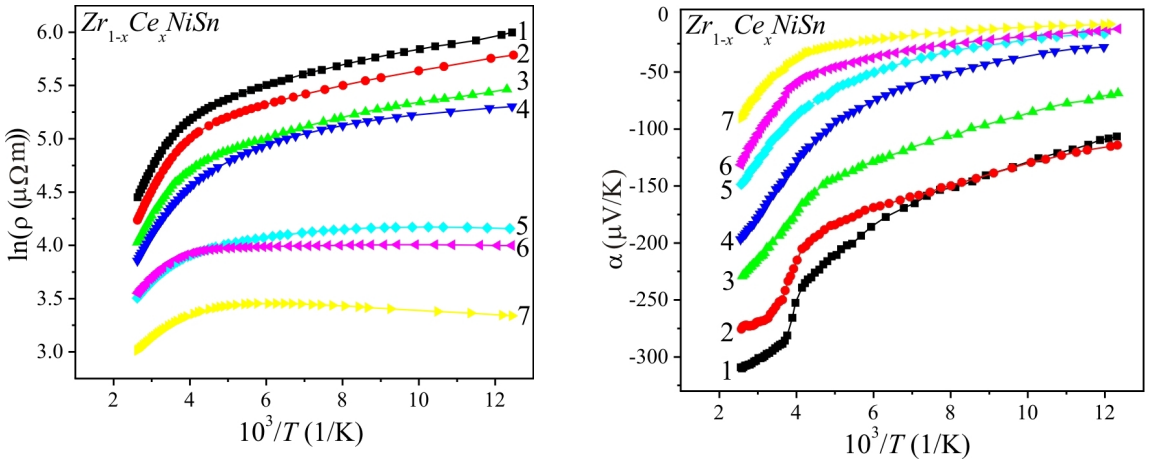

a) *b)*

Fig. 4. Temperature dependences of resistivity (a) and the Seebeck coefficient (b) of $Zr_{1-x}Ce_xNiSn$: 1 – x = 0.01; 2 – x = 0.02; 3 – x = 0.04; 4 – x = 0.05; 5 – x = 0.07; 6 – x = 0.08; 7 – x = 0.10

The fact that *Ce* atoms introduced into y *n-ZrNiSn* generate donors is also shown by dependences of change in the values of resistivity ρ(*x*) (Fig. 5*a*). Thus, introduction of the lowest in the experiment concentration of *Ce* is attended by the drastic reduction of ρ(*x*) values, for instance, at 80 K, from ρ(*x*=0) = 4751.1 μΩ·m to ρ(*x*=0.01) = 402.48 μΩ·m and ρ(*x*=0.10) = 28.20 μΩ·m, which is only possible under condition of semiconductor doping with donors. In this case, the valence of Ce^{4+}.

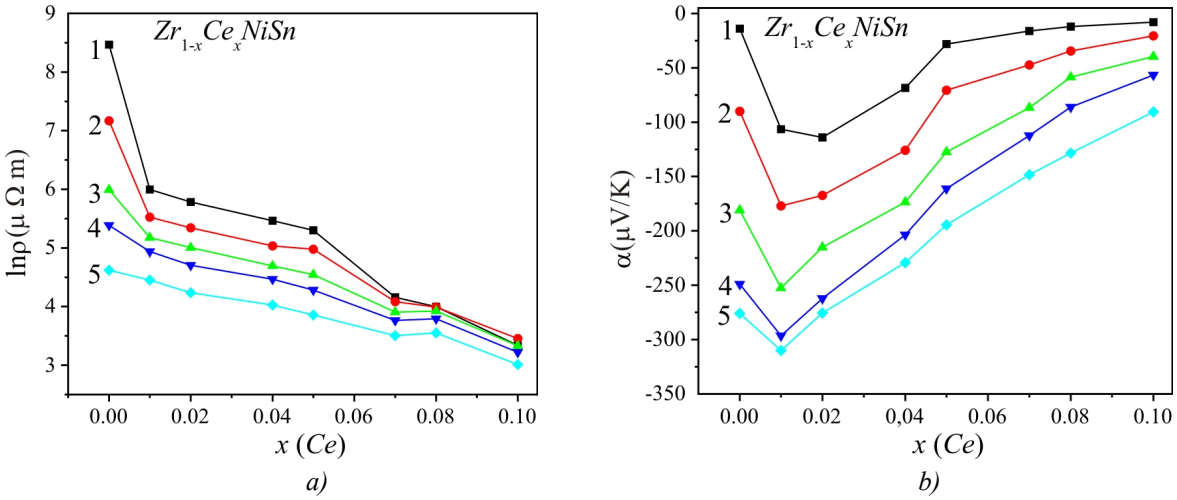

a) *b)*

Fig. 5. Change in the values of electric resistivity $\rho(x)$ (a) and the Seebeck coefficient $\alpha(x)$ (b) of $Zr_{1-x}Ce_xNiSn$ at temperatures: 1 – 80 K; 2 – 160 K; 3 – 250 K; 4 – 300 K; 5 – 380 K

Therefore, the two experimental results, namely the change in the values of electric resistivity ρ(*x*) and the Seebeck coefficient α(*x*) of $Zr_{1-x}Ce_xNiSn$, point to the presence of a mechanism of generation of donor structural defects, testifying to Ce^{4+}. And it means that the degree of compensation of $Zr_{1-x}Ce_xNiSn$ semiconductor (the ratio between ionized donors and acceptors) should be only

reduced, since we add donors to n-type semiconductor *n-ZrNiSn* by generation of structural donor defects. The obtained result is in full conformity with the experimental research on magnetic state of *Ce* in $Zr_{1-x}Ce_xNiSn$, as well as with the results of calculation of semiconductor electron structure.

A change in the values of activation energy $\varepsilon_1^{\rho}(x)$ $Zr_{1-x}Ce_xNiSn$ (activation energy from the Fermi level ε_F to the edge of the conduction band) does not give grounds for stating the presence of acceptors in the crystal. Thus, in *n-ZrNiSn* the value of energy $\varepsilon_1^{\rho}(x)$ reflects the position of the Fermi level ε_F to the edge of the conduction band, whereas doping of semiconductor with the lowest in the experiment concentration of *Ce* (x = 0.01) results in the reduction of $\varepsilon_1^{\rho}(x)$ values (Fig. 6*a*). That is, the Fermi level ε_F drifts in the direction of the conduction band, which is only possible at generation of donors in the crystal under condition of Ce^{4+}.

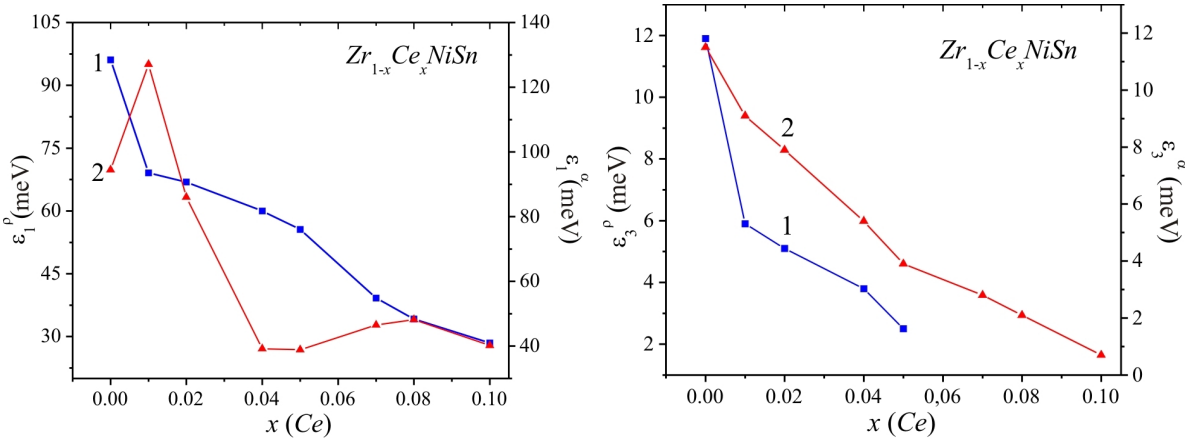

Fig. 6. Change in the values of activation energies $\varepsilon_1^{\rho}(x)$ (1) and $\varepsilon_1^{\alpha}(x)$ (2) (a) and $\varepsilon_3^{\rho}(x)$ (1) and $\varepsilon_3^{\alpha}(x)$ (2) (b) of $Zr_{1-x}Ce_xNiSn$

In this case, what is the reason for the origination of maximum at x = 0.01 on the dependence $\varepsilon_1^{\alpha}(x)$ the values of which are proportional to modulation amplitude of continuous energy bands $\varepsilon_1^{\alpha}(x)$ (Fig. 6*a*), which reflects a change in semiconductor compensation degree? At first sight, it looks like a manifestation of the mechanism for generation of acceptors by so far unknown mechanism which compensates donors, as long as maximum $\varepsilon_1^{\alpha}(x)$ at x = 0.01 reflects a decrease in the number of donors in $Zr_{1-x}Ce_xNiSn$. And this despite the fact that there is constant increase in the number of donors generated in the crystal as a result of occupation by Ce^{4+} of *Zr* atoms position.

To explain this effect, it is necessary to involve the results of structural investigations which showed that in $(Zr_{1-y}Ni_y)NiSn$ undoped semiconductor the position of *Zr* atoms (4*a*) up to ~1% (y = 0.01) is occupied by *Ni* atoms that are the source of donors. In the concentration area of impurity atoms x = 0–0.02 there is a reduction and full liquidation of donor structural defects (by decreasing the number of donors) when *Ni* atoms leave crystallographic positions 4*a* of *Zr* atoms due to structure ordering (Fig. 1). As long as *Ce* impurity atoms generate donors in crystal, in the area x = 0–0.02 per each x number of donors introduced into crystal (*Ce* atoms) the available number of donors is reduced by y value (*Ni* atoms leave 4*a* position). In other words, maximum on the dependence $\varepsilon_1^{\alpha}(x)$ $Zr_{1-x}Ce_xNiSn$ at x = 0.01 reflects the fact of reducing the rate of generation of donors, which in semiconductor usually takes place only under the emergence of acceptors, which results in the increase of compensation degree [13].

And only at higher *Ce* concentrations ($x > 0.02$), when *Ni* atoms will leave 4*a* position ($y = 0$), the increase in the concentration of impurity atoms will correspond to the number of generated donors, which in the *n*-type $Zr_{1-x}Ce_xNiSn$ semiconductor will only reduce the compensation degree, as testified by the behaviour $\varepsilon_1^{\alpha}(x)$ (Fig. 5*a*). Minor extreme $\varepsilon_1^{\alpha}(x)$ at $x = 0.08$ is not related to the appearance of acceptors in the crystal, which might increase the semiconductor degree of compensation, but reflects the fact of reconstruction of the conduction band ε_C, as discussed above.

The reduced values of activation energy of hopping conduction $\varepsilon_3^{p}(x)$ (Fig. 5*b*) point to the reduction of electron localization radius, which in *n*-type semiconductor is possible with increasing number of donors [13]. The reduction of modulation amplitude values of low-scale fluctuation from $\varepsilon_3^{\alpha}(x=0,01)=9,1$ meV to $\varepsilon_3^{\alpha}(x=0,05)=3,9$ meV and $\varepsilon_3^{\alpha}(x=0,10)=0,7$ meV is also possible only under condition of generation of donors, which reduces the semiconductor compensation degree [13].

Thus, the results of kinetic investigations of $Zr_{1-x}Ce_xNiSn$ allow speaking of the mechanism of generation of donors, which is possible under condition of the Ce^{4+}.

Thermoelectric power factor of $Zr_{1-x}Ce_xNiSn$

Fig. 7 represents a change in thermoelectric power factor $Z^*(x)$ of $Zr_{1-x}Ce_xNiSn$, from which it is evident that over the entire concentration range of *Ce* impurity atoms the values of $Z^*(x)$ are higher than in *n-ZrNiSn* undoped semiconductor. The result obtained is anticipated, as long as *n*-type semiconductor is doped with impurity atoms which generate donor structural defects in the crystal [8]. For the first time, the efficiency of thermal into electric energy conversion was improved [1] on doping of *n-ZrNiSn* with the atoms of rare-earth metal, since the property of *Ce* to change its valence state from 3+ to 4+ was utilized [7, 9].

In all fairness it should be noted that the values of $Z^*(x)$ of $Zr_{1-x}Ce_xNiSn$ rank below the record ones [14], but exactly this stimulates further research on the mechanisms and nature of structural defects generated in *n-ZrNiSn* semiconductor under heavy doping [13] and their influence on the mechanisms of electric conductivity.

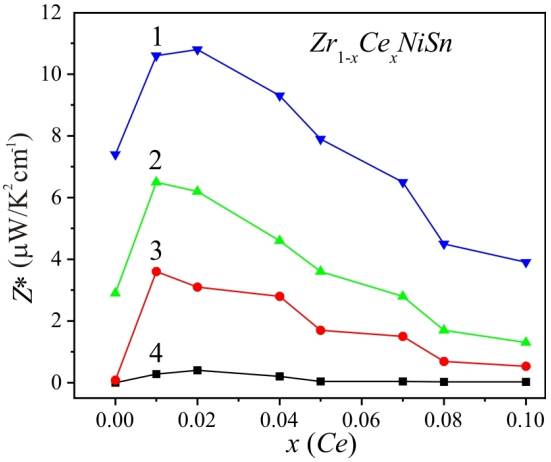

Fig. 7.Change in the values of thermoelectric power factor Z of $Zr_{1-x}Ce_xNiSn$: 1 – T = 380 K; 2 – T = 300 K; 3 – T = 250 K; 4 – T = 80 K*

Conclusions

For the first time, the increased values of thermoelectric power factor $Z^*(x)$ were obtained on doping of *n-ZrNiSn* with a rare-earth metal *Ce* as a result of realization of Ce^{4+} valence state that

generates donor structural defects in the crystal. A complicated mechanism of change in the compensation degree of $Zr_{1-x}Ce_xNiSn$ was revealed as a result of a simultaneous reduction of the number of donor defects (*Ni* in 4*a* position of *Zr* atoms) and generation in this same position of donor defects on substitution of *Zr* by *Ce* atoms in 4+ valence state. The investigated $Zr_{1-x}Ce_xNiSn$ solid solution is a promising thermoelectric material.

The work was performed in the framework of grants of the National Academy of Sciences and Ministry of Education of Ukraine, № 0113U007687 and № 0114U005464.

References

1. L.I.Anatychuk, Thermoelements and Thermoelectric Devices (Kyiv: Naukova Dumka, 1979), 768 p.
2. H.Hohl, A.P.Ramirez, C.Goldmann, G.Ernst, B.Wolfing, and E.Bucher, Efficient Dopants for *ZrNiSn*-based Thermoelectric Materials, *J. Phys. Condens. Matter*. **11**, 1697-1709 (1999).
3. A.Slebarski, M.Orzechowski, A.Wrona, J.Szade, and A.Jezierski, Structural Properties and Electronic Structure of Some Ternary *d*-electron and *f*-electron Intermetallics, *J. Phys. Condens. Matter*. **12**, 1269-1284 (2000).
4. S.Katsuyama, R.Matsuo, and M.Ito, Thermoelectric Properties of Half-Heusler Alloys $Zr_{1-x}Y_xNiSn_{1-y}Sb_y$, *J. Alloys Compd*. **428**, 262-267 (2007).
5. Yu.V.Stadnyk, V.A.Romaka, Yu.K.Gorelenko, L.P.Romaka, D.Fruchart, and V.F.Chekurin, Metal-Insulator Transition Induced by Changes in Composition in $Zr_{1-x}Sc_xNiSn$ Solid Solution Range, *J. Alloys Compd*. **400**, 29-32 (2005).
6. V.A.Romaka, V.V.Romaka, and Yu.V.Stadnyk, *Intermetallic Semiconductors: Properties and Applications* (Lviv, Lvivska Polytechnika, 2011), 488 p.
7. D.I.Khomsky, Problem of Intermediate Valence, *Advances in Physical Sciences* **129**(3), 443–485 (1979).
8. V.A.Romaka, D.Fruchart, Yu.V.Stadnyk, J.Tobola, Yu.K.Gorelenko, M.G.Shelyapina, L.P.Romaka, and V.F.Chekurin, A Condition of Maximum Power Characteristic to Intermetallic Semiconductors of the *MgAgAs* Structure Type, *Semiconductors* **40**(11), 1289-1395 (2006).
9. V.A.Romaka, Yu.N.Grin, Ya.P.Yarmolyuk, O.S.Zarechnyuk, and R.V.Skolozdra, Magnetic and Crystallographic Characteristics of R_2Ni_2Ga and R_2Ni_2Al Compounds, *The Physics of Metals and Metallography* **54**(4), 691-696 (1982).
10. T.Roisnel, J.Rodriguez-Carvajal, WinPLOTR: a Windows Tool for Powder Diffraction Patterns Analysis, *Mater. Sci. Forum, Proc. EPDIC7* 378-381, 118–123 (2001).
11. M.Schruter, H.Ebert, H.Akai, P.Entel, E.Hoffmann, and G.G.Reddy, First-Principles Investigations of Atomic Disorder Effects on Magnetic and Structural Instabilities in Transition-Metal Alloys, *Phys. Rev. B* **52,** 188-209 (1995).
12. V.L.Moruzzi, J.F.Janak, and A.R.Williams, *Calculated Electronic Properties of Metals* (NY, Pergamon Press, 1978), 348 p.
13. B.I.Shklovsky, A.L.Efros, *Electronic Properties of Doped Semiconductors* (Moscow: Nauka, 1979), 416 p.
14. S.R.Culp, S.J.Poon, N.Hickman, T.M.Tritt, and J.Blumm, Effect of Substitutions on the Thermoelectric Figure of Merit of Half-Heusler Phases at 800^0 C, *Appl. Phys. Letters* **88**(16), 042106-1-3 (2006).

Submitted 02.12.2014.

G.P. Gaidar

G.P. Gaidar, P.I. Baranskii

[1]Institute for Nuclear Research, NAS Ukraine,
47, Nauky Ave., Kyiv, 03680, Ukraine;
[2]V.E. Lashkaryov Institute of Semiconductor Physics,
NAS Ukraine, 45, Nauky Ave., Kyiv, 03028, Ukraine;

P.I. Baranskii

CONCENTRATION DEPENDENCES OF THE ANISOTROPY PARAMETER OF MOBILITY $K = \mu_\perp/\mu_\parallel$ AND THE ANISOTROPY PARAMETER OF ELECTRON-PHONON DRAG THERMOPOWER $M = \alpha_\parallel^{ph}/\alpha_\perp^{ph}$ IN *n-Ge* AND *n-Si*

In the range of $10^{12} \le n_e \le 2\cdot10^{15}$ cm^{-3} at $T = 83$ K the concentration dependences of the parameters of the mobility anisotropy $K = \mu_\perp / \mu_\parallel$ and the anisotropy of electron-phonon drag thermopower $M = \alpha_\parallel^{ph} / \alpha_\perp^{ph}$ in n-Ge single crystals were investigated and the significant distinctions in changes of these dependencies from the ones observed (in similar conditions) in n-Si single crystals were found. It was found that the n-Ge crystals are characterized by significantly higher (absolute) values of anisotropy parameters M and K in comparing with the corresponding values of these parameters for n-Si. It was shown that the parameter M in n-Ge (as distinct from n-Si) is insensitive to the presence of impurities in the crystals, but the parameter K monotonically decreases both in n-Ge and in n-Si with increasing the carrier concentration n_e.

Key words: germanium, silicon, the anisotropy parameter of mobility, the anisotropy parameter of thermopower, charge carrier concentration.

Introduction

Theory of kinetics of electronic processes in many-valley semiconductors [1] and general literature in this field (including that dedicated to experiments) [2–6] make wide use of two particularly important parameters, namely the anisotropy parameter of mobility $K = \mu_\perp / \mu_\parallel$ (where $\mu_\parallel$, $\mu_\perp$ are charge carrier mobilities along and across the long axis of isoenergetic ellipsoid, respectively) and the anisotropy parameter of electron-phonon drag thermopower $M = \alpha_\parallel^{ph} / \alpha_\perp^{ph}$ (where $\alpha_\parallel^{ph}$, $\alpha_\perp^{ph}$ are phonon components of electron-phonon drag thermopower along and across the long axis of isoenergetic ellipsoid, respectively).

The temperature dependence of the anisotropy parameter $K(T)$ for *n-Ge* crystals was experimentally studied in [7] and described on the basis of concepts related to the anisotropic type of relaxation time τ [8, 9]. Under the assumption concerning the anisotropic character of relaxation time the anisotropy parameter of scattering K_τ (hence, K) is largely defined by the contribution of impurity scattering which (at given crystal temperature) is equivalent to dependence of K on the impurity concentration in the bulk of the crystal. Reduction of both M and K in *n-Si* single crystals with a rise in temperature from 77.4 K to 350 K was found in [10].

In [11], by measuring the saturation of longitudinal magnetoresistance $\rho_H^\parallel / \rho_0$ in *n-Ge* in strong ($\frac{\mu H}{c} >> 1$) magnetic fields (up to 250 кЕ) the concentration dependence of the anisotropy parameter of mobility *K* was studied in the range of $5 \cdot 10^{13} \le n_e \equiv N_{Sb} \le 1.38 \cdot 10^{17}$ cm^{-3}, and comparison of the experimental data to the results of theoretical calculations of dependence $K = f(n_e)$ performed within the anisotropic scattering theory yielded their quantitative fit.

The concentration dependence of the anisotropy parameter of electron-phonon drag thermopower $M = \alpha_\parallel^{ph} / \alpha_\perp^{ph} = f(n_e)$ for *n-Si* single crystals was studied in [12]. Different authors with the aid of different methods found the value of *M* parameter for *n-Ge* as well, but only for conditions of preferably phonon scattering [13–15].

However, taking into account that instrument making utilizes silicon and germanium doped with impurities in a wide concentration range, in the calculation of various effects in such crystals (especially in the calculation of thermoelectric and thermomagnetic effects on the basis of anisotropic scattering theory generalized in [16] for the case of electron-phonon drag and elastic deformation) one must also know the values of parameters *K* and *M* in mixed scattering area.

The objective of this paper was to study changes in the anisotropy parameter of mobility $K = \mu_\perp / \mu_\parallel$ and the anisotropy parameter of electron-phonon drag thermopower $M = \alpha_\parallel^{ph} / \alpha_\perp^{ph}$ with increase in concentration $n_e \equiv N_d$ in *n-Ge* and *n-Si* in the range of charge carrier concentration $10^{12} \le n_e \equiv N_d \le 3 \cdot 10^{16}$ cm^{-3} at temperature $T = 83$ K.

Results and discussion

The value of parameter *K* is known to be experimentally obtained (see, e.g. [17]) from the data on tensoresistance using the relation

$$K = \frac{3}{2} \frac{\rho_\infty^{\langle ijk \rangle}}{\rho_0} - \frac{1}{2}, \tag{1}$$

where ρ_0, $\rho_\infty^{\langle ijk \rangle}$ is resistivity of undeformed $\rho(X = 0) \equiv \rho_0$ and uniaxially elastically deformed $\rho(X \to \infty) \equiv \rho_\infty$ (ρ_∞ corresponds to saturation region of function $\rho = \rho(X)$) crystal in crystallographic direction $\langle i\ j\ k \rangle$ (i.e. under conditions $\vec{X} \parallel \vec{J} \parallel \langle i\ j\ k \rangle$, where *X* is mechanical load, *J* is current; and $\langle i\ j\ k \rangle \to \begin{cases} \langle 111 \rangle & - \text{ for } n\text{-}Ge \\ \langle 100 \rangle & - \text{ for } n\text{-}Si \end{cases}$

As regards parameter *M*, similarly to *n-Ge* in [18], for *n-Si*, elastically deformed in the direction of [001] // ∇T // $\vec{X}$, on the basis of general expressions represented in [16], we shall write

$$\alpha - \alpha^e = \alpha_\perp^{ph} \frac{M + \gamma \frac{8K + M}{3}}{1 + \gamma \frac{8K + 1}{3}}, \tag{2}$$

where γ is the relation of charge carrier concentration in the ascending minima to charge carrier concentration in the descending minima, α is experimentally measured thermopower value in phonon

drag region, $\alpha^e = \frac{k}{e}\left[2 + \ln \frac{2\left(2\pi m^* kT\right)^{3/2}}{n_0 h^3}\right]$ is electron (diffusion) thermopower component which is calculated by the Pisarenko formula; n_0 is charge carrier concentration; e is electron charge; k is the Boltzmann constant; T is temperature; h is the Planck constant; $m^* = N^{3/2}\sqrt[3]{m_\parallel m_\perp^2}$ is density-of-state effective mass; N is the number of isoenergetic ellipsoids.

From expression (2) for boundary cases $X = 0$ (absence of deformation) and $X \to \infty$ (corresponding to X values assuring complete transition of carriers to the descended minima) we obtain a system of equations

$$\left.\begin{aligned} \alpha_0^{ph} &\equiv \alpha_0 - \alpha^e = \alpha_\perp^{ph}\frac{M + 2K}{1 + 2K} \\ \alpha_\infty^{ph} &\equiv \alpha_\infty - \alpha^e = \alpha_\perp^{ph} \cdot M \equiv \alpha_\parallel^{ph} \end{aligned}\right\}, \tag{3}$$

where α_0 and α_∞ are thermopower values in the undeformed and deformed samples, respectively; α_0^{ph} and α_∞^{ph} are phonon components of thermopower measured in the undeformed and elastically deformed crystal; $\alpha_{(0\ or\ \infty)} = \alpha_{(0\ or\ \infty)}^{ph} + \alpha_{(0\ or\ \infty)}^{e}$.

Excluding $\alpha_\perp^{ph}$ from the system of equations (3), we obtain for *n-Si* crystals (just as for *n-Ge*):

$$M = \frac{2K}{(2K+1)\dfrac{\alpha_0 - \alpha^e}{\alpha_\infty - \alpha^e} - 1} = \frac{2K}{(2K+1)\dfrac{\alpha_0^{ph}}{\alpha_\infty^{ph}} - 1}\ . \tag{4}$$

Table 1 gives characteristics of samples under study and the results of processing the experimental and calculated data to determine the anisotropy parameter of electron-phonon drag thermopower M in *n-Ge* at $9.8 \cdot 10^{11} \le n_e \le 1.7 \cdot 10^{15}$ cm^{-3}. The values of the anisotropy parameter K were obtained from the data on tensoresistance with the use of expression (1) for *n-Ge*.

Table 1

Characteristics of n-Ge samples under study at temperature T = 83 K under conditions of $\vec{X}$ *// ∇T // [111] and X ≥ 0.6 GPa*

Sample №	n_e, cm^{-3}	α^e, μV/K	$\alpha_\parallel^{ph}$, μV/K	$\alpha_\perp^{ph}$, μV/K
1	$9.8 \cdot 10^{11}$	1395	9205	751
2	$1.6 \cdot 10^{13}$	1159	7921	702
3	$1.6 \cdot 10^{13}$	1152	7348	617
4	$6.9 \cdot 10^{13}$	978	7282	632
5	$1.7 \cdot 10^{15}$	757	5668	505

It was shown that at $T = 83$ K the anisotropy parameter of electron-phonon drag thermopower $M = \alpha_\parallel^{ph} / \alpha_\perp^{ph}$, measured by tensothermopower (i.e. in the absence of a magnetic field) is practically independent of concentration, as is evident from Fig. 1, though all components of the right-

hand side of formula (4) (namely : K, α_0^{ph}, α_∞^{ph} and even α^e that does not appear in (4) directly, but was used in the system of equations (3) when finding the phonon components of electron-phonon drag thermopower α_0^{ph} i α_∞^{ph}) are essentially dependent on $n_e \equiv N_d$.

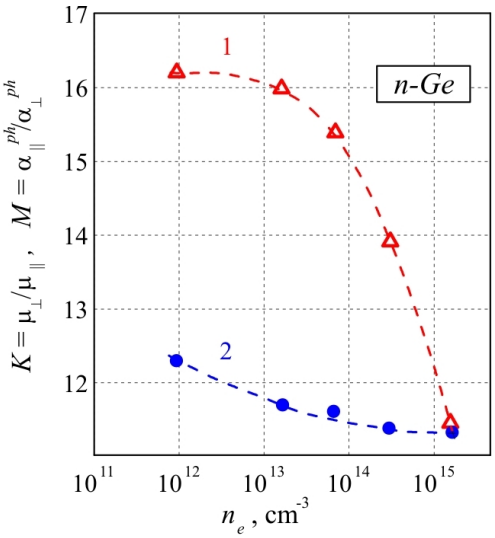

Fig. 1. Concentration dependences of the anisotropy parameter of mobility $K = f(n_e)$ *(1) and the anisotropy parameter of electron-phonon drag thermopower* $M = f(n_e)$ *(2) in n-Ge single crystals at T = 83 K.*

Thus, the anisotropy parameter of mobility K with increase in concentration from $9.8 \cdot 10^{11}$ to $1.7 \cdot 10^{15}$ cm^{-3} (i.e. approximately 2000 times) is constantly reduced from 16.2 to 11.4 (by a factor of 1.42), whereas the anisotropy parameter of electron-phonon drag thermopower M is reduced only by a factor of ~ 1.088 (actually, a change of M in *n-Ge* is as low as 9 %), as illustrated in Fig. 1.

It may be considered that within the accuracy of performed investigations parameter M practically remains invariable and uniform $M = \alpha_\parallel^{ph} / \alpha_\perp^{ph} \cong 11.7 \pm 0.3$ at measurement temperature $T = 83$ K. Thus, unlike the anisotropy parameter of mobility K formed by combination of electron scattering mechanisms on crystal lattice vibrations and on impurity centres, the phonon part of thermopower (to be more precise, its anisotropy, that is, the ratio $M = \alpha_\parallel^{ph} / \alpha_\perp^{ph}$) is practically independent of concentration $n_e \equiv N_d$ (in any case, under investigation limits $9.8 \cdot 10^{11} \div 1.7 \cdot 10^{15}$ cm^{-3}) and is fully defined by atomic vibrations in crystal lattice sites.

In weakly doped crystals, when scattering on crystal lattice vibrations is practically dominant, the ratio ρ_X / ρ_0, in any case within the concentration range $10^{12} \le n_e \equiv N_d \le 10^{14}$ cm^{-3}, is free from prominent impurity influence [10, 19], it would be interesting to compare the values of K obtained at crystal deformation in different crystallographic directions.

With this objective, to determine the anisotropy parameter of mobility $K = \mu_\perp / \mu_\parallel$, not only relation (1) was used with the values of $\langle i\ j\ k \rangle \to \langle 111 \rangle$, but also the relation

$$K = 3 \cdot \frac{\rho_\infty^{\langle 111 \rangle}}{\rho_\infty^{\langle 110 \rangle}} - 2, \qquad (5)$$

which is associated with the necessity of measuring resistivity ρ in two crystallographic directions of *n-Ge*

samples. Moreover, $\rho_\infty^{\langle 111\rangle} = \lim_{X\to\infty} \rho(X)$ and $\rho_\infty^{\langle 110\rangle} = \lim_{X\to\infty} \rho(X)$ are resistivity values at uniaxial elastic deformation X assuring complete migration of current carriers to energy minima located in the direction of deformation axis (<111> or <110>).

For experiment set up, two series of *n-Ge* samples were used (four samples in each) with charge carrier concentrations $1.5 \cdot 10^{13}$ and $9.5 \cdot 10^{13}$ cm^{-3}, respectively. Two samples of each series were cut in crystallographic direction [111], and the other two – in [110] direction. Changes in tensoresistance of *n-Ge* crystals were measured at temperature 77.4 K. The results of the experiments were summarized in Table 2.

Table 2

Results of processing the experimental data on tensoresistance obtained at T = 77.4 K on n-Ge samples of different doping level under conditions of $\vec{X}$ *//* $\vec{J}$ *//[111] and* $\vec{X}$ *//* $\vec{J}$ *//[110]*

Series №	n_e, cm^{-3}	$\rho_\infty^{[111]} / \rho_0$	$\rho_\infty^{[111]} / \rho_\infty^{[110]}$	$K = \mu_\perp / \mu_\parallel$, found by formula (1)	$K = \mu_\perp / \mu_\parallel$, found by formula (5)
1	$1.5 \cdot 10^{13}$	10.93	6.0	15.9	16.0
2	$9.5 \cdot 10^{13}$	10.26	5.66	14.98	15.0

It was established that the numerical values of the anisotropy parameter of mobility *K*, found by using the relation (1), as well as formula (5), coincide. This, in turn, means that at deformation of *n-Ge* in crystallographic directions [111] and [110] the isoenergetic ellipsoids are only displaced in the energy scale, remaining practically undeformed (as ellipsoids of revolution).

Besides, as is evident from the experiments performed, the identity of values of the anisotropy parameter of mobility *K* is retained not only with different production methods (i.e. with the use of various formulae), but this statement also remains valid in going from one to another (higher) charge carrier concentration (see Table 2).

On *n-Si* single crystals, experimental study of the anisotropy parameter of electron-phonon drag thermopower *M* and the anisotropy parameter of mobility *K* was performed at $T = 83$ K and $1.9 \cdot 10^{13} \le n_e \le 2.6 \cdot 10^{16}$ cm^{-3} (characteristics of samples are given in Table 3).

Table 3

Characteristics of n-Si samples investigated at temperature T = 83 K under conditions of $\vec{X}$ *//* ∇T *// [001] and X ≥ 0.6 GPa*

Sample №	n_e, см$^{-3}$	$\mu_{H_{77\,K}}$, cm^2/ V·s	ρ_{300K}, Ω·cm	α^e, μV/K	$\alpha_\parallel^{ph}$, μV/K	$\alpha_\perp^{ph}$, μV/K
1	$1.9 \cdot 10^{13}$	19250	230	1227	30770	4650
2	$1.29 \cdot 10^{14}$	18700	27.7	1063	27440	4530
3	$6.55 \cdot 10^{14}$	14550	4.16	923	20180	3500
4	$2 \cdot 10^{15}$	9290	0.9	827	17670	3350
5	$6.21 \cdot 10^{15}$	6370	0.245	729	15530	3530
6	$2.60 \cdot 10^{16}$	1790	0.054	606	7640	2350

Measuring tensoresistance $\rho_X = f(X)$ and tensothermopower $\alpha_X = \varphi(X)$ on *n-Si* crystals under conditions $\vec{X} \,//\, \vec{J} \,//\, [001]$ and $\vec{X} \,//\, \nabla T \,//\, [001]$ (typical appearance of this data is represented for one of investigated silicon samples in Fig. 2), as well as subtracting from α_0 and α_∞ the diffusion component α^e (which is practically independent of *X*) in expression (4), we find parameter *M* for each sample.

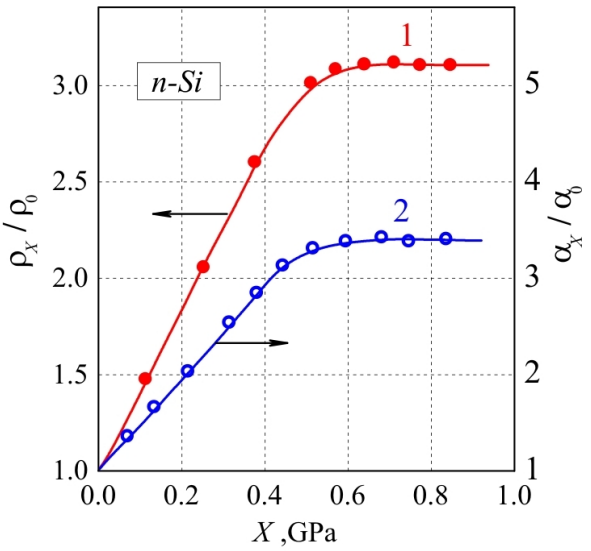

Fig. 2. Typical dependences of tensoresistance ρ_X / ρ_0 *(1) and tensothermopower* α_X / α_0 *(2) on mechanical load X for n-Si.*

The value of parameter *K* will be obtained from the experimental data on tensoresistance and expression (1) for *n-Si*.

The concentration dependences of the anisotropy parameter of mobility $K = \mu_\perp / \mu_\parallel$ and the anisotropy parameter of electron-phonon drag thermopower $M = \alpha_\parallel^{ph} / \alpha_\perp^{ph}$ for *n-Si* single crystals at $T = 83$ K are given in Fig. 3.

Note that as long as electron-phonon drag thermopower is proportional to the mean free path of long-wave phonons (l^{ph}) [20], the experimentally observed reduction of $M = \alpha_\parallel^{ph} / \alpha_\perp^{ph}$ (due to a more efficient reduction of $\alpha_\parallel^{ph}$ than $\alpha_\perp^{ph}$ with increasing $n_e \equiv N_d$) results from "cutting" of l^{ph} by growing efficiency of phonon scattering on impurity atoms.

Reduction of the anisotropy parameter of mobility $K = \dfrac{\mu_\perp}{\mu_\parallel} = \dfrac{K_m}{K_\tau} = \dfrac{m_\parallel}{m_\perp} \dfrac{\langle \tau_\perp \rangle}{\langle \tau_\parallel \rangle}$ in multi-valley semiconductors with growing contribution of impurity scattering is due to increase in scattering anisotropy, as long as impurity scattering in such semiconductors as silicon and germanium is fairly anisotropic. Exactly this results in the reduction of tensoresistivity $\rho_{X\to\infty}^{[001]}$ (in case of *n-Si* (Fig. 3)) and $\rho_{X\to\infty}^{[111]}$ values (in case of *n-Ge* (Fig. 1)) with increase in doping level of silicon and germanium crystals and in the monotonic decrease (in both cases) of parameter *K* with increasing concentration of charge carriers n_e. Note that scattering conditions in crystals are defined by several basic factors, namely the concentration of scatterers, their structure and arrangement in crystal lattice.

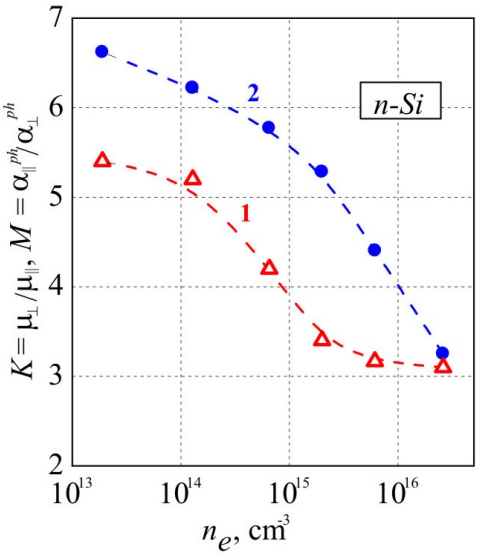

Fig. 3. Concentration dependences of the anisotropy parameter of mobility $K = f(n_e)$ *and the anisotropyparameter of electron-phonon drag thermopower* $M = f(n_e)$ *(2) in n-Si single crystals at T = 83 K.*

Comparison of data for *n-Ge* and *n-Si* samples represented in Fig. 1 and Fig. 3 points to considerably higher (absolute) values of *M* and *K* that characterize *n-Ge* single crystals as compared to corresponding values for *n-Si*. This is primarily related to higher anisotropy of charge carriers effective mass in *n-Ge* than in *n-Si* ($\frac{m_\parallel}{m_\perp} = \frac{1.58}{0.082} \cong 19.3$ – in *n-Ge* and $\frac{0.91}{0.191} \cong 4.75$ – in *n-Si*) which brings about the appearance of essentially different scattering conditions in *n-Ge* and *n-Si* crystals, as well as to significant difference in the arrangement of isoenergetic ellipsoids with respect to crystal axes in germanium and silicon.

Conclusions

1. Formulae (1), (4) and (5), convenient for processing the experimental data obtained when measuring changes in the resistivity and thermopower in directionally elastically deformed *n-Ge* and *n-Si* single crystals of known crystallographic orientation are given.
2. In a wide range of charge carrier concentrations n_e ($10^{12} \div 3 \cdot 10^{16}$ cm^{-3}) in *n-Ge* and *n-Si* single crystals the anisotropy parameter of mobility $K = \mu_\perp / \mu_\parallel$ and the anisotropy parameter of electron-phonon drag thermopower $M = \alpha_\parallel^{ph} / \alpha_\perp^{ph}$ was studied at temperature $T = 83$ K on samples of known crystallographic orientation. Changes in the investigated parameters *K* and *M* with increase in doping degree of germanium and silicon crystals by donor-type impurity were obtained. It was shown that parameter *M* in *n-Ge* (unlike *n-Si*) is low-sensitive to the presence of impurities in crystals, however, parameter *K* is monotonically decreased both in *n-Ge* and in *n-Si* with increase in charge carrier concentration n_e.
3. It was established that *n-Ge* single crystals are characterized by much higher (absolute) values of the anisotropy parameters *M* and *K*, as compared to the respective values for *n-Si*.

References

1. P.I.Baranskii, I.S.Buda, and I.V.Dakhovsky, *Theory of Thermoelectric and Thermomagnetic Effects in Anisotropic Semiconductors* (Kyiv, Naukova Dumka, 1987), 272 p.
2. P.I.Baranskii, O.E.Belyayev, G.P.Gaidar, V.P.Gaidar, V.P.Kladko, and A.V.Kuchuk, *Problems of Diagnostics of Real Semiconductor Crystals* (Kyiv: Naukova Dumka, 2014), 462 p.
3. G.P.Gaidar, P.I.Baranskii, Thermoelectric Properties of Transmutation Doped Silicon Crystals, *Physica B: Condensed Matter*. **441**, 80–88(2014).
4. P.I.Baranskii, G.P.Gaidar, Some Thermoelectric Features of Conventional and Transmutation Doped Silicon Crystals, *J.Thermoelectricity* **1**, 5–12 (2012).
5. P.I.Baranskii, A.V.Fedosov, and G.P.Gaidar, *Semiconductor Inhomogeneities and Critical Tasks of Defects Interaction in Radiation Physics and Nanotechnology* (Kyiv-Lutsk, Lutsk State Technical University, 2007), 316 p.
6. P.I. Baranskii, I.S. Buda, I.D. Dakhovsky, and V.V. Kolomoyets, *Electric and Galvanomagnetic Effects in Anisotropic Semiconductors* (Kyiv: Naukova Dumka, 1977), 270 p.
7. R.A.Laff, H.Y.Fan, Magnetoresistance in *n*-Type Germanium at Low Temperatures, *Phys. Rev.* **112**(2), 317–321 (1958).
8. C.Herring, E.Vogt, Transport and Deformation-Potential Theory for Many Valley Semiconductors with Anisotropic Scattering, *Phys. Rev*. **101**(3), 944–961 (1956).
9. I.V. Dakhovsky, Anisotropic Scattering of Electrons in Germanium and Silicon, *Physics of the Solid State* **5**(8), 2332 – 2338 (1963).
10. P.I.Baranskii, V.V.Savyak, and Yu.V.Simonenko, Temperature Dependence of Phonon Drag ThermoEMF Anisotropy in Uniaxially Deformed *n-Si, Semiconductors* **18**(6), 1059–1063 (1984).
11. V.M.Babych, P.I.Baranskii, Concentration Dependence of the Anisotropy Parameter *K* in *n*-Germanium, *Semiconductors*. **1**(7), 1029–1032 (1967).
12. P.I.Baranskii, S.L.Korolyuk, and P.G.Ostafiychuk, Concentration Dependence Concentration Dependence of Phonon Drag ThermoEMF Anisotropy in *n-Si, Semiconductors* 18(11), 2053–2056 (1984).
13. C.Herring, T.H.Geballe, and J.E.Kunzler, Analysis of Phonon Drag Thermomagnetic Effects in *n*-Type Germanium, *Bell System Tech. J.* **38**(3), 657–747 (1959).
14. P.I.Baranskii, I.S.Buda, V.V.Kolomoyets, A.G.Samoilovich, and B.A.Sus, Study of Electron Phonon Drag Effect Anisotropy in *n-Ge, Semiconductors* **8**(11), 2159–2163 (1974).
15. I.S.Buda, V.V.Kolomoyets, B.A.Sus, and L.A.Scherbina, Determination of Drag ThermoEMF Anisotropy Parameter in *n-Ge, Ukrainian J. of Physics* **22**(8), 1375–1378 (1977).
16. A.G.Samoilovich, I.S.Buda, Influence of Elastic Deformations on ThermoEMF in *n-Ge* in Drag Effect Region, *Semiconductors* **3**(3), 400–408 (1969).
17. P.I.Baranskii, A.V.Fedosov and G.P.Gaidar, *Physical Properties of Silicon and Germanium Crystals in the Fields of Effective External Influence* (Nadstyria, Lviv, 2000).
18. P.I.Baranskii, G.P.Gaidar, Anisotropy of Electron-Phonon Drag ThermoEMF in *n-Ge*, *J. Thermoelectricity* **2**, 29–38 (2012).
19. P.I.Baranskii, I.S.Buda, I.V.Dakhovsky, V.V.Kolomyets, and A.G.Samoilovich, Piezoresistance of *n-Ge* in [111] Direction under Mixed Scattering Conditions, *Semiconductors* **8**(5), 984–986 (1974).
20. L.S.Stilbance, *Physics of Semiconductors* (Sov. Radio, Moscow, 1967).

Submitted 22.11.2014.

Yu. M. Lobunets

Yu. M. Lobunets

Institute of Thermoelectricity NAS and MES of Ukraine
1, Nauky Str., Chernivtsi, 58029, Ukraine

HEAT EXCHANGE-TYPE TEG FOR MARINE PROPULSION PLANTS

The characteristics of heat exchange-type thermoelectric generators using the exhaust gas heat of marine engines are analyzed. The prospects of using such TEG are outlined.

Key words: thermoelectric generator, low-grade heat source, marine propulsion plants

Introduction

There is a wealth of papers on the subject of using thermoelectric generators (TEG) for the recovery of exhaust gas energy of automobile internal combustion engines. This line is considered to be one of promising spheres of TEG application [1-8]. However, the use of TEG in similar schemes on water transport is more attractive due to the absence of essential restrictions typical of automobile transport. The advantages of such use are listed in [7]:

- much higher powers of propulsion plants;
- much greater scope of saving energy resources;
- much better cooling conditions (outside water);
- absence of weight and size limitations;
- numerous options of recovery schemes;
- TEG unification capability allowing their use for any type of ship.

Conditions of using TEG on ships are essentially different from those on automobile transport, so these applications require special developments. With regard to high power of propulsion plants, conventional schemes of automobile TEG with arrangement on the exhaust pipe are unsuitable for marine propulsion plants. Schemes with the use of cassette-type thermopiles that are arranged in exhaust gas flow [8] or schemes with intermediate heat carrier [4] are discussed. Schemes using phase transitions for thermal energy transportation, i.e. heat pipes [5] or two-phase thermosiphons [3], where thermopiles are heated by heat carrier steam condensed on their surface (Fig.1) also seem to be rather efficient.

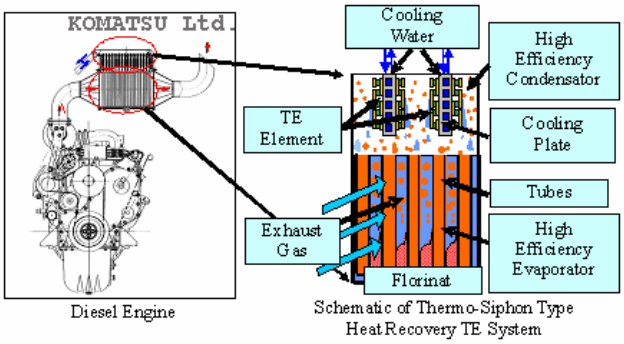

Fig.1. Schematic of TEG with a two-phase thermosiphon [3]

In my opinion, the scheme of heat exchange-type TEG proposed in [9] is most efficient for the application under study. It permits the use of both liquid and steam-like heat carriers, provides for the highest specific power and is well adapted into the flowchart of propulsion plant. The basic peculiarities of such TEG combined with a marine propulsion plant are considered and the technical and economic features of this scheme are analyzed.

Scheme of heat exchange-type TEG for diesel propulsion plant

Distribution of energy fluxes in a marine diesel engine is illustrated in Fig.2 from which it follows that about 25% of primary energy is lost with exhaust gases. Normally, gas temperature is approximately 500°C.

TEG under study is schematically represented in Fig.3.

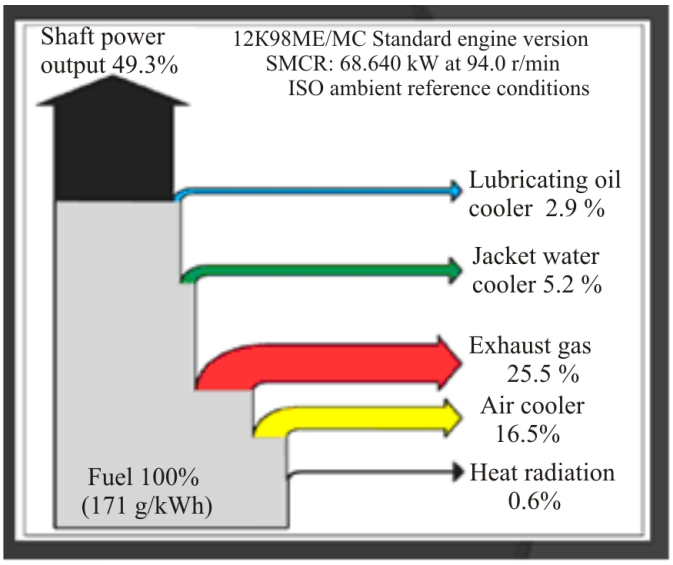

Fig.2. Distribution of energy fluxes in a marine diesel engine [7]

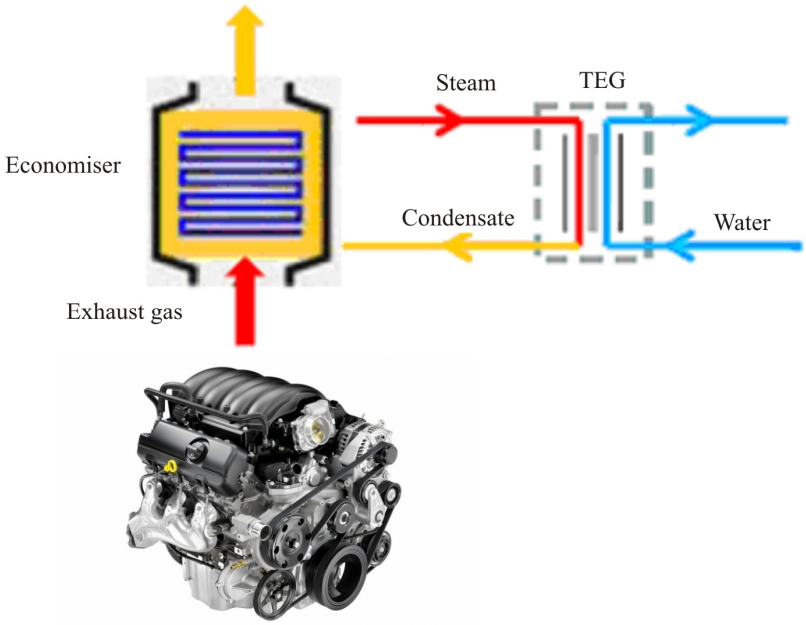

Fig.3. Schematic of TEG for a marine propulsion plant

Exhaust gases with temperature t_{hg}=500°C from the engine come to heat exchanger-economizer where heat carrier coming from TEG is heated to boiling point. Steam with temperature t_{ho} comes to channels formed by thermopiles where it is condensed and returns to economizer. Cooling of thermopiles is done by outside water with temperature t_{xo} that circulates through TEG channels. Packing of thermopiles to prevent leakage of heat carriers is done by gaskets of special shape that form channels and collectors for passage of heat carriers.

The operating temperature of heat carrier at inlet to TEG t_{ho} is easily controlled by maintaining the necessary pressure in the system. The choice of this parameter in the available temperature range $t_{xo}<t_{ho}<t_{hg}$ strongly affects system efficiency and TEG power. It is clear that with a rise in t_{ho}, the amount of heat taken from exhaust gas (Q_h) is reduced, just as the efficiency of heat exchanger K_{heat} and the amount of heat carrier generated by economizer (G_h). At $t_{ho} \rightarrow t_{hg}$; $Q_h \rightarrow 0$; $K_{heat} \rightarrow 0$. Alongside with that, the operating temperature difference on thermoelements and, accordingly, TEG efficiency is increased. When affected by these factors, TEG power reaches a maximum within the available temperature range (Fig.4). As is seen from the presented data, in the first approximation the operating temperature $t_{ho}=(t_{hg}-t_{xo})/2$ is optimal. In our case this corresponds to approximately t_{ho}= 250°C.

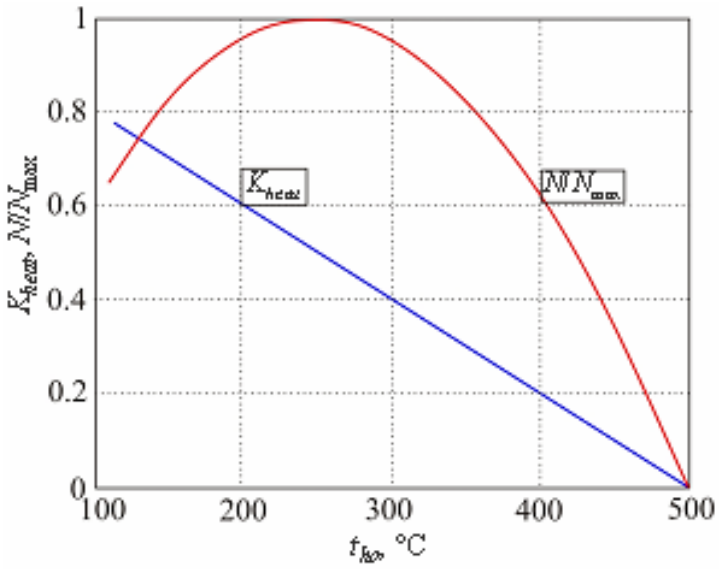

Fig.4. Heat exchanger efficiency K_{heat} and TEG power N versus heat carrier input temperature t_{ho}

Another restriction imposed on heat carrier temperature is permissible operating temperatures of thermoelectric material and structural components. For the scheme under consideration, critical at the moment is maximum permissible operating temperature of sealing gaskets which for stock-produced items is 180°C.

Mathematical model of TEG

In view of the fact that heating of TEG is due to phase transitions (condensation), the temperature of hot thermoelement junctions along the channels can be considered constant. The availability of unrestricted source of cooling water allows making an assumption as to slight temperature changes along the cold channels of TEG. In this case it will be correct to use a mathematical model of thermoelement under third-order boundary conditions, taking no account of

temperature changes along the thermopiles. According to [10], the equation for temperature distribution in TEG will be written as below:

$$\Theta(Y) = C_1 + C_2 Y - \frac{J^2}{2I_0 Y^2}. \tag{1}$$

Constants C_1, C_1 are determined as:

$$C_1(J + Bi_x) - C_2 = Bi_x \vartheta_x, \tag{2}$$

$$C_1(Bi_h - J) + C_2(Bi_h - J + 1) = Bi_h \vartheta_h + \frac{J^2}{I_0}(1 + \frac{Bi_h - J}{2}),$$

Where:

$\Theta = \frac{T}{T_p}$ is dimensionless thermoelement temperature;

$\vartheta = \frac{t}{T_p}$ is dimensionless heat carrier temperature;

$I_0 = zT_p$ is the Ioffe criterion;

$Bi = \frac{h}{\lambda R_t}$ is the Biot criterion;

$J = \frac{jeh}{\lambda}$ is dimensionless current density.

Indexes *h* and *x* refer to the hot and cold TEG sides, respectively.

In the above expression for the Biot criterion, coefficient R_t characterizes a sum of thermal resistances on the way of heat flux from thermoelement surface to heat carrier, that is

$$Rt = \frac{1}{\alpha} + \sum_i \frac{h_i}{\lambda_i}, \tag{3}$$

where α is heat exchange coefficient between heat carrier and thermopile; h_i and λ_i is the thickness and thermal conductivity of each layer on the way of heat flux (connecting elements, heat spreaders, thermopile package, solder layers, etc).

As long as a system of equations (1– 3) is nonlinear, we shall solve it by numerical methods.

Owing to the fact that in this schematic the isothermal conditions are assured on thermopile surfaces, for its calculation and analysis it is sufficient to consider the characteristics of one module with defined properties under the above conditions. Maximum power of such module in the general case is:

$$N_m = \frac{E^2}{4R}, \tag{4}$$

Where $E = n_v e(T_h - T_c)$ is module EMF; $R = n_v \frac{\rho h}{s}$ is its electrical resistance.

In view of the above, let us determine the characteristics of TEG scheme under study with the following input data:

- diesel plant power P = 1 MW (gas enthalpy Q_h =500 kW);
- warming heat carrier temperature at inlet to TEG t_{ho} = 180°C;
- water temperature in cooling system t_{xo}= 15°C;
- water velocity in TEG cooling channels - V_x= 2 m/s;
- heat exchanger efficiency will be determined from known t_{ho} as K_{heat}= (t_{hg} - t_{ho})/t_{hg}= 0.64;
- figure of merit of thermoelectric material z = 0.0026K^{-1};
- number of thermoelements in modules n_v = 526;
- thermoelement cross-section s = 0.026 cm^2;
- thermal resistance Rt_x=1.7 cm^{2}K/W; Rt_h=1.5 cm^{2}K/W.

According to (1-4), characteristics of TEG scheme are determined by the available temperature difference Δt_o=t_{ho}-t_{xo}, the properties of thermoelectric material *Io*, heat exchange conditions *Rt* and module characteristics -n_v, *h, s*. The majority of said parameters is determined by problem formulation conditions and has fixed values. Only module characteristics can be considered as independent parameters that can be varied over a wide range. With regard to the fact that the impact of n_v and s is of extensive nature, only thermoelement height h should be referred to independent parameters. The impact of height lies in the fact that it determines thermal (R_o=h/λ) and electric (R) resistance of thermoelements. Increase in h leads to increase in thermal resistance and useful temperature difference, at the same time, the electric resistance of module is increased which has a negative impact on its power. As a result, one can always find the optimal value of h that assures maximum module power (Fig.5a). The dependence of module efficiency on h is monotonic, since increase in thermoelement thermal resistance simultaneously results in temperature difference increase and reduction of heat flux through thermoelements (Fig.5b).

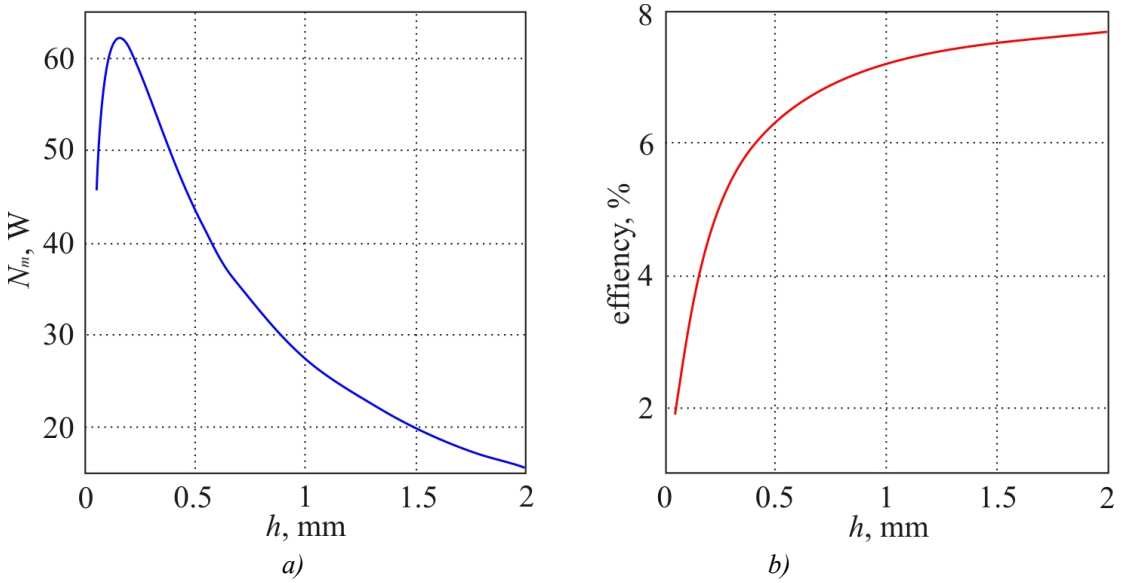

Fig.5. Power (a) and efficiency (b) of module versus thermoelement height

Analysis of the task shows that the optimal ratio between thermal resistances of thermoelement R_o and heat transfer R_t is constant and always equals to R_o/R_t =2 (Fig.6). As a consequence, maximum power mode is realized at temperature difference which is equal to half of the available (Fig.7). It is clear that R_t increase brings about the respective reduction of maximum power.

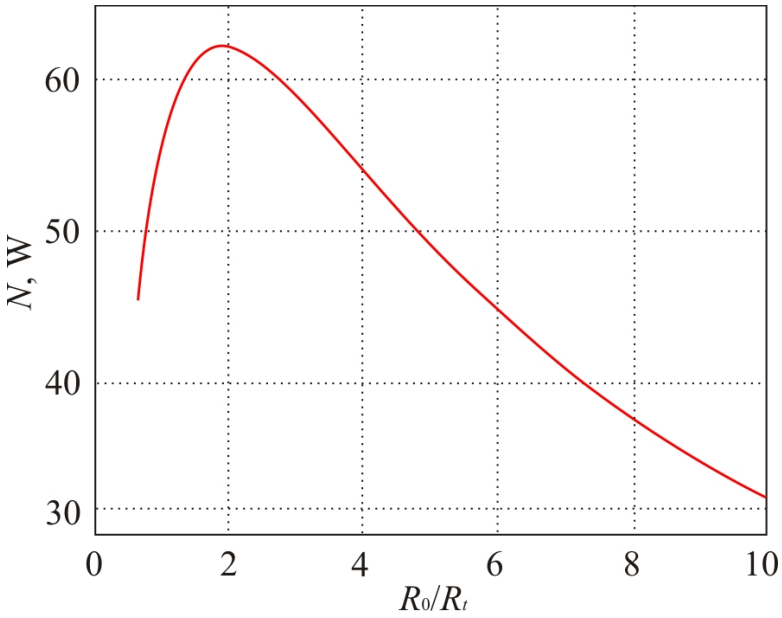

Fig.6. Module power versus the ratio between thermal resistances of thermoelement R_o and heat transfer R_t

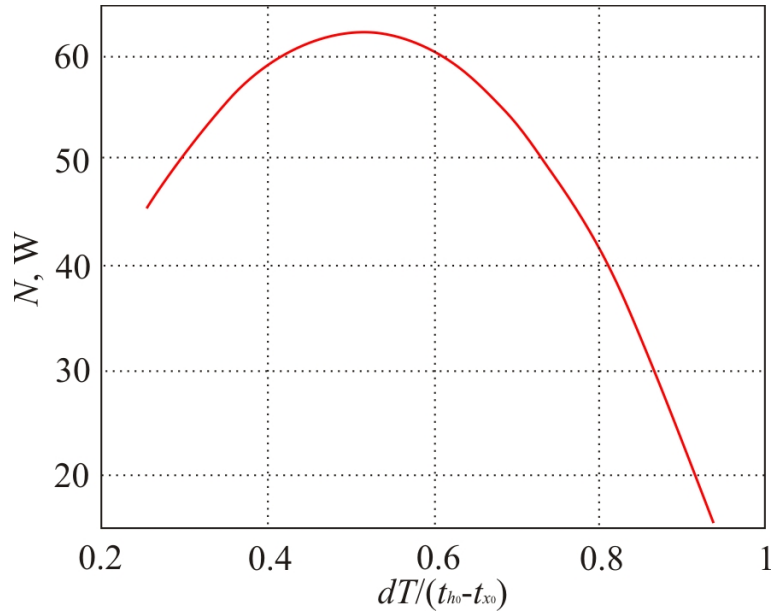

Fig.7. The ratio between module power N and temperature difference which is a function of height ΔT= f(h)

Knowing heat flux through the module Q_m, the total number of modules in TEG can be determined as

$$n_m = Q_h K_{heat} / Q_m . \quad (5)$$

The total power of TEG is, accordingly

$$NS = n_m N . \quad (6)$$

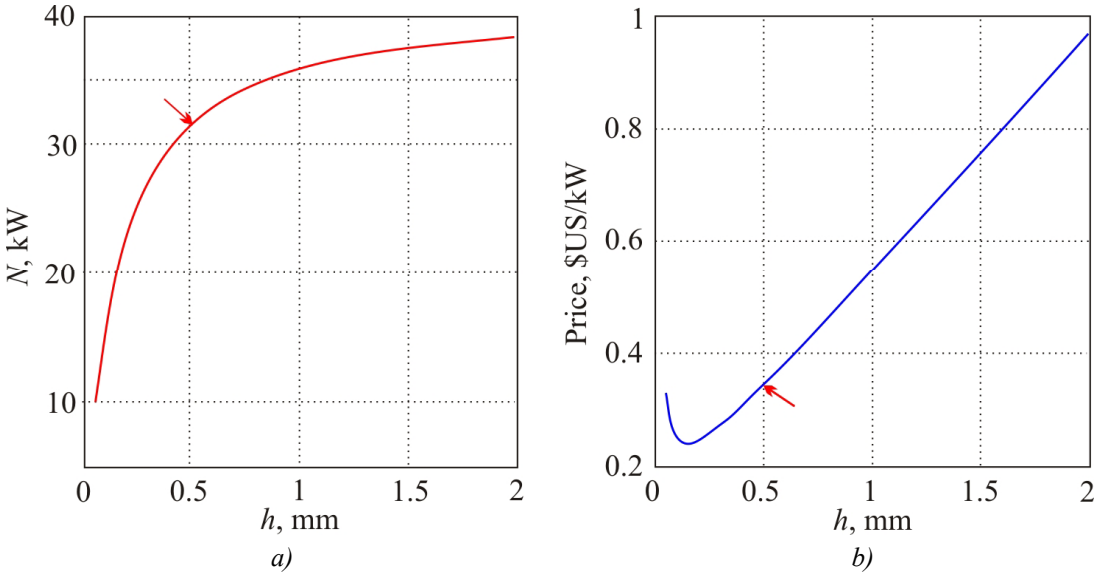

Fig.8. Power (a) and unit cost of TEG (b) versus thermoelement height

As is apparent from the data given in Fig.8a, despite the availability of extreme point on the curve $N=f(h)$, a dependence of total TEG power on thermoelement height is monotonic and similar to efficiency dependence. At the same time, it should be borne in mind that at $h>h_{opt}$ the necessary number of modules, hence, the cost of TEG increases considerably (Fig.8b). It is evident that a compromise solution should be the choice of h in the zone of acceptable TEG cost, close to boundary value line N, as marked by arrows in Fig.8. With this approach, the scheme of TEG under study assures quite acceptable values of unit cost (on the level of 350 $US/kW) and efficiency (close to 5%). One should also note high specific power of such generator – according to our estimates the above TEG will have the dimensions about 250×700×300 mm. These figures do not take into account the cost and dimensions of heat exchanger-economizer. To estimate possible scope of using such TEG, it can be noted that marine vessels of medium class have propulsion plants 10...15 MW. That is, for instance, using the above scheme of TEG on a Mistral class ship would yield additional 400...500 kW of electric power and provide fuel saving nearly 100 liters per hour.

Conclusions

1. The scheme of heat exchange-type TEG utilizing as the source of heat the exhaust gases of marine propulsion plants is discussed.
2. It is shown that maximum power of individual module in the above scheme meets the condition $R_o/R_t = 1$, whereas total power of TEG can monotonically increase to the limit restricted to theoretical efficiency, i.e. defined only by thermoelectric material properties.
3. Technical and economic features of the above scheme permit to expect wide application of similar TEG on water transport.

References

1. L.I.Anatychuk, R.V.Kuz, Theory and Computer Simulation of Automotive Thermoelectric Generators, XIII Interstate Workshop “Thermoelectrics and their Applications”, November 13-14, 2012, A.F.Ioffe Physical and Technical Institute, Saint-Petersburg.

2. L.I.Anatychuk, O.J.Luste, and R.V.Kuz, Theoretical and Experimental Studies of Thermoelectric Generator for Vehicles, J. Electronic Materials 40(5), (2011).
3. J.W.Fairbanks, Thermoelectric Developments for Vehicular Applications, Diesel Engine Efficiency and Emission Research Conference, Detroit, August 24, 2006.
4. Sumeet Kumar, Stephen D. Heister, Xianfan Xu, James R. Salvador and Gregory P. Meisner, Thermoelectric Generators for Automotive Waste Heat Recovery Systems. Part I: Numerical Modeling and Baseline Model Analysis, J.Electronic Materials**,** DOI: 10.1007/s11664-013-2471-9 (2013)
5. Jorge Martins, Francisco P. Brito, L.M. Goncalves, and Joaquim Antunes, Thermoelectric Exhaust Energy Recovery with Temperature Control through Heat Pipes, Universidade do Minho, Portugal, 2011-01-315
6. Aleksander Kushch, Madhav Karri, Brian Helenbrook, and Clayton J. Richter, The Effects of an Exhaust Thermoelectric Generator of a GM Sierra Pickup Truck, 2004 DEER Conference. August 29-September 2, 2004, Coronado, California.
7. Travis T. Wallace, Development of Marine Thermoelectric Heat recovery Systems, 2011 DOE Thermoelectric Applications Workshop, January 5, 2011.
8. http://www.alphabetenergy.com/product/e1/
9. Yu.M.Lobunets, Thermoelectric Generator, Patent of Ukraine №8357 of 27.08.2013.
10. Yu.M.Lobunets, Criteria for Performance Evaluation of Thermoelectric Power Converters, J.Thermoelectricity **2**, 68 – 84 (2014).

Submitted 20.11.2014.

V.Ya.Mikhailovsky, R.V.Kuz, V.V.Lysko,
M.V.Maksimuk, R.M.Mochernyuk

Institute of Thermoelectricity NAS and MES of Ukraine
1, Nauky Str., Chernivtsi, 58029, Ukraine

THERMOELECTRIC GENERATOR MODULES OF *n-InSe* AND *p-PbTe*-BASED MATERIALS FOR THE LEVEL OF OPERATING TEMPERATURES 30-500ºC

This paper gives the results of computer and experimental studies of thermocouple generator modules of InSe and PbTe-based materials to be used in thermoelectric power converters for the hot temperature level ~ 500°C. Computer methods based on optimal control theory are used to determine optimal conditions whereby maximum power and efficiency of InSe and PbTe is achieved. Design is performed with regard to temperature dependences of material parameters, thermal and electric losses on the contacts and module interconnects.

Key words: computer design, generator modules, efficiency, termoelement.

Introduction

To create one-segment generator modules for the hot temperature level 500 °C, *n-PbTe* and *p-GeTe-AgSbTe* (TAGS)-based materials are traditionally used [1, 2]. Maximum efficiency of such modules lies within 8-8.5 % [3]. However, the restricting factor for their mass use is high cost of TAGS source components [4]. In this connection, studies aimed at creating thermoelectric modules of other materials become of current concern [5-8].

Among the alternative thermoelectric materials for operation in medium-temperature range, *InSe*-based materials attract the attention of researchers owing to their low thermal conductivity, high Seebeck coefficient [9]. Besides the cost of indium and selenium about 3-4 times is lower than the cost TAGS components: germanium, tellurium, silver and antimony [10]. However, in the majority of cases, *InSe* is employed as thin films for the manufacture of photoelectric devices. The results of development and creation of thermoelements based on the bulk InSe materials have not been recorded.

The purpose of this work is computer design and creation of thermoelectric modules of *n-InSe–p-PbTe*-based materials and experimental study of their characteristics.

Physical model of thermoelectric generator module and its description

Thermoelectric generator module consists of a number of equal pairs of thermoelectric legs that are electrically connected in series and thermally in parallel. With regard to that, for the design of thermoelectric generator module this paper deals with one structural unit of module, namely thermoelement. The thermoelement model is given in Fig. 1. It comprises *n*- and *p*-type legs (1), connecting copper plates (2) and isolating ceramic plates (3). The model takes into account contact layer (4) between the legs and connecting plates. The hot and cold thermoelement surfaces are at constant temperatures T_{hot} and T_{cold}, respectively.

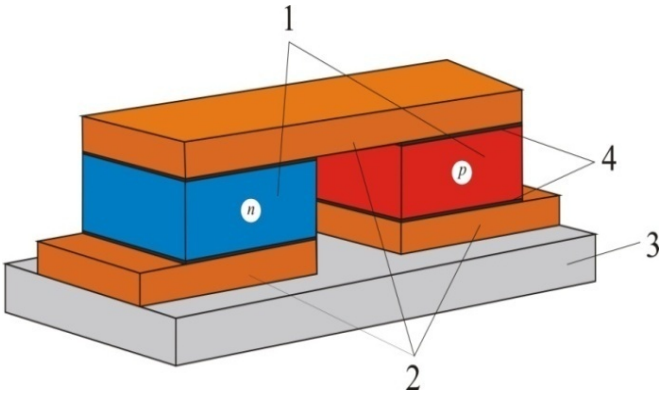

Fig. 1. Thermoelement model.
1 – thermoelement legs, 2 – connecting plates,
3 – ceramics, 4 –contact layers.

Parameters of thermoelectric materials, electric interconnects and connecting plates are a function of temperature. $\alpha_n(T)$, $\alpha_p(T)$ are the Seebeck coefficients of materials of *p*- and *n*-type legs. $\sigma_n(T)$, $\sigma_p(T)$ is the electric conductivity of leg materials; $\kappa_n(T)$, $\kappa_p(T)$ is the thermal conductivity of leg materials; $\sigma_{con}(T)$, $\kappa_{con}(T)$ is the electric conductivity and thermal conductivity of interconnect material; $\kappa_{ins}(T)$ is the thermal conductivity of ceramic plate.

The contacts of thermoelectric legs with connecting plates are characterized by the value of contact electric resistance $r_c(T)$ which is also a function of temperature. The space between the legs is filled with air of thermal conductivity κ_{air}. In this air space, heat exchange between the hot and cold ceramic plates takes place.

Maximum efficiency of thermoelectric module is described by the following expression:

$$\eta = \frac{Q_h - Q_c}{Q_h} = 1 - \varphi, \tag{1}$$

where Q_c, Q_h are external heat fluxes on the cold and hot surfaces of generator module, respectively. Function $\varphi = \frac{Q_c}{Q_h}$ can be regarded as a minimizing functional of the assigned task. Then it is necessary to pass to equivalent logarithmic functional $J = \ln\varphi$:

$$J = \ln q_c - \ln q_h, \tag{2}$$

where

$$q_c = \frac{Q_c}{nI}, \quad q_h = \frac{Q_h}{nI}, \tag{3}$$

q_c, q_h are specific heat fluxes on the cold and hot thermoelement junctions, respectively.

To calculate the boundary heat fluxes q_c and q_h, use is made of a system of four differential equations of nonequilibrium thermodynamics

$$\left.\begin{aligned} \frac{dT(x)}{dx} &= -\frac{\alpha(T)j}{\kappa(T)}T(x) - \frac{j}{\kappa(T)}q(x) \\ \frac{dq(x)}{dx} &= \frac{\alpha(T)^2 j}{\kappa(T)}T(x) + \frac{\alpha(T)j}{\kappa(T)}q(x) + \frac{j}{\sigma(T)} \end{aligned}\right\}_{n,p}, \tag{4}$$

where x is dimensionless coordinate, $0 \le x \le 1$, $j_{n,p} = \dfrac{Il}{s_{n,p}}$ is specific current density in thermoelement legs. The boundary conditions for system (4) are of the form:

$$T(0) = T_{cold} + \delta T_c, \quad T(1) = T_{hot} - \delta T_h, \tag{5}$$

where the losses in temperature difference on the ceramic and connecting plates δT_c and δT_h are defined in [11] with regard to the difference in parameters of ceramic and interconnect materials on the cold and hot sides:

$$\left.\begin{aligned} \delta T_c &= -\frac{q_c}{l\left(\frac{1}{j^n}+\frac{1}{j^p}\right)}\left(\frac{d_{ins}}{\kappa_{ins}(T_{cold})K_{ins}}+\frac{d_{con}}{\kappa_{con}(T_{cold})K_{con}}\right), \\ \delta T_h &= -\frac{q_h}{l\left(\frac{1}{j^n}+\frac{1}{j^p}\right)}\left(\frac{d_{ins}}{\kappa_{ins}(T_{hot})K_{ins}}+\frac{d_{con}}{\kappa_{con}(T_{hot})K_{con}}\right). \end{aligned}\right\}, \tag{6}$$

where K_{ins}, K_{con} are fill factors of ceramic and connecting plates.

The expressions for heat fluxes q_h and q_c with regard to temperature dependence of electric contact resistance will take on the form:

$$\left.\begin{aligned} q_h &= \sum_{n,p}\left[q^{n,p}(1)+\frac{j^{n,p}}{l}r_c(T_{hot})\right]+q^h_{con}, \\ q_c &= \sum_{n,p}\left[q^{n,p}(0)+\frac{j^{n,p}}{l}r_c(T_{cold})\right]-q^c_{con}. \end{aligned}\right\}, \tag{7}$$

where in order to find the specific Joule heat $q^{h,c}_{con}$ released in connecting plate, expression [12] is used:

$$q^h_{con} = \frac{2I^2 r_c(T_{hot})}{d_{con}}\left(K_{con}-\frac{2}{3}\right),\ q^c_{con} = \frac{2I^2 r_c(T_{cold})}{d_{con}}\left(K_{con}-\frac{2}{3}\right). \tag{8}$$

Heat fluxes q_h and q_c depend on specific current density $j_{n,p}$. The challenge is to determine the values of the current density $j_{n,p}$, which provide for a minimum of functional *J*. Herewith thermoelement efficiency reaches its highest value.

Optimal control theory [13, 14] gives a solution of the assigned task. It is realized by a numerical method of successive approximations and allows finding the optimal density of generated current to assure maximum efficiency of thermoelectric power converter. Through selection of the geometrical dimensions and the number of thermoelements one can achieve the assigned voltage and power of thermoelectric generator module. The complexity of the optimization problem enables its solving by computer methods.

Results of designing modules of *InSe – PbTe* based materials

In_4Se_3 based modules

Computer design and optimization of *InSe–PbTe* thermoelectric modules was performed with regard to the temperature dependences of thermoelectric materials obtained through synthesis of the

source components and hot pressing of synthesized materials for the range of hot side temperatures 450-500°C, cold side temperatures 30-90 °C.

As a *p*-type thermoelement leg, sodium-dope *PbTe*-based material was selected, as long as in the temperature range 400-500°C the figure of merit of *PbTe* is rather high (Fig.2). It should be noted that selection of *PbTe* is also motivated by the well-proven technique of samples production. However, this does not rule out the possibility of using in thermoelement of other *p*-type medium-temperature materials.

Experimental temperature dependences of thermoelectric parameters of *InSe* and *PbTe* based materials (Fig.2-5) were obtained on automated equipment Altec-10001 developed by the Institute of Thermoelectricity [15].

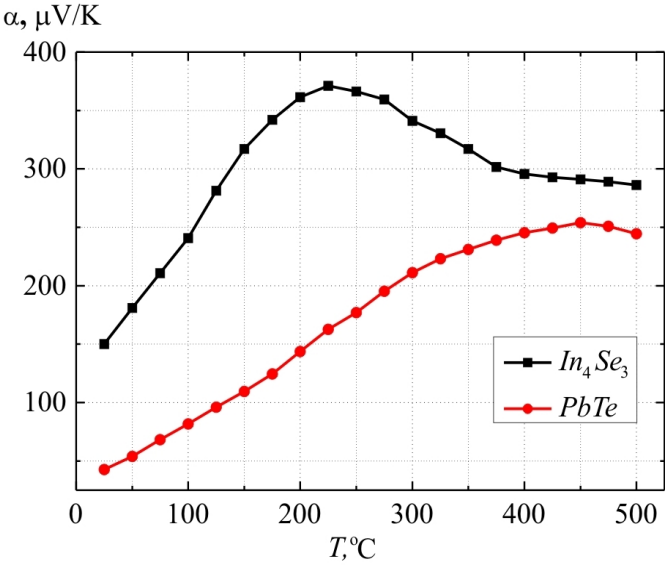

Fig.2.The figure of merit of n-$In_4Se_3$and p-PbTe versus temperature.

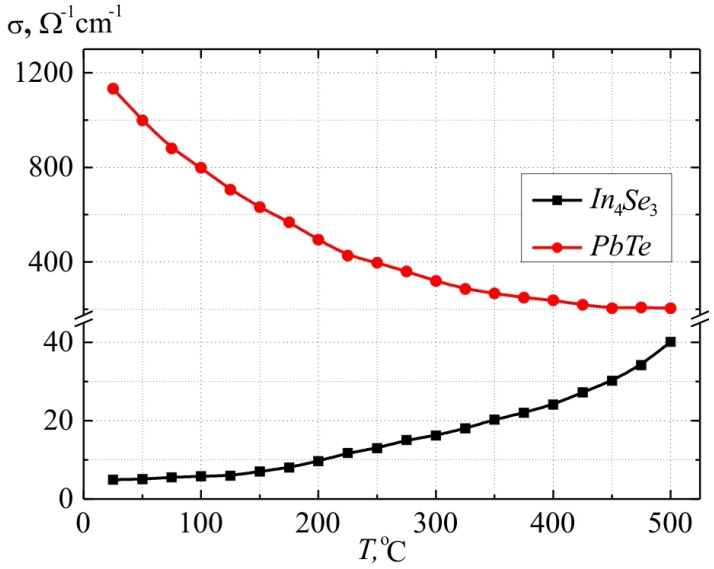

Fig. 3. The electric conductivity of n-In_4Se_3 and p-PbTe versus temperature.

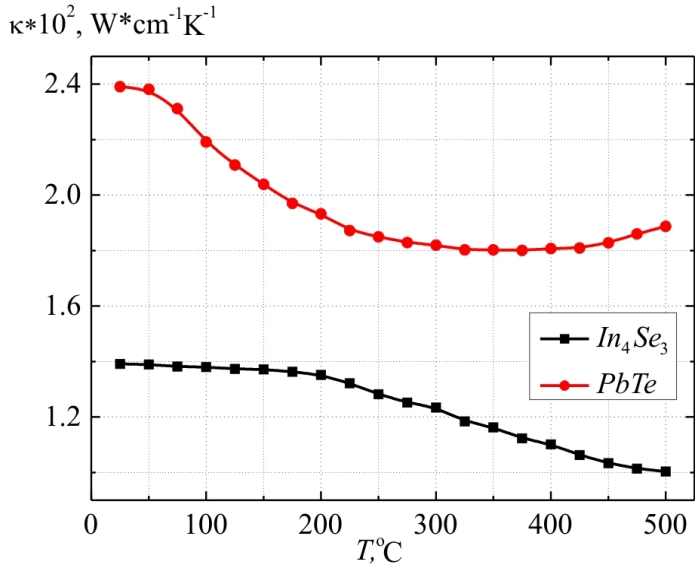

Fig. 4. The thermal conductivity of n-In_4Se_3 and p-PbTe versus temperature.

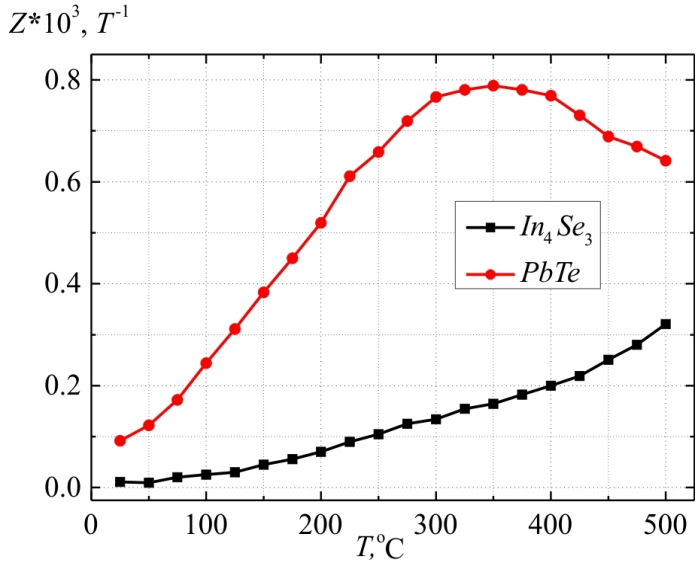

Fig.5. The Seebeck coefficient of n-In_4Se_3 and p-PbTe versus temperature.

As is evident from Fig.5, the value of α for In_4Se_3 is rather high and, with a rise in temperature, it passes through the maximum (370 μV/K) at 225-250 ºC. At the operating temperatures of the module 400-500 ºC, the value of α for In_4Se_3 varies only slightly and is on the level of 300 μV/K. The electric conductivity of n-In_4Se_3 at 20 ºC is very low, increases with a rise in temperature and at 500ºC reaches 40 $\Omega^{-1}cm^{-1}$. The thermal conductivity of *n-In_4Se_3*, on the contrary, is reduced with a rise in temperature and at 500 ºC is 1.0 W/cm K. The calculated thermoelectric figure of merit of *n-In_4Se_3* at 500 ºC is $0.35 \cdot 10^{-3}$ K^{-1}.

The Seebeck coefficient for *p-PbTe* is also rather high and at 400-500ºC lies within 250-260 μV/K. The electric conductivity of *p-PbTe* at these temperatures is 200-220 $\Omega^{-1}cm^{-1}$. The thermal conductivity passes through the minimum and at 500 ºC reaches the value of 1.9 W/cm·K.

The electric power of modules made of the above described materials (*p-PbTe*, *n-In_4Se_3*) versus the cross-sectional area of legs for different values of output voltage is represented in Fig.6.

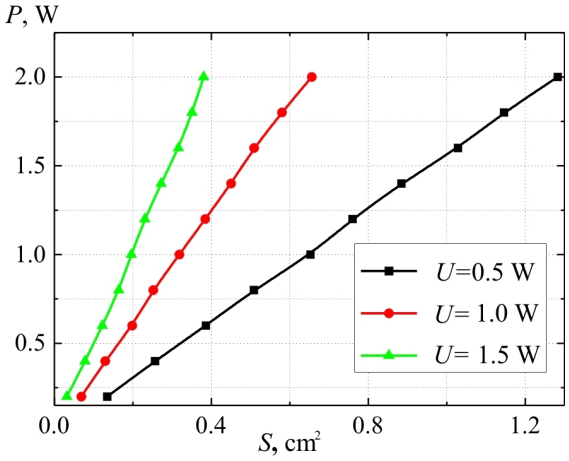

Fig.6. The electric power of In_4Se_3–PbTe module versus the cross-sectional area of legs for different values of output voltage, T_h=500°C, T_c=30 °C, h=5.5 mm.

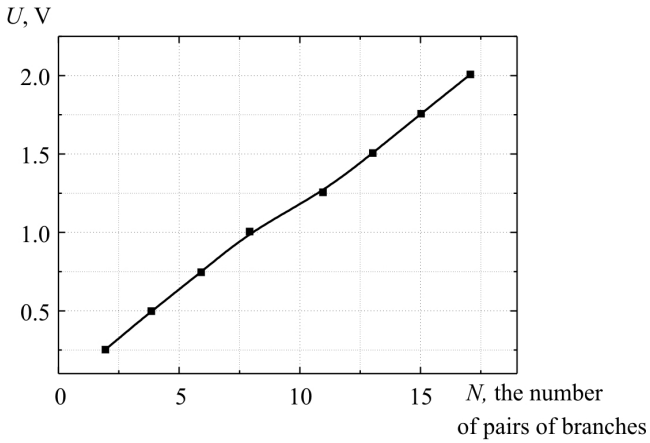

Fig.7. The output voltage of In_4Se_3–PbTe module versus the number of legs in a module, T_h=500 °C, T_c=30 °C, h=5.5 mm.

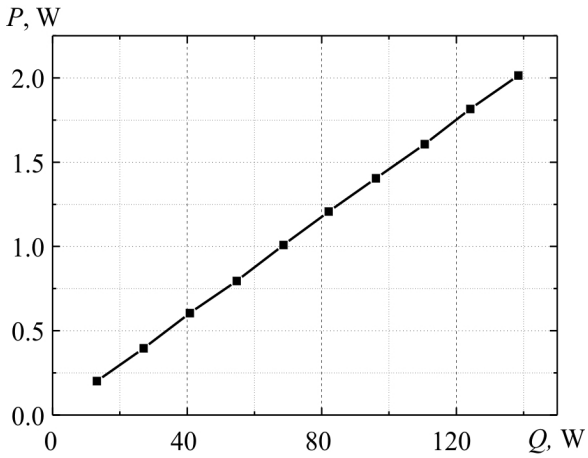

Fig.8. The optimal heat flux (Q) for obtaining given electric power (P) of In_4Se_3–PbTe module, T_h=500 °C, T_c=30 °C, h=5.5 mm

At module power 1 W and module voltages 0.5 V; 1.0 V; 1.5 V the cross-sectional area of leg is 68, 30 and 18 mm^2, respectively (Fig. 6). In so doing, to the get the voltage of 1 V in the assigned range of cold and hot temperatures, it is necessary to have 8 thermoelements (Fig. 7). Accordingly, for 2 V it is necessary to have 16 thermoelements, etc. The values of heat fluxes needed to obtain the assigned electric powers are given in Fig. 8. It is seen that to generate 1 W of electric power, the heat flux on the hot side of a module must come up to 65-70 W.

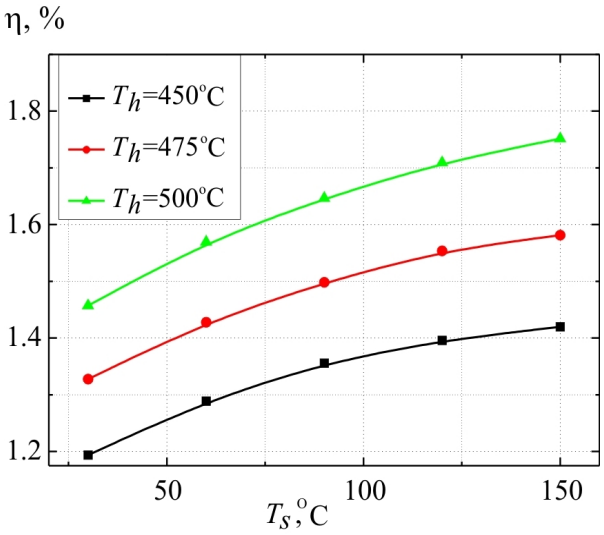

Fig.9. The efficiency of In_4Se_3–PbTe module versus the cold side temperature at different hot side temperatures of module.

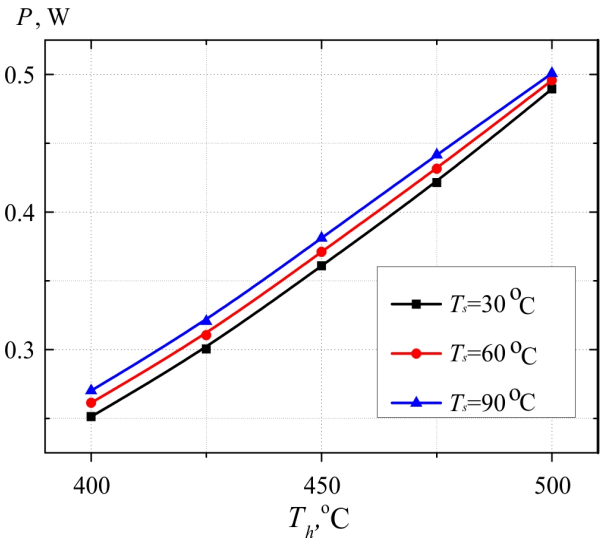

Fig.10. The electric power of In_4Se_3–PbTe module versus the hot side temperature.

A non-traditional dependence was obtained when studying the effect of cold side temperature on module efficiency. As is seen from Fig.9, with a rise in cold side temperature there is efficiency increase. In so doing, the electric power of a module, especially at high temperatures (~500 °C), is very weakly dependent on the cold side temperature (Fig. 10).

Such dependence is due to the fact that at low cold side temperatures of a module there is a mismatch between thermoelectric parameters α, σ, κ of In_4Se_3 and *PbTe* samples. Therefore, thermoelectric material on the cold side of a module works under conditions far from being optimal.

With a rise in temperature of In_4Se_3 samples, the thermal conductivity is essentially reduced and the electric conductivity is increased by about an order (Fig.3, 4), assuring higher Z value at elevated cold side temperatures of a module. The dependence passes through the maximum, and further increase of the cold side temperature (in this case over 160 °C) reduces the efficiency.

Modules designed using other compounds based on *InSe*

As is clear from the investigation results, the efficiency of a module of *InSe-PbTe*-based materials (Fig.2-5) is rather low as compared to other modules traditionally used in medium-temperature range [16]. One of the ways to enhance the efficiency of such module is to improve the thermoelectric figure of merit of In_4Se_3 via optimization of composition and the use of efficient doping impurities. In particular, in [17] it is shown that for $In_4Se_{2.35}$ single crystal grown by the Bridgman method maximum ZT value is 1.48 at 432 °C. In [18], through doping with Cl the figure of merit was increased to 1.53, in [19], by introducing Pb and Sn – to 1.4 at 427°C. Using the thermoelectric parameters of In_4Se_3 compounds given in [17 – 19] (Fig. 11) as the initial data, the authors of this paper used optimal control method to calculate the efficiency of modules (Fig. 12), where *PbTe* is *p*-leg, $In_4Se_{2.35}$, $In_4Se_{2.67}Cl_{0.03}$ and $In_4Pb_{0.01}Sn_{0.04}Se_3$ are *n*-leg.

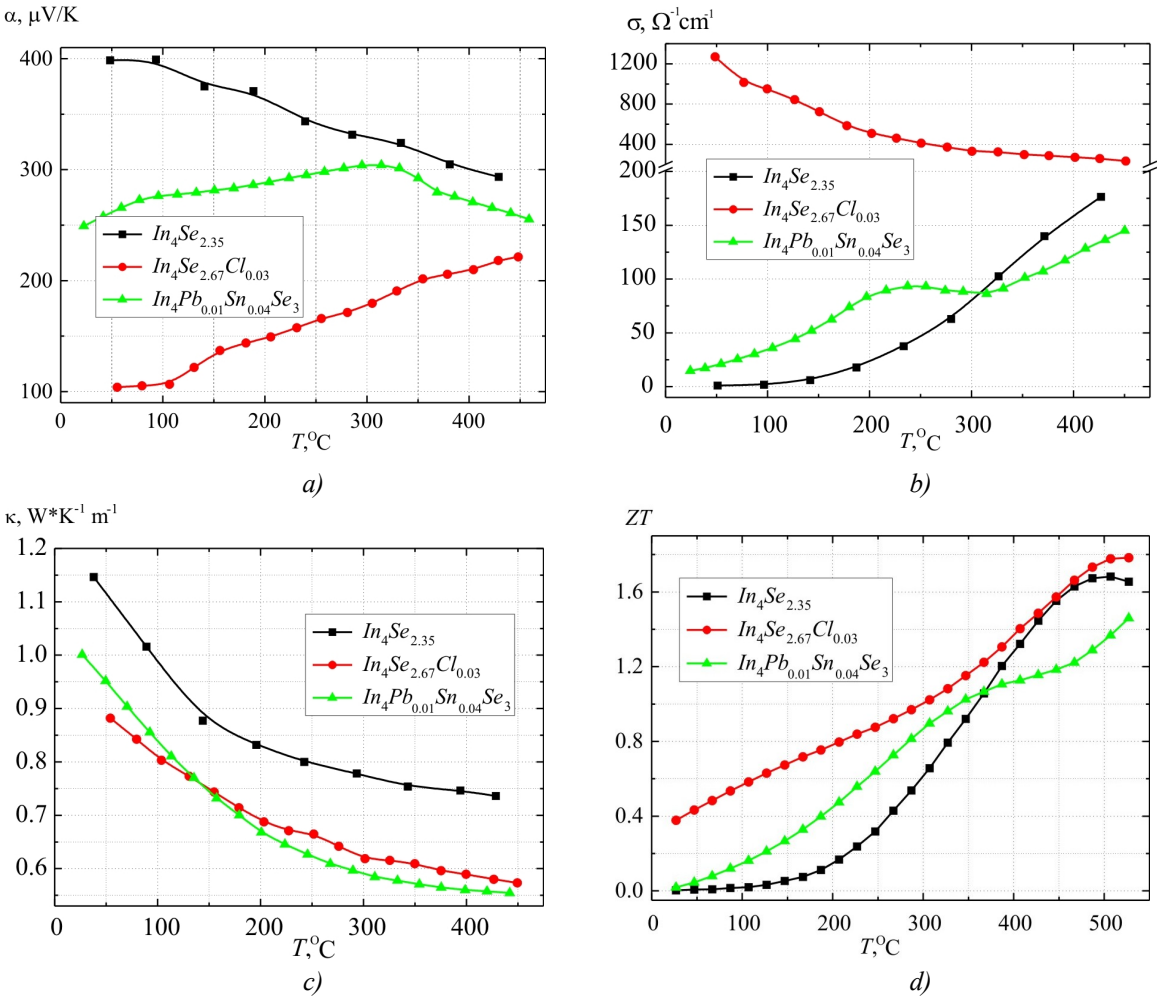

Fig. 11. Temperature dependences of the Seebeck coefficient (a), electric conductivity (b), thermal conductivity (c) and figure of merit (d) of In_4Se_3 materials [18 – 20].

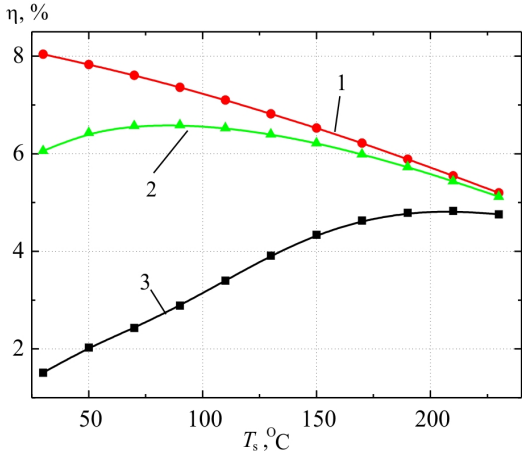

Fig. 12. The efficiency of thermoelectric modules of materials:
1 – p-PbTe – n-$In_4Se_{2.67}Cl_{0.03}$, 2 – p-PbTe – n-$In_4Se_{2.32}I_{0.03}$, 3 – p-PbTe – n-$In_4Se_{2.35}$
versus the cold side temperature. The hot side temperature is 500 °C.

Maximum efficiency η=8 % at constant hot side temperature and variable cold side temperatures was demonstrated by a module with *p-PbTe* and *n-*$In_4Se_{2.67}Cl_{0.03}$ (Fig. 12). For a module where *Pb* and *Sn*-doped In_4Se_3 is used as *n*-leg, efficiency maximum is shifted towards higher temperatures and makes ~6.6% at T_c= 90 °C. This is due to a mismatch in thermoelectric parameters (mostly σ) of *PbTe* and $In_4Pb_{0.01}Sn_{0.04}Se_3$ materials (Fig. 11 b). Further reduction of η to 5.1% is caused by the reduction of operating temperature difference, even though the figure of merit of $In_4Pb_{0.01}Sn_{0.04}Se_3$ is increasing (Fig. 11 d).

A non-traditional dependence was obtained when studying the efficiency of a module with *p-PbTe* and *n-*$In_4Se_{2.35}$ versus the cold side temperature (Fig. 12). A rise in T_c leads to efficiency increase that reaches its maximum 4.83% at 210 °C. Such dependence of η is due to non-optimal material operating conditions on the cold side and low figure of merit values of $In_4Se_{2.35}$ material in low temperature region (Fig.11 d).

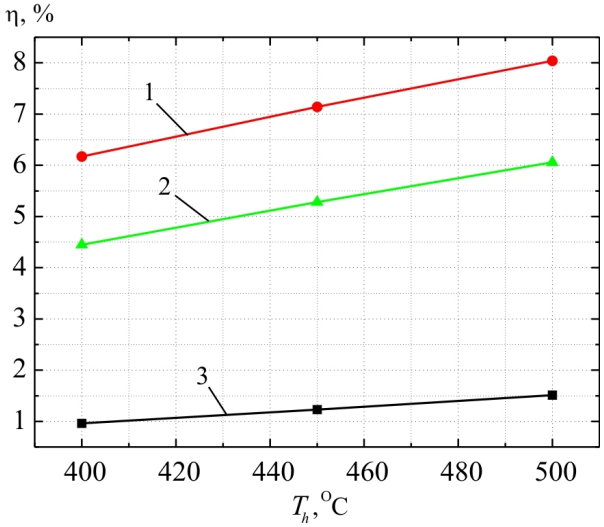

Fig. 13. The efficiency of thermoelectric modules of materials: 1 – p-PbTe – n-$In_4Se_{2.67}Cl_{0.03}$,
2 – p-PbTe – n-$In_4Se_{2.32}I_{0.03}$, 3 – p-PbTe – n-$In_4Se_{2.35}$
versus the hot side temperature. The cold side temperature is 30 °C

Fig. 13 shows the efficiency of thermoelectric modules based on *PbTe* and *InSe* compounds versus the hot side temperature.

It is clear that with a rise in the hot side temperature, the efficiency of a module is increased and reaches the level of 8% and 6% for *PbTe-*$In_4Se_{2.67}Cl_{0.03}$ and *PbTe-* $In_4Pb_{0.01}Sn_{0.04}Se_3$, respectively. At the cold side temperature 30 ^oC maximum efficiency for *p-PbTe – n-*$In_4Se_{2,35}$ module is 1.5%, making inefficient the use of this material in pair with *p-PbTe* in traditional generator modules.

The results of experimental studies In_4Se_3 – *PbTe* based modules

On the basis of calculations performed, some alternate designs of thermoelectric modules of *p- PbTe* and *n-* In_4Se_3 materials of electric power 0.5-5 W were developed (Table 1).

Electric interconnect of *PbTe* and In_4Se_3 legs was made by silver plates via diffusion bonding technique. *Co* and *Fe* are used as anti-diffusion layers for *PbTe* and In_4Se_3. As transient layers, a mixture of *CoTe* and *PbTe* is used for *PbTe*, and a mixture of *CoTe* and In_4Se_3 - for In_4Se_3 [20].

Table 1

Geometric and electric parameters of PbTe - In_4Se_3*-based modules with a series connection of legs (T_h = 500 ^oC, T_c = 30 ^oC)*

Electric power, W	Electric voltage, V	Heat flux, W	Leg cross-section, mm^2	Number of leg pairs	Overall dimensions, mm
0.5	0.5	34.2	5.6×5.6	4	11.7×19.7×7.8
	1.0		4×4	8	17.5×25.5×7.8
	5.6		1.5×1.5	50	19.5×27.5×7.8
	3.2		1.6×1.6	28	14.2×23.3×6.3
3	0.5	205.4	13.8×13.8	4	28.1×36.1×7.8
	1		9.8×9.8	8	40.7×48.7×7.8
	8.8		3.1×3.1	78	46.3×50.7×7.8
	1		7.2×7.2	8	30.3×38.3×6.3
	5.6		2.9×2.9	50	33.5×41.5×6.3
5	3.2	342.4	6.7×6.7	28	49.9×65.1×7.8
	5.6		3.7×3.7	50	41.5×49.5×6.3

For 0.5 W modules the number of legs was increased from 4 to 50, and the cross-section of leg in this case was reduced from 5.6×5.6 mm to 1.5×1.5 mm, respectively. The overall dimensions of a module were in the range from 11.7×19.7 to 14.2×23.3 mm. For 5 W modules the cross-section of legs

should be increased with their invariable height. Maximum dimensions of a 5 W module of voltage 5.6 V were 50×65×7.8 mm.

Using of cheap thermoelectric materials and simple technology makes the prospect of wide use of *InSe-PbTe* based modules for thermoelectric energy converters on the level of operating temperatures 30-500°C.

Conclusions

1. Using the methods of optimal control theory, computer design has been performed and the efficiency of generator modules of *n-InSe–p-PbTe*-based materials in the temperature range of 30–500 °C has been determined. It has been shown that maximum efficiency of thermoelectric modules is 8% for *p-PbTe–n-*$In_4Se_{2.67}Cl_{0.03}$ and 6.6% for *p-PbTe–n-*$In_4Pb_{0.01}Sn_{0.04}Se_3$.
2. For the first time thermoelectric generator module based on *n-*In_4Se_3*–p-PbTe* has been created for the operating temperature range 30-500 °C, and the results of theoretical calculations have been experimentally confirmed.
3. Thermoelectric modules of materials based on *n-InSe–p-PbTe* and *n-PbTe* and *p-GeTe-AgSbTe* are characterized by close efficiency values. However, *n-InSe–p-PbTe* modules have lower manufacturing cost which gives them the advantage for use in medium-temperature range.

References

1. Z.H. Dughaish. Lead telluride as a thermoelectric material for thermoelectric power generation // Physica B, 322, pp. 205-223 (2002).
2. E.A. Skrabek, D.S. Trimmer. Properties of the general TAGS system. // in CRC Handbook of Thermoelectrics, Eds. D.M. Rowe, pp.267-275, CRC Press, Boca Raton, FL (1995).
3. L.T.Strutynska, V.R.Bilinsky-Slotylo, and V.Ya.Mikhalovsky, Design of Segmented Modules Based on PbTe/TAGS for Thermoelectric Generators, *Physics and Chemistry of the Solid State.* – 2012.- № 4.- T13.-C. 1032-1036..
4. Mineral commodity summaries 2012 / U.S. Geological Survey. Reston: Virginia, 2012. 198 p.
5. Singh D.J. Electronic Transport in Old and New Thermoelectric Materials / D.J. Singh // Science of Advanced Materials. Vol.3. 2011. P.561-570.
6. High-performance nanostructured thermoelectric materials / J.-F. Li, W.-Sh. Liu [etc] // NPG Asia Mater. Vol.2, No.4. 2010. P.152-158.
7. Tritt T.M. Thermoelectric Phenomena, Materials, and Applications / T.M. Tritt // Annual Review of Materials Research. Vol.41. 2011. P.433-448.
8. Snyder G.J. Complex thermoelectric materials / G.J. Snyder, E.s. Toberer // Nature Materials. Vol.7. 2008. P.105-114.
9. Ju-Hyuk Yim et al. / Thermoelectric properties of indium-selenium nanocomposites prepared by mechanical alloying and spark plasma sintering // Journal of Electronic Materials.-2012.-Vol. 41.-№ 6.- P.1354-1359.
10. http://www.infogeo.ru/metalls/worldprice/.
11. L.I.Anatychuk, L.N.Vikhor, Computer Design of Staged Generator Modules, *J.Thermoelectricity*. – 2002. – №4. – C. 19 – 27.
12. L.I.Anatychuk, V.A.Semenyuk, *Optimal Control Over the Properties of Thermoelectric Materials and Devices* (Chernivtsi:Prut, 1992), 264 p.
13. L.N.Vikhor, Computer Design of Thermoelectric Generator Modules, *J.Thermoelectricity*. – 2005.

– №2. – P. 60-67.

14. L.I.Anatychuk, *Thermoelements and Thermoelectric Devices. Handbook* (Kyiv: Naukova Dumka, 1979), 766 p.
15. L.I.Anatychuk, M.V.Havrylyuk, and V.V.Lysko, Installation for Measuring the Properties of Semiconductor Thermoelectric Material, *J.Thermoelectricity*. – 2010, №3. P. 41-49.
16. L.M.Vikhor, V.Ya.Mikhailovsky, and R.M.Mochernyuk, Materials Optimization and Performance Evaluation of Generator Modules for Heat Recuperators, *Physics and Chemistry of the Solid State* 1(15), 206-213 (2014).
17. J.-S.Rhyee, K.H.Lee, S.M.Lee, E.Cho, S.I.Kim, E.Lee, Y.S. Kwon, J.H.Shim, G.Kotliar. Peierls distortion as a route to high thermoelectric performance in $In_4Se_{3-\delta}$ crystals.– Nature2009, 459, 965.
18. J.-S.Rhyee, K.Ahn, K.H.Lee, H.S.Ji, J.-H.Shim. Enhancement of the thermoelectric figure-of-merit in a wide temperature range in $In_4Se_{3-x}Cl_{0.03}$ bulkcrystals. –Adv. Mater. 2011, 23, 2191.
19. Z.-S.Lin, L.Chen, L.-M.Wang, J.-T.Zhao, L.-M.Wu. A promising mid-temperature thermoelectric material candidate: *Pb/Sn*-codoped $In_4Pb_xSn_ySe_3$. – Adv. Mater. 2013, 25, 4800.
20. Patent (UA) № 79960 InCl H01L 35/00 Method for Manufacture of Thermoelement Comprising *n*-In_4Se_3 / V.Ya.Mikhailovsky, R.M.Mochernyuk, Kim Sang Il, Lee Kyuhyoung – Publ. 13.05.2013, Bul.№9 Appl.u2012 12353 of 29.10.12.

Submitted 19.12.2014.

L.I. Anatychuk

L.I. Anatychuk, R.V. Kuz

Institute of Thermoelectricity NAS and MES of Ukraine
1, Nauky Str., Chernivtsi, 58029, Ukraine

R.V. Kuz

EFFECT OF AIR COOLING ON THE EFFICIENCY OF SECTIONAL THERMOELECTRIC GENERATOR IN A CAR WITH A PETROL ENGINE

The paper is concerned with a physical model of sectional thermoelectric generator (TEG) for a petrol engine with a system of heat removal from TEG comprising an air-to-liquid heat exchanger and an electric fan. Computer simulation of TEG operation for a 70 kW petrol engine is performed. The optimal hot temperatures of the generator sections and the optimal fan powers whereby maximum real TEG efficiency is attained with regard to the costs of power supply to the fan for ambient temperatures in the range of –40…+50°C are found. A comparison of sectional generator efficiency to the previously obtained values for one-section TEG is made. It is shown that a real efficiency of sectional TEG with a heat removal system is 1.2 – 1.4 times higher than that of one-section TEG. It is shown that the costs of power supply to heat removal system can reach 20…30% of TEG power.

Keywords: heat recovery, thermoelectric generator, internal combustion engines.

Introduction

The interest in using thermoelectric generators (TEG) for the recovery of exhaust heat of internal combustions engines remains unchanged. Analysis of international thermoelectric conference proceedings shows that the number of papers dealing with automotive applications of thermoelectricity is constantly growing [1] with creation of special sessions covering this subject [2]. This clearly demonstrates the invariable urgency of this line. The purpose of using TEG in a car is fuel saving due to utilization of engine exhaust heat for electric energy generation.

The presence of thermoelectric generator in a car creates additional problems related to TEG operation. One of them is to assure efficient heat removal from thermoelectric generator. Optimization of the costs of heat removal from one-section thermoelectric generator for cars with different engine types was performed in [3, 4]. Optimization of three-section TEG with a heat removal system for diesel engine was done in [5]. Investigations show that the costs of heat removal from TEG can reach 15-25% of electric energy produced by TEG with the optimal design of heat removal system. Of current interest is further study with a view to establish similar laws for sectional TEG in petrol engines, because as far as is known [4, 5], the use of sectional TEG for petrol engines provides for higher efficiency of waste heat recovery.

The purpose of this work is to estimate the efficiency of using sectional TEG in a car with petrol engine with regard to the costs of energy for heat removal from TEG.

Physical model

The work of sectional thermoelectric generator as part of a car can be represented by a schematic

shown in Fig. 1. Exhaust gas of thermal power Q_{in} and temperature T_{in} from engine 1 comes to hot heat exchanger 3 of sectional thermoelectric generator 2. Pat of the heat from the hot heat exchanger is transferred to thermopiles 4 which convert it to electric energy. TEG produces total electric power W_{TEG} at efficiency η_{TEG}. Part of this electric power W_{cool} is spent on the work of cooling system 6 which removes thermal power Q_{TEG} from the cold heat exchanger 5. The temperature of the cold heat exchanger is considered to be fixed.

Such a physical model and its mathematical description are detailed in [5]. The distinctive feature of the model in the present paper is that the temperature of exhaust gases in petrol engines is higher (~800ºC). This necessitates the use in TEG sections of different thermoelectric materials optimized for the necessary temperature range.

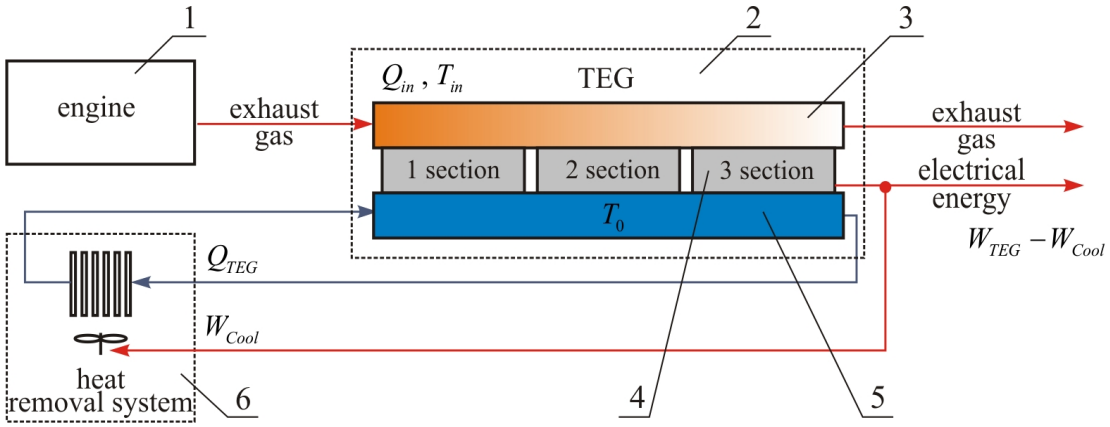

Fig. 1. A model of TEG operation in a car with regard to the costs of electric energy on heat removal from thermal generator. 1 – engine; 2 – sectional TEG; 3 – hot heat exchanger; 4 – thermopiles; 5 – cold heat exchanger, 6 – heat removal system.

As before, maximum efficiency of sectional thermoelectric generator was calculated according to method [5] by means of computer simulation [6] on a two-dimensional finite-element mesh. In short, it is as follows. At first, the hot temperatures of sections are optimized by varying thermal resistances of sections for achieving maximum TEG efficiency:

$$\eta_{TEG} = \frac{W_{TEG}}{Q_H^{in}}. \tag{1}$$

For the optimization of heat removal system a function of the efficiency of air-to-liquid heat exchanger is introduced as below

$$Q_{cool} = f(W_{cool}, T_L, T_A) \tag{2}$$

where Q_{cool} is thermal power of heat removal system, W_{cool} is electric supply power of heat removal system, T_L is liquid temperature, T_A is air temperature. This function is used for calculation of optimal supply power of heat removal system.

The effective efficiency of TEG is found from the expression:

$$\eta_{ef} = (W_{TEG} - W_{cool}) / Q_{in}. \tag{3}$$

Example of parameters calculation for TEG with cooling system

As an example, we shall perform optimization of sectional TEG with cooling system for a stock 70 kW petrol engine UMZ-3318 with the exhaust gas temperature ~790°C. For the calculation of the efficiency and power of such TEG the *n-PbTe* and *p-TAGS* thermoelectric materials were selected that are among the best in the figure of merit in the high-temperature range. Materials based on *Bi-Te* were selected for lower-temperature sections [7]. The *ZT* value of modules made of such materials is given in Fig. 2 [7].

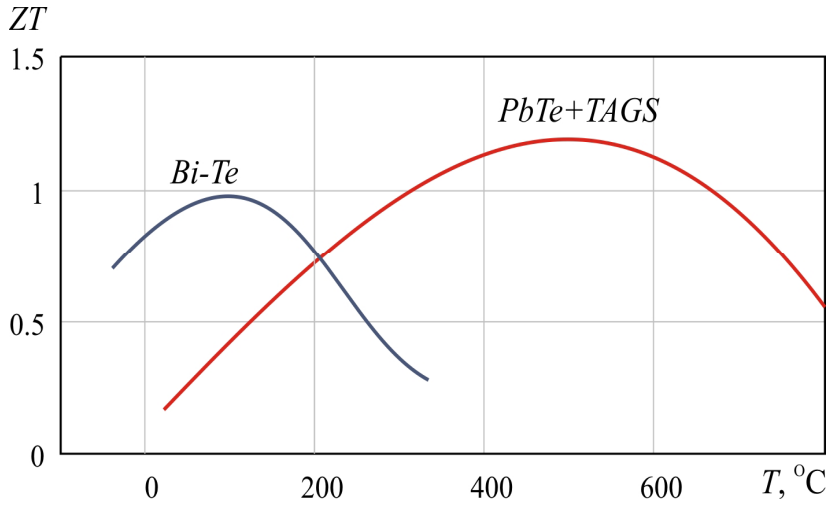

Fig. 2. Temperature dependence of ZT of modules made of materials based on Bi-Te and PbTe + TAGS.

TEG hot side temperature optimization. In the beginning, calculation and optimization of the hot temperatures of TEG sections took place according to procedure [5]. Fig. 3 shows an example of a two-dimensional temperature field in TEG sections calculated by computer simulation. Fig. 4 shows the values of the optimal hot temperatures of sections versus their cold temperature.

As is evident from Fig. 4, the optimal hot temperature of the third section does not rise above 280 ºC. Therefore, for this section it is more reasonable to use thermopiles of *Bi-Te* materials (Fig. 2). The temperatures of the first two sections are sufficiently high for using thermopiles of *n-PbTe* and *p-TAGS* materials in them. Further calculations will be performed for precisely this model.

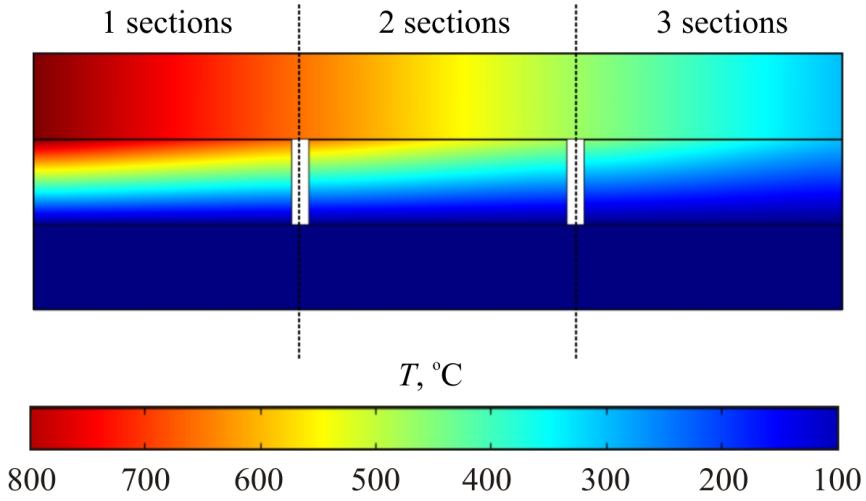

Fig. 3. Temperature distribution in TEG sections.

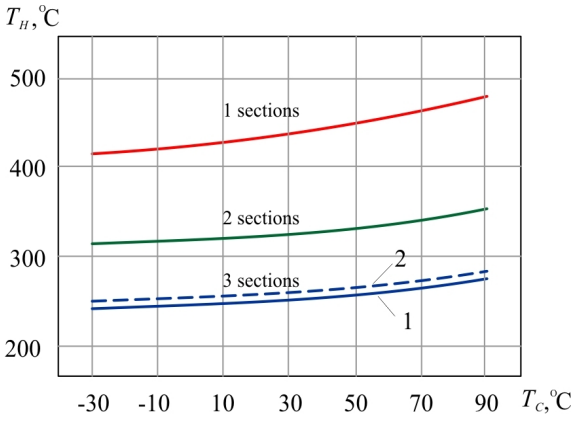

Fig. 4. The optimal hot temperature of TEG sections versus their cold temperature. 1 – for Bi-Te modules, 2 – for n-PbTe and p-TAGS modules.

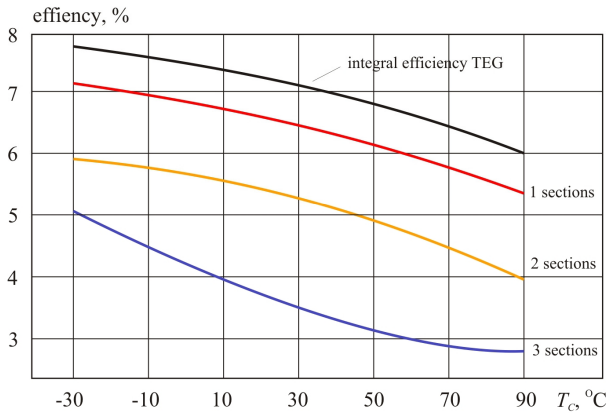

Fig. 5. The efficiency of sections and the integral TEG efficiency versus the cold side temperature of TEG.

Heat removal system optimization. The optimal costs of heat removal from the TEG sections were calculated according to procedure [3, 4]. Characteristics of air-to-liquid heat exchanger necessary for the calculations were taken from [3]. Fig. 6 gives the value of thermal power to be removed from TEG versus the cold temperature of TEG.

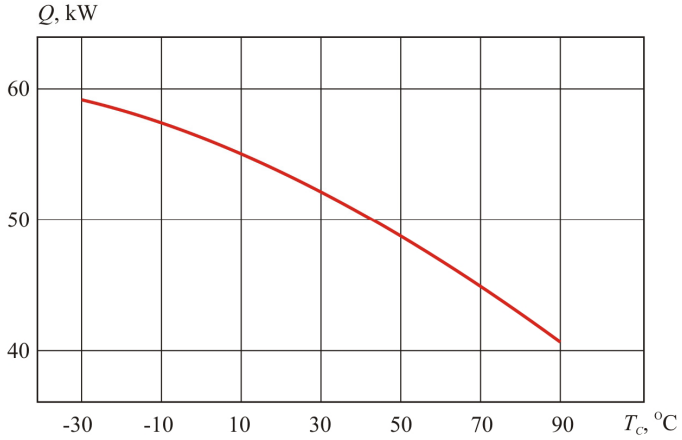

Fig. 6. Thermal power to be removed from TEG versus the cold temperature of TEG.

Fig. 7 shows the results of "TEG-cooling system" optimization for different ambient

temperatures. The optimal power values of cooling system fan are presented here. They make ~20%...30% of thermal generator power. Fig. 8 shows the electric power of TEG versus ambient temperature with regard to the costs of heat removal.

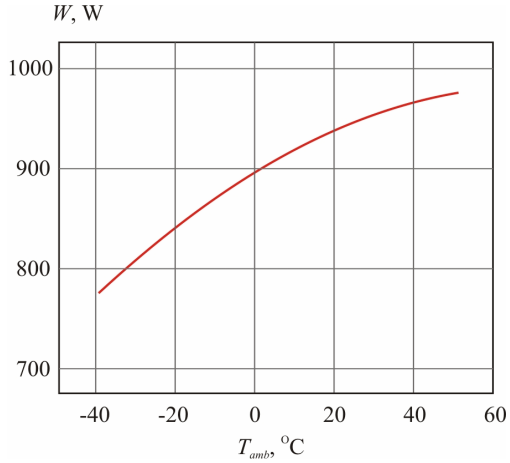

Fig. 7. The optimal electric power of TEG cooling system versus the ambient temperature.

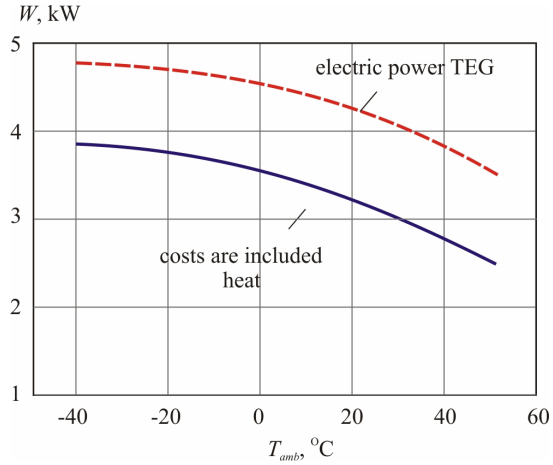

Fig. 8. The electric power of TEG versus the ambient temperature.

Fig. 9 compares the efficiency of one-section TEG [5] and three-section TEG analyzed in the present paper, as well as the efficiency of TEG for a diesel engine analyzed in [3, 5].

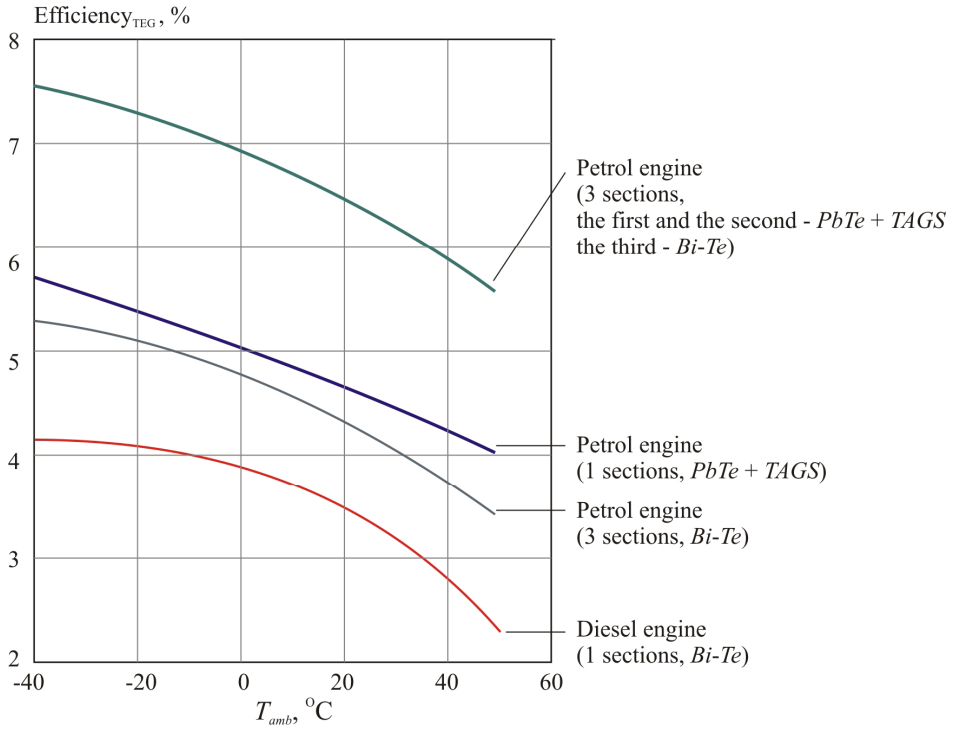

Fig. 9. TEG efficiency versus the ambient temperature.

It is seen that the use of generator sections, under otherwise equal conditions, yields better efficiency values. The use of sections assures 1.2 -1.3 times higher efficiency of TEG. As compared to TEG for a diesel engine, TEG for a petrol engine yields better figures both in efficiency and its stability versus the ambient temperature.

Conclusions

1. By means of computer simulation a physical model of three-section thermoelectric generator for a car with a petrol engine has been analyzed. Computer simulation efficiency has been demonstrated on a specific generator version for a car with a 70 kW petrol engine.
2. The optimal hot temperatures of sections have been obtained as a function of the cold side temperature of TEG in the range of –30…+90 ºC. It has been established that with a rise in the cold side temperature of TEG, the optimal hot temperatures are also displaced towards the range of higher values.
3. Optimization of heat removal system has been performed. The optimal costs of electric energy for heat removal have been found. It has been established that these costs increase from 770 W to 940 W with a rise in ambient temperature from –40 ºC to +50 ºC.
4. The power of TEG as a function of ambient temperature has been determined. It has been established that the highest power value (~4.7 kW) is achieved at $T_{amb} = -40$ ºC and reduced to 3.5 kW at $T_{amb} = +50$ ºC. Part of this energy is spent on assuring heat removal from TEG. With regard to these expenditures, the generator power at $T_{amb} = -40$ ºC is 3.8 kW and reduced to 2.6 kW at $T_{amb} = +50$ ºC.
5. A comparison of the efficiency of one-section and three-section generators demonstrates efficiency increase with the use of three sections from 5.8% to 7.5% at $T_{amb} = -40$ ºC. The efficiency of three-section generator remains higher at elevated ambient temperatures as well. At $T_{amb} = +50$ ºC the efficiency of three-section TEG is 5.63%, whereas the efficiency of one-section TEG is as low as 4%. In general, the investigations performed demonstrate the advantages of three-section TEG in electric power and efficiency by a factor of 1.2…1.4.
6. A system of heat removal from three-section TEG consumes a considerable amount of electric energy. These costs can make 20…30% of the total TEG power.
7. In the range of ambient temperatures –40…+60 ºC the efficiency of TEG for a petrol engine is reduced by ~14%. At the same time, the efficiency of TEG for a diesel engine is reduced by 45%. This testifies to the advisability of using TEG for diesel engines only at reduced ambient temperatures. Since the efficiency of TEG for a petrol engine is less dependent on the ambient temperature, it can be used in a wide range of above temperatures.

References

1. http://web.ornl.gov/sci/theory/ict2014/schedule.pdf.
2. http://ectmadrid2014.com/wp-content/uploads/EC2014_Schedule.pdf.
3. L.I.Anatychuk, R.V.Kuz, Effect of Air Cooling on the Efficiency of Thermoelectric Generator in a Diesel-Engined Car, *J.Thermoelectricity* **2**, 60-67 (2014).
4. L.I.Anatychuk, R.V.Kuz, Effect of Air Cooling on the Efficiency of Thermoelectric Generator in a Car with a Petrol Engine, *J.Thermoelectricity* **3**, 87-91 (2014).
5. L.I.Anatychuk, R.V.Kuz, Effect of Air Cooling on the Efficiency of Sectional Thermoelectric Generator in a Car with a Diesel Engine, *J.Thermoelectricity* **3**, 81-87 (2014).
6. Comsol Multiphysics – http://www.comsol.com.
7. L.I.Anatychuk, R.V.Kuz, Materials for Vehicular Thermoelectric Generators, *Proc. of ICT-2011, Michigan, USA*.

Submitted 17.10.2014.

R. Ahiska

Rasit Ahiska

Gazi University, Faculty of Sciences, Department
of Physics, 06500, Teknikokullar, Ankara, Turkey

TEGPAS A NEW APPARATUS FOR TEST OF THERMOELECTRIC GENERATORS

In this study, a new test measurement system and supervisory control and data acquisition application with programmable logic controller has been carried out to be enable the collection of the data of thermoelectric generator for the usage of thermoelectric modules as thermoelectric generator. A hot-cold water circulator system has been established to carry out thermoelectric generator experiments in the laboratory. During the production of the electric energy from the thermoelectric generator, the temperatures of the surfaces of the thermoelectric generator, current-voltage values obtained from output of the thermoelectric generator, hot and cold flows have been measured by the system instantly. All these data have been monitored continuously from the computer and recorded by a supervisory control and data acquisition program. At the same time, in the environments where there was no computer, an operator panel with the ability to communicate with the programmable logic controller has been used for the monitoring of the instant thermoelectric generator data. All of the measurement data of the thermoelectric generator have been aggregated in the new test measurement and supervisory control and data acquisition system. The setup test measurement system has been implemented on the thermoelectric generator system with about 10W.

Key words: thermoelectric generator, PLC, SCADA, test measurement

Introduction

Mankind's need for energy keeps increasing day by day. Due to the limited availability of fossil fuels such as petrol, coal used nowadays, people are increasing their efforts for the increase of renewable energy sources as well as more efficient usage of the energy resources [1]. When one considers the increase of human population in the world, the increase in the share of the new and renewable energy sources in energy production and efficient use of energy are inevitable. When one considers the greenhouse gas effect on the environment by fossil fuels, the importance of renewable and environmentally friendly energy resources becomes clearer [2]. Today, the studies of energy production from renewable energy sources such as wind, solar, biomass, hydro, geothermal and hydrogen continues rapidly. Thermoelectric generators (TEGs) are used to convert geothermal energy, which is one of the renewable energy sources available, into electrical energy [3]. The basic principle of the TEGs is the Seebeck effect, which was discovered in 1821 by Thomas Seebeck. Since TEGs have no moving mechanical parts, they are long-lived, silent, and environmentally friendly and they require little maintenance [4]. On the other hand, due to the low conversion efficiencies (about 5%), thermoelectric power applications are restricted [5]. Currently, many researches are focused on the increasing of the conversion efficiency of thermoelectric materials. One exception is the TE recovery

of waste heat in which it is unnecessary to consider the cost of the thermal input. Consequently, low conversion efficiency is not a serious drawback [6]. A thermoelectric module (TEM) consists of a number of thermoelements (from 3 to 127) connected electrically in series to increase the operating voltage and thermally in parallel to increase the thermal conductivity. TEGs convert thermal energy into electrical energy directly (Seebeck effect) [7].

Many different measurement instruments have been used for data acquisition and testing of the TEGs. Hand-held measuring instruments usually have been preferred to measure instantaneous values. Data acquisition cards have been used in order to transfer data obtained from the TEG experiments to a personal computer (PC). In order to register the data obtained from the TEGs in the PC, either a separate PC program is written or ready PC programs are often used. Gould et al. [8] designed a thermoelectric test system suitable for conducting experiments to measure the micro-electrical and power generation performance of thermoelectric modules. Their hardware consisted of standard PC running National Instruments LabView software, data acquisition (DAQ) PC card, Pico Technology thermocouple data logging unit, a number of T-type thermocouples. This system was tested for Melcor module CP1.4-127-05L TEG. Eklund et al. [9] used the DAQ board. Han et al. [10] stored the experimental data in a DAQ device (Yokogawa, DA100) for analysis, after reaching a steady state in the temperature and the voltage output in the TEG system. Kim [11] and Hasebe et al. [12] monitored temperatures of the heater, the heat sink base, and the ambient by utilizing T-type thermocouples, a data logger (Agilent 34970A) and a DAQ PC. Singh et al. [13] and Champier et al. [14] monitored all data of TEGs by a data logger and two hand-held measuring instruments. Kucukkomurler [15], Zhou et al. [16] and Rinalde et al. [17] used the hand-held measuring instruments.

In this study, a data acquisition and test measurement system with programmable logic controller (PLC) has been established for the measuring, testing, registering and analyzing of the data obtained from the TEGs. All of the measurement data of the thermoelectric generator have been aggregated in the new test measurement and supervisory control and data acquisition system. The cold-hot surface temperatures, the fluid flows passed over hot-cold surfaces, the current, the voltage and the power of the TEG have been measured by this data acquisition and test system. The instantly measured values have been monitored by an operator panel (OP) that was connected to the PLC whose program was specially written for this. Also, a supervisory control and data acquisition (SCADA) program has been written in order to monitor and register the measured data values by the PC. All the data values have been visualized by the SCADA program in the PC. At the same time, all the data values have been transferred to the MySQL database to be analyzed. All the data calculations of TEG have been realized both in the OP and in the SCADA programs.

Experimental setup

TEG basic structure

The structure and equivalent circuit of a TEG is given in Fig. 1. The basic structure of TEG using the electric production is made up of thermoelectric elements. When *p*- and *n*-type semiconductors are connected electrically in series and thermally in parallel, a TEM is set off [18]. TEM devices can typically be classified into thermoelectric generators (TEGs) and thermoelectric coolers (TECs). TEGs convert thermal energy from a temperature gradient to electrical energy (Seebeck effect), whereas TECs convert electrical energy into a temperature gradient (Peltier effect) [7].

The electrical equivalent circuit of the TEG consists of an ideal voltage source V and an internal resistance R_{in}. It is similar to the equivalent circuit of a battery.

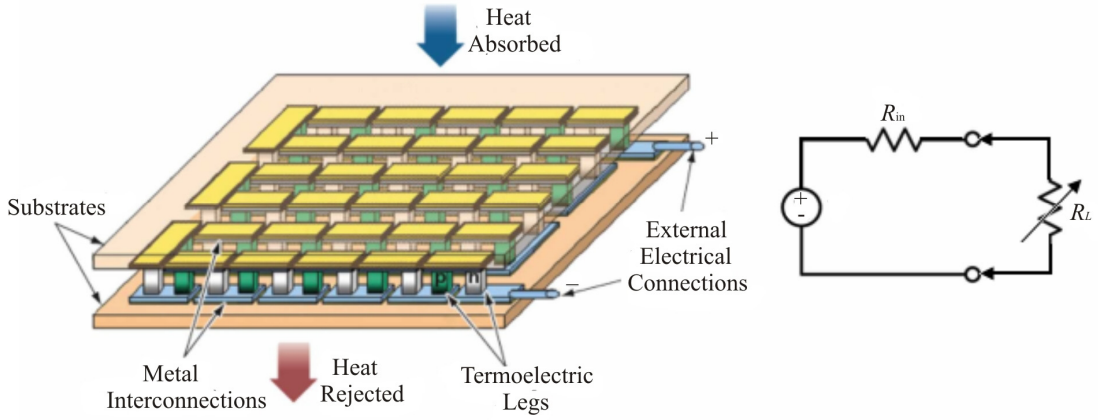

Fig. 1. A TEM in the generator mode and the equivalent circuit of the TEM.

When a temperature difference between surfaces of TEG occurs, a direct voltage (DC) across the TEG is achieved. If a load resistor R_L is connected across the TEG, the electric current passes through the load resistor and an electric power is obtained from the TEG. If the temperature difference between the surfaces of the TEG is increased, the electric power obtained from the TEG increases. The maximum power output obtained from the TEG is obtained when the internal resistor R_{in} value of the TEG equals that of the load resistor R_L. From the standpoint of TEG applications, it is highly desirable to maximize power output [18].

Experimental installation of TEG

The experimental setup of the TEG is given in Fig. 2. The main parts of the experimental setup of the TEG consists of a TEG system, a hot-cold water circulator obtained from the hot-cold water, an electric heater placed between the TEGs and an auto transformer that controls the heat of electric heater, a load resistor of the TEG, a SCADA system with PLC, sensors and transmitters.

Two TEGs, which are brand-coded Altec-GM-1, have been used in the TEG system. The flat-rolled electric heater, wired with a chrome-nickel wire of 500 W in the size of 5×5cm, has been used to provide the increased temperatures of hot surfaces of the TEGs. The heater is compressed in the form of a sandwich between two TEGs forming the hot surface temperatures of the TEGs. Hence due to this electric heater, the hot side temperature could rise up to about 200°C. Two radiators, sized 5×5×0.8 cm, have been used to provide the cold side temperature and through them, cold water from has been passed with the aid of a water circulator. Owing to an established hot-cold water system, the temperature of the cold water could reduce down to about 5 °C. In this study, while the cold side temperature has been kept constant, the hot side temperature has been raised, since power P taken from the TEG depends on the temperature difference ΔT between its surfaces.

In order to achieve a higher temperature difference in TEGs, the temperature of the hot surface has been increased by the flat-rolled electrical heater because the temperatures of the hot water, which is provided from geothermal areas, are up to about 95°C and the value along with the steam temperature reaches about 120°C. The temperature of the cold water in the application areas is about 15 °C. In this case, the temperature difference between the hot water and the cold water has been raised up to about 100°C. The temperature difference can be changed through wide ranges of about 250°C by the flat-rolled electrical heater. Via this, the reactions of the TEGs at the high-temperature have been analyzed. The power of the electric heater has been changed with an auto transformer of 2 kVA with the brand of Artes Electronics

Company. The spot-ended T-type thermocouples have been used so as to measure the temperatures of the hot-cold surfaces. Maximum temperature sensing values of T-type thermocouple temperature sensors can be up to 350 °C.

Four copper heat stabilizer plates, with sizes 4×5×0.2 cm, have been placed on each side of the TEGs. Two T-type thermocouples as the temperature sensors have been used in order to sense the temperatures of the hot T_H -cold T_C surfaces of the TEGs and in order to find the temperature difference between the surfaces. As shown in Fig. 2, these thermocouples have been placed onto the copper plate between the TEGs and they have been welded to the heat stabilizer plate. To minimize the thermal conduction resistance between the cold and hot surfaces, silicon grease has been applied to their surfaces. A resistor that is scaled and winded from the chromium-nickel wire of 300 W has been used as the load resistor.

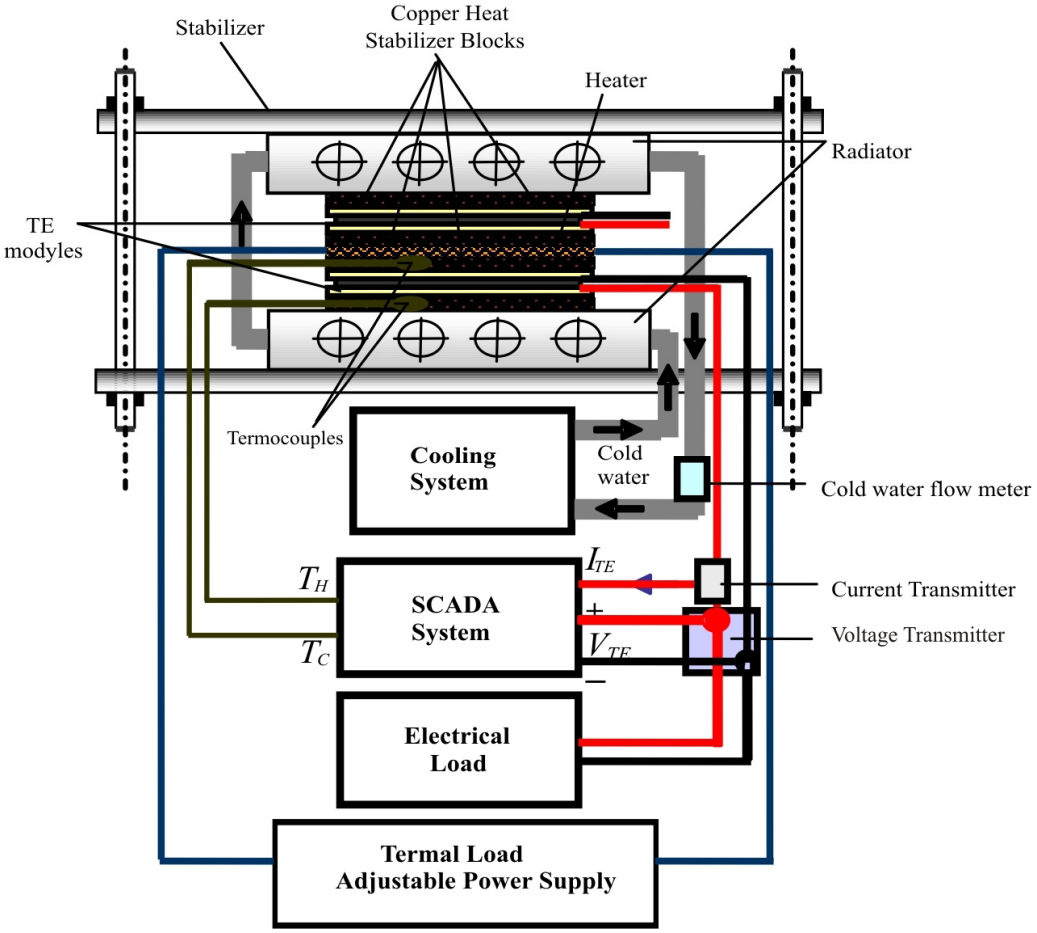

Fig. 2. TEG system block diagram of the experimental setup.

The hot-cold water circulator

A hot-cold water circulator system has been established to carry out the TEG experiments in the laboratory, as shown in Fig. 3. The main parts of the system consisted of a hot water tank, a cold water tank, an electric heater, two cooler motors, two on-off controllers, four hot-cold on-off valves, two hot-cold circulation motors and two flow meters.

In this system, the TEG system of 10 W has been used and later on the TEGs system to be used will be carried out using systems with 100 W and 1.5 kW, as sources of geothermal energy. Performance characteristics of TEG are carried out by maintaining a constant reference value for the temperatures of the hot surface T_H and the cold surface T_C.

Fig. 3. The hot-cold water circulatory system.
1 – cold water storage tank, 2 – hot water storage tank, 3 –electric heater,
4 – refrigerator motors, 5 – on-off controllers,
6 – hot/cold valves, 7 – circulation motors, 8 – flowmeters.

With this purpose, the developed hot-cold water circulator system can be used both as a source of hot water and as a source of cold water. In order to increase the temperature differences between the TEGs surfaces, the temperature of the cold surface T_C has been lowered as much as possible and kept at the lowest possible levels of about 5 °C.

During the experiments performed, the hot surface temperature of TEG has been provided with the electrical heater to measure the extreme temperature performances of TEG. During application in the field, the hot surface temperature and the cold surface temperature of TEG to be tested will be provided with the geothermal hot water and the cold public water supply, respectively. The temperatures of the geothermal resources and the temperatures of the cold public water supply are up to about 120°C and <20°C, respectively. Pipes and hoses in the hot-cold water circulatory system were selected to withstand 150°C.

The control of the hot water and the cold water systems is done separately. Cold water system has been the basis for classic air-cooled heat transfer system from water to air. An electric water heater of 2 kW has been used to heat the water in the hot water tank. Two classic cooling systems have been used to achieve a more powerful cooling. The sensing of the hot-cold water temperatures has been carried out by T-type thermocouples and their controls have been executed by the E-72 temperature controllers of Elimko Company as on-off controlled. Their hysteresis range has been selected 3°C. Two motor, which are three-speed stage, one phase and of 80 W, have been used for circulation of the hot-cold water.

Another factor that is effective for electric production from TEGs is flow. Flow measurements have been carried out by two ARF-4 HH flow meters of Micronet Company. Measuring range of the flow meter is 0.5-15 m^3/sec.

The sizes of the used water tanks are 49×69×60 cm in the hot-cold water circulator system. While the hot and the cold water pass through the hot and cold surfaces of the TEG, affect each other and between them is the exchange of heat. The interaction has been minimized with Styrofoam isolation 1 cm thick. When ambient temperature is 20°C, the hot-cold tanks are filled with water and the cooling system is run, the cold water temperature could be reduced up to about 5°C at the 6 hour. In this case, after a small swing decreasing about 2°C, the hot water tank temperature has remained at

about 15°C. In the same way, when ambient temperature is 20°C, the hot-cold tanks are filled with water and the heating system is run, the hot water temperature could be raised up to about 93°C in 6 hours. In this case, after a small swing increasing about 2°C, the cold water tank temperature has remained at about 19°C. When the hot-cold systems are run together, their temperatures have been reached in 7 hours. In this case, the hot water temperature was about 93°C and the cold water temperature was about 5°C. As a conclusion, the hot-cold temperatures in tanks did not almost affect each other through the insulation.

TEG data acquisition and SCADA

Set up of TEG data acquisition and test system (TEG-DA-TS)

A TEG data acquisition and test system (TEG-DA-TS) has been established to monitor and register to the data obtained from the TEG, as shown in Fig. 4. The TEG-DA-TS components mounted DIN rail have been consisted of a power supply of 24 VDC, a PLC, a expansion module (EM) of thermocouple, a voltage transmitter, a current transmitter, a OP, a PLC-OP communication cable, PLC-PC communication cable, a PC and two follow meters.

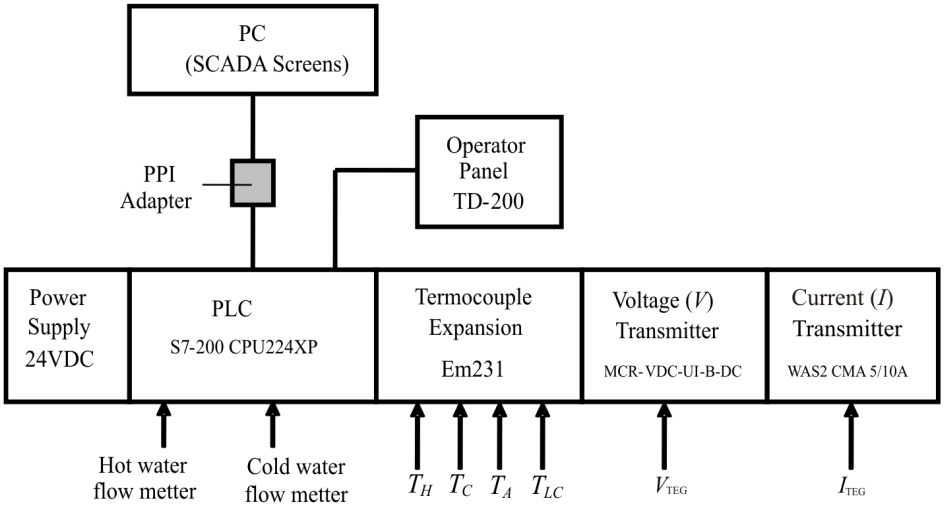

Fig. 4. TEG-DA-TS block diagram.

The system power has been provided with the seamless power supply of 24 VDC. The hot-cold surface temperatures, the ambient temperature T_A and the entering water temperature T_{LC} have been measured four T-type thermocouples. Four thermocouples have been connected to S7–200 CPU224XP PLC via the EM231. Analog temperature signals have been converted and processed into digital signals by the EM231. A WAS2 CMA 5/10A DC current transmitter branding WeidMüller and a MCR-VDC-UI-B-DC voltage transmitter branding Phoenix Contact have been used for sensing amount of current and voltage obtained from the TEG, respectively. Owing to the used current-voltage transmitters, up to 10 A DC and 550 V DC voltage values can be sensed, respectively. AN0 and AN2 analog inputs of PLC have been carried out to convert the current and voltage values into digital values. The system will be utilized on the high power TEG of 1.5 kW. Two flow meters have been used to measure the flows of water passed from the cold-hot surfaces of TEG and their pulses have been connected to the DI1 and DI4 inputs of PLC directly. For sensing the pulses of flow meters, two high speed counters of PLC have been used.

Monitoring of all data of TEG has been carried out by a TD200 OP branding Siemens and a SCADA program. The used OP has two-line and each line has 20 characters. Also, there are function keys on it. The

four temperatures, the temperature difference between surfaces, current, voltage, power, the hot-cold flows and efficiency calculations have been monitored through the OP in real time. The calibration of current, voltage and temperatures were carried out by the Fluke 725 Multifunction Process Calibrator device.

The PLC program

The used Siemens S7-200 PLC in the TEG-DA-TS is the main component. The PLC program has been written by the MicroWin program. Data inputs of PLC are the hot-cold flows, the hot-cold surface temperatures, ambient temperature, the entering water temperature, output current and output voltage of TEG.

There are two communication ports on the used PLC. Owing to these communication ports, the PLC data have been both monitored from the OP and transferred to the PC SCADA program. If a single-port PLC had been selected, the OP and SCADA could not have been used at the same time.

The PLC program algorithm is given in Fig. 5.

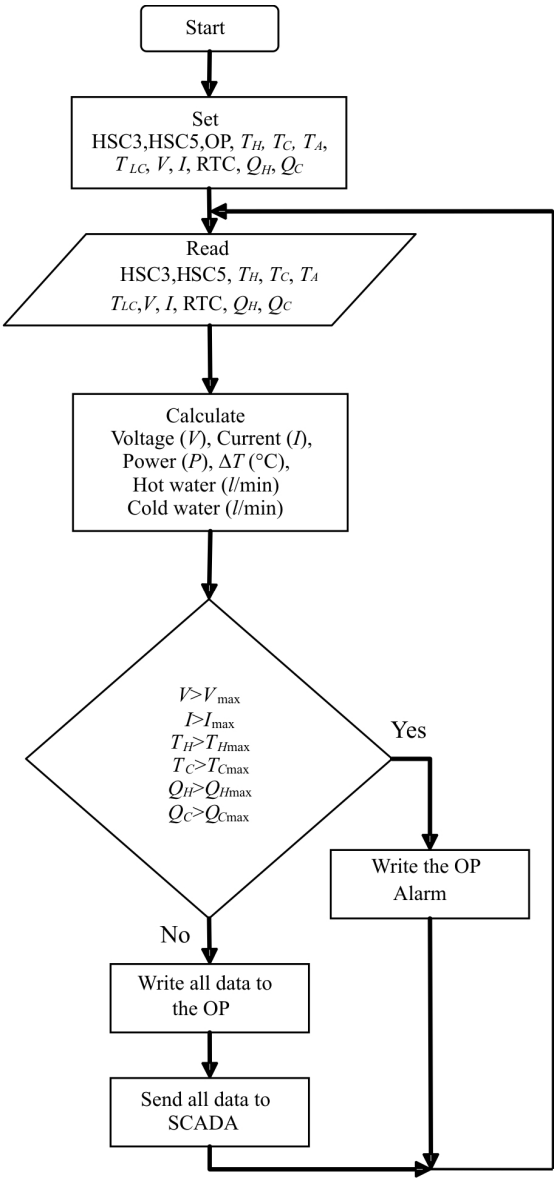

Fig. 5. Flow diagram of PLC program.

TEG's current and voltage outputs have been connected to the AI0 and AI2 inputs of the PLC, respectively. The current-voltage transmitters have been calibrated for the 0-10 V analog output. Owing to the PLC has a 16-bit registers, the analog current-voltage data has been converted into 16-bit numbers. After the necessary scaling current, voltage and power values have been calculated and transferred to the OP and SCADA. DI1 and DI2, which are high speed counter (HSC) inputs of the PLC, have been used for the hot-cold flow pulses. DI1 is the HSC3 input and DI4 is the HSC5 input. Without these HSCs being initiated, the HSCs have been configured to count the flow pulses continuously.

Interruption pulses or cut-offs in the HSC3 and HSC5 have been setup for every 10 pulses. The Counter0 (C0) and the Counter1 (C1) have been increased by one value for the hot water flow rate and the cold water flow rate with every interruption, respectively. Also in order for an interruption pulse to be formed at the end of every 10 pulses, HSC3 and HSC5 have been setup. The PLC has been set up at real time clock (RTC) so as to enable the calculations of the l/min flow rates to be obtained. AI4, AI6, AI8 and AI10 inputs of the PLC have been configured to sense four temperatures. The temperature records have been sensed up to 350°C by T-type thermocouples.

The OP program has been written by the wizard of the MicroWin program. There are four menus on the OP: the calculations, flows, I_V_P and temperatures. The point to point interface cable (PPI-485) has been used to transfer all data from the PLC to the PC SCADA program.

The SCADA program

The SCADA program interface page is given in Fig. 6. The SCADA program has been written by the WinTr SCADA program software. The SCADA program consists of four pages: Temperatures, flows, V_I_P_R and all data. The user can easily get access to the TEG data via the SCADA pages and buttons.

Fig. 6. SCADA program page.

The TEG parameters processed in the PLC have been transferred to the commercially available SCADA program via the RS485 communication line. Owing to the SCADA program, all the data of TEG have been visualized on the PC. The transfer process has been done from serial port of the PC via using the RS485 communication protocol at 9600 baud/rate. Current, voltage, power, the cold-hot temperatures, the temperature differences, the hot-cold flow rates and the flow differences values have been registered for "a second" time periods by the MySQL database in the SCADA program. The data has been programmed as historical and their graphics have been drawn to make a retrospective analysis. Analyzer can easily be seen via the changes in the system with help of the graphs. The reporting of the data desired time intervals can be done in order to be used later on. The alerts and

warnings have been added to the SCADA program in order to enable users to communicate failures that may be in the system.

Implementation and experimental results

The established TEG-DA-TS is given in Fig. 7. Power, current and voltage performance graphs of the test results obtained from the SCADA program are given in Fig. 8, only one of the modules used the Altec brand for various temperature differences. The data sources of the curves are the data savings in the MySQL database to be analyzed. In Fig. 8, the maximum current I_{SC} is when value of the load resistor R_L is equal to zero and the maximum voltage V_{max} is when value of the load resistor R_L is infinite.

a)

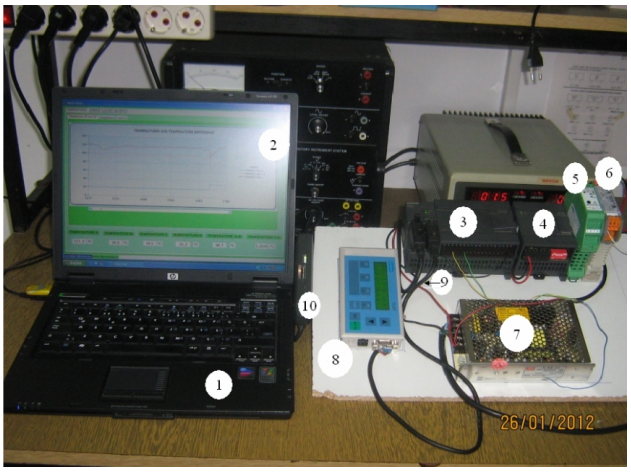

b)

Fig. 7. Established TEG-PAS system.
1 – personal computer (PC), 2 –SCADA screen, 3 – PLC,
4 – EM231 TC expension module, 5 –voltage transmitter,
6 – current transmitter, 7 – power supply, 8 – operator panel (OP),
9 – PLC-OP communication cable, 10 – PLC-PC communication cable.

The generated maximum power P_{max} and the taken maximum efficiency η_{max} in the Altec datasheets are equal to 7 W and *3.5%* in the temperature difference of ΔT=100°C, respectively. Experimentally, the highest power value has been received when the value of the load resistor is

R_L=0.72Ω, and the value is about 6.71W. In this case, the input power is Q_H=197W and efficiency of TEG have been found to be η_{max}=% 3.4. When the temperature difference between surfaces of the TEG is ΔT=50°C, the generated maximum power and the taken maximum current have decreased and hence the generated power have diminished.

Current, voltage, power curves, which have been obtained from the data that was registered and transferred from the TEG-DA-TS to the SCADA program and depending on the difference temperature, are given in Fig. 9.

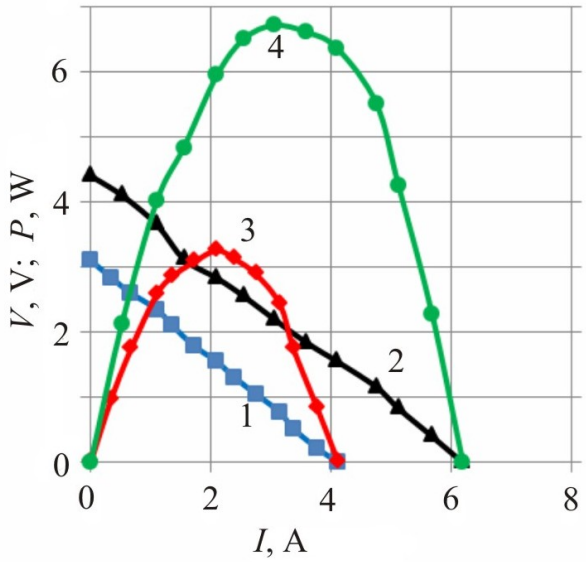

Fig. 8. Voltage and power curves comprising the data obtained from the SCADA at various temperature differences ΔT (°C). (1 – voltage (V) npu ΔT = 50 °C, 2 – voltage (V) npu ΔT = 100 °C, 3 –power (P) npu ΔT = 50 °C, 4 – power (P) npu ΔT = 100 °C)

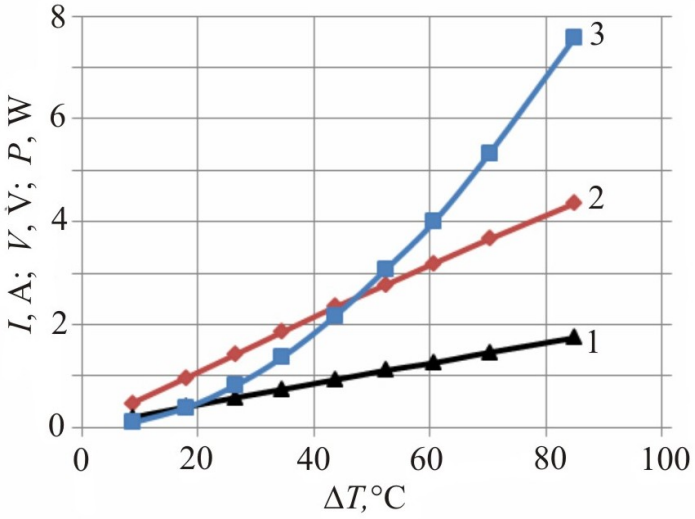

Fig. 9. Current, voltage, and power curves at various temperature differences obtained from the SCADA. (1 – voltage (I), 2 – current (V), 3 – power (P)).

The temperature difference of the TEG has been raised from ΔT=10°C to about ΔT=85°C. During the experiment, the value of the load resistance has been kept constant in R_L=2Ω. While the current value is I=0.19A in ΔT=10°C, it is I=1.75A at ΔT=85°C and it consequently has increased linearly. Also, while the voltage value is V=0.45V at ΔT=10°C, it is V=4.35V at ΔT=85°C and it

consequently has increased linearly. However, while the power value is P=0.09W at ΔT=10°C, it is P=7.58W at ΔT=85°C and it consequently has increased nonlinearly.

Conclusion

A TEG-DA-TS has been designed for the calculation of the performance of the TEG depending on the data received from the TEG and it has been applied on the pre-installed TEG system of 10 W. A SCADA program that has been written for monitoring and recording of the measured TEG parameters such as the hot-cold side temperatures, the hot-cold water flow rates, current, voltage and power values via the PC. An OP program communicating with the PLC has been written and implemented in order to instantly monitor the data independent of the PC. A hot-cold water circulator system has been established to enable carrying out the TEG experiments in the laboratory. TEGs, Altec-GM-1 brand-coded have been examined with TEG-DA-TS and the values of maximum power P_{max} and efficiency were found. When the obtained results have been compared with the TEG datasheets, the relative error for the maximum power was around 4% and the value for efficiency was below 3% by TEG-DA-TS.

In prospective study, the developed TEG-DA-TS will be used with higher-power TEG systems, such as 100 W and 1.5 kW.

Acknowledgement

This research is sponsored by NATO's Public Diplomacy Division in the framework of "Science for Peace" (NATO.NUKR.SFPP 984536).

References

1. R. Ahiska, H. Mamur, M. Ulis, Modeling and Experimental Study of Thermoelectric Module as Generator, Journal of the Faculty of Engineering and Architecture of Gazi University **26**, 889-896 (2011).
2. D.M. Rowe, Review Thermoelectric Waste Heat Recovery as a Renewable Energy Source, International Journal of Innovations in Energy Systems and Power **1**, 13-23 (2006).
3. X. Niu, J. Yu, S. Wang, Experimental Study on Low-Temperature Waste Heat Thermoelectric Generator, Journal of Power Sources **188**, 621-626(2009).
4. R. Ahiska, S. Dislitas, Computer Controlled Test System for Measuring the Parameters of the Real Thermoelectric Module, Energy Conversion and Management **52**, 27-36 (2011).
5. X. Gou, H. Xiao, S. Yang, Modeling, Experimental Study and Optimization on Low-Temperature Waste Heat Thermoelectric Generator System, Applied Energy **87**,3131-3136 (2010).
6. C. Lertsatitthanakorn, Electrical Performance Analysis and Economic Evaluation of Combined Biomass Cook Stove Thermoelectric (BITE) Generator, Bioresource Technology 98, 1670-1674 (2007).
7. H.L. Tsai, J.M. Lin, Model Building and Simulation of Thermoelectric Module using Matlab/Simulink, Journal of Electronic Materials **39**, 2105-2111 (2009).
8. C.A. Gould, N.Y.A. Shammas, S. Grainger, I. Taylor, A Comprehensive Review of Thermoelectric Technology, Micro-Electrical and Power Generation Properties, in: 26th International Conference on Microelectronics, 2008, pp. 329-332.
9. J.M. Eklund, I. Spencer, J. Zheng, D. Mercy, C. Elliot, I. Marnoch, Data Collection, Simulation and Design of a Waste Heat Energy Conversion System, in: 2009 IEEE Electrical Power & Energy Conference, 2009, pp. 1-6.

10. H.S. Han, Y.H. Kim, S.Y. Kim, S. Umd, J.M. Hyuna, Performance Measurement and Analysis of a Thermoelectric Power Generator, in: 12th IEEE Intersociety Conference on Thermal and Thermomechanical Phenomena in Electronic Systems, 2010, pp. 1-7.
11. K.J. Kim, Thermal and Power Generating Performances of Thermoelectric Energy Recovery Modules, in: 12th IEEE Intersociety Conference on Thermal and Thermomechanical Phenomena in Electronic Systems, 2010, pp. 1-7.
12. M. Hasebe, Y. Kamikawa, S. Meiarashi, Thermoelectric Generators Using Solar Thermal Energy in Heated Road Pavement, in: 25th International Conference on Thermoelectrics, 2006, pp. 697-700.
13. R. Singh, S. Tundee, A. Akbarzadeh, Electric Power Generation from Solar Pond Using Combined Thermosyphon and Thermoelectric Modules, Solar Energy **85** (2011) 371-378.
14. D. Champier, J.P. Bedecarrats, M. Rivaletto, F. Strub, Thermoelectric Power Generation from Biomass Cook Stoves, Energy 35, 935-942 (2010).
15. A. Kucukkomurler, Thermoelectric Powered High Temperature Wireless Sensing and Telemetry, in: 4th IEEE Conference on Industrial Electronics and Applications, 2009, pp. 1080-1086.
16. Y. Zhou, S. Paul, S. Bhunia, Harvesting Wasted Heat in a Microprocessor Using Thermoelectric Generators: Modeling, Analysis and Measurement, in: Design, Automation and Test in Europe, 2008, pp. 98-103.
17. G.F. Rinalde, L.E. Juanico, E. Taglialavore, S. Gortari, M.G. Molina, Development of Thermoelectric Generators for Electrification of Isolated Rural Homes, International Journal of Hydrogen Energy **35**, 5818-5822 (2010).
18. Y.K. Ramadass, A.P. Chandrakasan, A Battery-Less Thermoelectric Energy Harvesting Interface Circuit with 35 mV Startup Voltage, IEEE Journal of Solid-State Circuits **46**, 333-341 (2011).

Submitted 12.12.2014.

V.O. Dudal

V.O. Dudal

Institute of Thermoelectricity NAS and MES of Ukraine
1, Nauky Str., Chernivtsi, 58029, Ukraine

THE HARNESSING OF THERMOELECTRIC GENERATORS UNDER ASPHALT

This paper presents the schematic and operating principle of thermoelectric converter of thermal energy of soils. The physical and mathematical models of thermal generator using asphalt pavement as a concentrator of solar radiation thermal energy and those of soil thermal generator have been described. Computer models for such cases have been created. Analysis of simulation results has been made and a promising outlook for using thermoelectric generators under asphalt pavement as low-power supplies has been shown.

Key words: thermoelectric generator, asphalt pavement, low-power supply.

Introduction

General characterization of the problem. To achieve essential changes in energy saving is one of the key tasks of economic policy in the overwhelming majority of countries worldwide. Under the conditions of growing prices for energy resources, the use of state-of-the-art energy-efficient technologies yields tangible economic benefits and competitive advantages.

Fig. 1. Appearance of Altec-8027.

Power consumption level of many modern electronic devices (sensors, light-emitting diode lamps, etc) is from tens of milliwatts to several watts, leading to a search for efficient low-power supplies.

One of the variants of solving this problem is the use of thermoelectric power supplies utilizing the thermal energy of soil [1, 2].

Physical fundamentals for creation of such soil thermoelectric generators (STEG) have been created in the Institute of Thermoelectricity [3]. Based on the results of theoretical studies, samples of STEG have been developed and manufactured [3]. One of the variants of STEG is shown in Fig. 1.

Powers generated by soil thermoelectric generators become commensurate to power consumption of low-power electronic devices. With regard to a number of known advantages of STEG, their use as power supplies with service life up to 30 years becomes increasingly attractive [3, 4].

Ref. [5, 6] describe systems of energy harvesting and thermal into electric energy conversion that can be installed on the surface of road pavement and used for power supply to various sensors, road signs illumination, etc.

The purpose of this work is to study the possibilities of improving thermoelectric generators with a concentrator of solar radiation thermal energy in which capacity asphalt pavement is considered.

Physical model of soil TEG

A physical model and operating principle of thermoelectric generator using the thermal energy of soil is shown in Fig. 2.

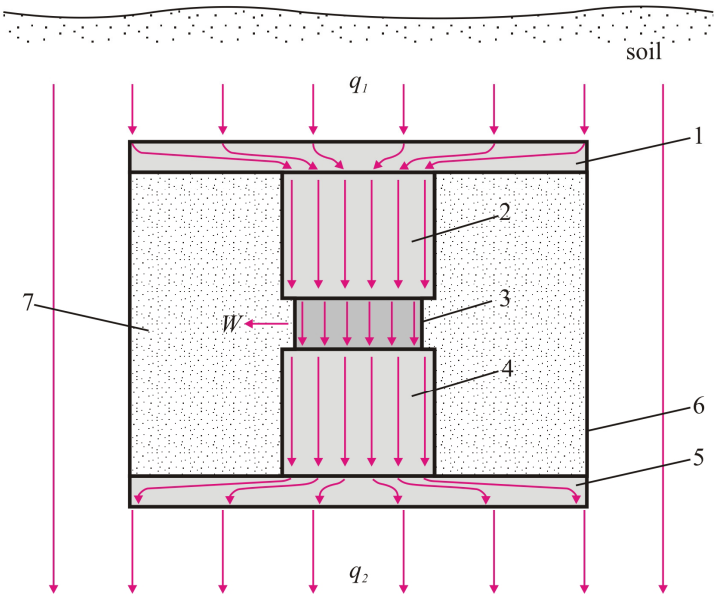

Fig. 2. A physical model of thermal generator arranged in soil.

Thermoelectric generator arranged in soil is composed of heat-absorbing collector 1, heat conductor 2, high-performance multi-element thermopile 3, heat conductor 4, heat sink 5, case 6 and thermal insulation 7. The operating principle of thermal generator is as follows: heat flux q existing in soil comes to heat-absorbing collector 1, is fed by heat conductor 2 to the hot junctions of thermopile 3, removed by heat conductor 4 to heat sink 5 and scattered to lower layers of soil. To reduce thermal losses, case 6 of thermal generator is filled with heat-insulating material. Passing through the thermopile, heat creates temperature gradient thereupon which results in the generation of electric power W. It is noteworthy that throughout the day a direction of heat flow can change to the opposite. Therefore, structural components 1, 2 and 4, 5 of the generator are functionally interchangeable. This model is concerned with a quasi steady-state case whereby the dynamic processes in soil are

considered to be slow. Under these conditions the heat capacity of power supply is ignored.

Mathematical description of a physical model of soil TEG

Let us consider a cylinder-shaped soil thermal generator of height *H* and diameter *D*, with its heat-absorbing pad arranged at the depth *h* under the surface of soil [3].

In order to simplify a mathematical description of a physical model of soil thermal generator, we shall consider our model in a cylinder system of co-ordinates *r*, *z* where *z* axis is directed from the surface deep into soil.

To find the distribution of temperatures *T (r, z)* and thermal flow *q* in soil in the presence of STEG, one should first solve the thermal conductivity equation:

$$\frac{1}{\chi}\frac{\partial T(r,z)}{\partial t}=\frac{\partial^2 T(r,z)}{\partial r^2}+\frac{1}{r}\frac{\partial T(r,z)}{\partial r}+\frac{\partial^2 T(r,z)}{\partial z^2} \tag{1}$$

With the boundary conditions

$$-k_0\frac{\partial T(r,z)}{\partial z}=q_0,\ z=0, \tag{2}$$

$$T(h,r<D/2)=T_{н}, \tag{3}$$

$$T(H+h,r<D/2)=T_l, \tag{4}$$

$$-k_0\int_s\frac{\partial T(r,z)}{\partial z}dS=\frac{1}{R_{\text{STEG}}}(T_{н}-T_1),\ z=h, \tag{5}$$

$$-k_0\frac{\partial T(r,z)}{\partial r}=0,\ \ h<z<h+H,\ \ r=D/2, \tag{6}$$

where q_0 is the value of specific heat flux on the surface; $T_{н}$, T_l are unknown temperatures of the receiving pad and lower end face of STEG to be determined; R_{STEG} is thermal resistance of STEG.

The physical meaning of the above boundary conditions is as follows: condition (2) assigns heat flux on the surface of soil; (3) and (4) express isothermality conditions of cylinder STEG end faces, (5) is a condition of thermal balance of STEG receiving pad, and (6) is a condition of adiabatic insulation of its lateral surface. The distribution of temperatures *T (r, z)* in soil in this case is a solution of exterior boundary-value problem for Eq. (1).

The electric power output of STEG in the general case can be written as:

$$W=f\left[T(r,z),k_0(r,z),\sum_{i=1}^{N}B_i,Z^*,L(r,z)\right], \tag{7}$$

where *T (r, z)* is temperature distribution in soil with STEG arranged in it; $k_0(r,z)$ is thermal conductivity coefficient of soil; $\sum_{i=1}^{N}B_i$ is an algebraic sum of *N* components of thermal balance in soil; Z^* is thermoelectric figure of merit of thermopile in STEG; $L(r,z)$ is spatial coordinate of STEG arrangement in soil that characterizes its geometrical dimensions.

Computer simulation of soil TEG

To study the work of soil thermoelectric generator under the steady state (the temperature on the surface of soil was 300 K, and at the depth of 55 cm – 285 K), a three-dimensional computer model of such generator was created. The computer model was built with the use of the Comsol Multiphysics software package [7] which permits simulation of thermophysical processes occurring in soil and TEG.

Calculation of temperature and heat flux density distributions in the thermoelectric generator and soil was done by finite-element method (Fig. 3) the essence of which is that object under study is split into a large number of finite elements, and in each of them the value of function is sought for that satisfies given differential equations of second order with the respective boundary conditions. The accuracy of solving the formulated problem depends on the level of splitting and is assured by the use of a large number of finite elements [7].

Object-oriented computer simulation was used to obtain temperature distributions (Fig.4) in soil thermoelectric generator under the steady state.

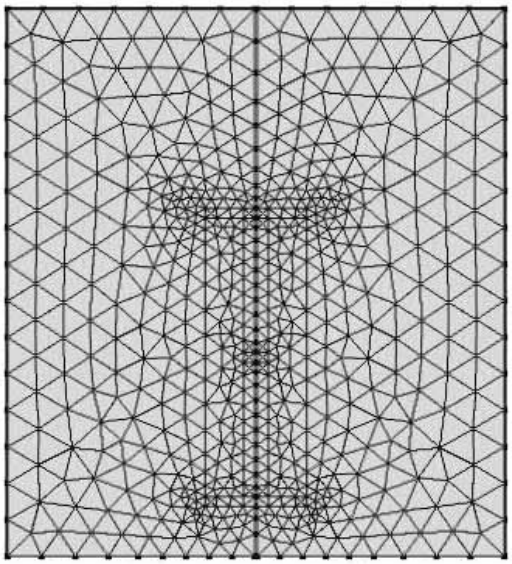

Fig. 3. Finite-element method mesh.

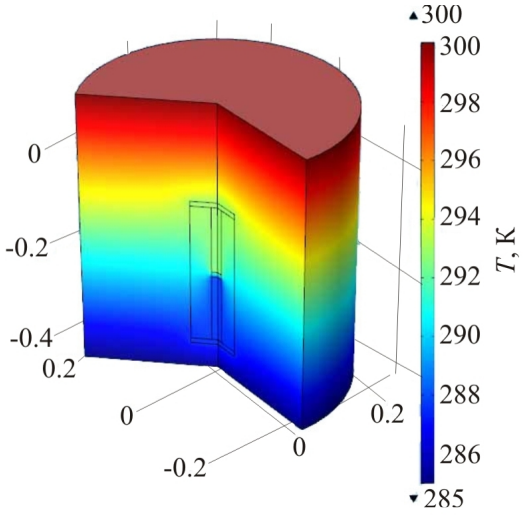

Fig. 4. Temperature distribution in TEG and soil.

Physical model of TEG under asphalt pavement

One of the simplest variants to improve the operating efficiency of STEG seems to be its arrangement under asphalt that has much better coefficient of solar energy absorption.

A physical model of thermoelectric generator under asphalt pavement is represented in Fig. 5.

According to the physical model, an area of road pavement is a structure of five layers (asphalt pavement 1, concrete floor 2, a layer of broken stones 3, a layer of sand 8, soil 9) whose thermophysical characteristics (thermal conductivity κ, density ρ) and layer thicknesses are given in Table 1.

Soil thermoelectric generator is a cylinder bar which consists of heat-absorbing collector 4, thermal insulation 5, thermopile 6 and heat sink 7. The generator dimensions: Ø10×30 (cm).

The collector and heat sink of STEG are made of aluminum and consist of heat-absorbing (heat-dissipating, respectively) plates of size Ø10×1 (cm) and heat conductor of size Ø2.256×13.48 (cm). Mineral wool with thermal conductivity coefficient κ_{insul}= 0.032 $W \cdot m^{-1} \cdot K^{-1}$ is used as thermal insulation.

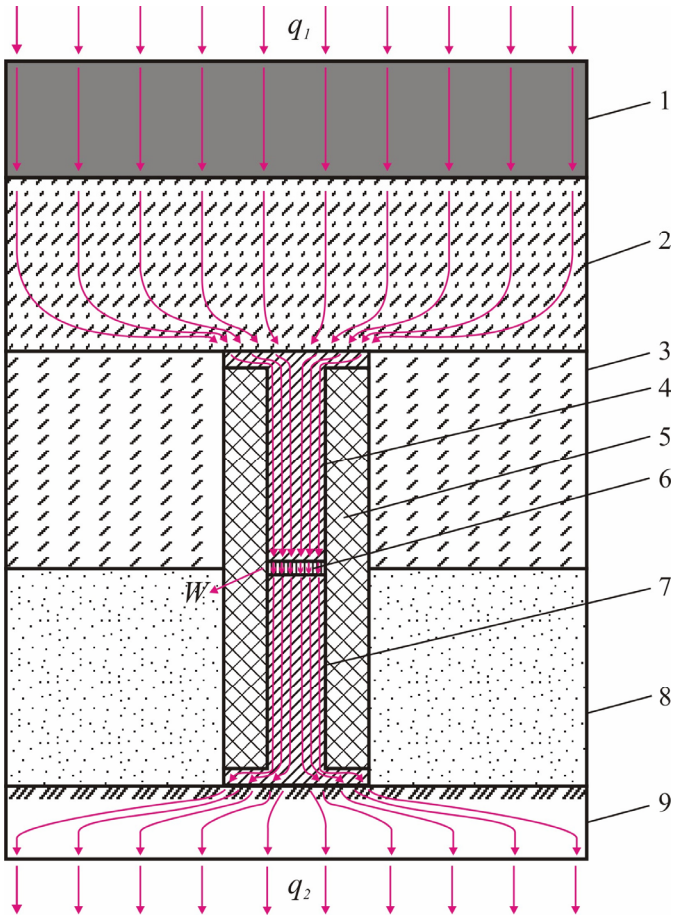

Fig. 5.A physical model of STEG under asphalt:

1 – asphalt pavement, 2 – concrete floor, 3 – layer of broken stones, 4 – heat-absorbing collector, 5 – thermal insulation, 6 – thermopile, 7 – heat sink, 8 – layer of sand, 9 – soil.

As is known, the EMF value of thermopile is mainly affected by temperature difference ΔT between its surfaces. Therefore, to achieve the objective of this paper, a bulk homogeneous sample of

Bi_2Te_3 semiconductor material of thermal conductivity $\kappa_t = 1.8\ W \cdot m^{-1} \cdot K^{-1}$ was considered as a thermopile. The thermoelectric converter is a cylinder bar of geometric dimensions Ø2.256×1.04 (cm).

Table 1

Thermophysical properties of physical model components

	Thermal conductivity, κ ($W \cdot m^{-1} \cdot K^{-1}$)	Density, ρ ($kg \cdot m^{-3}$)	Density of layer, m
Asphalt pavement	1,05	2100	0,08
Concrete floor	1,51	2400	0,12
Broken stones	0,064	200	0,15
Sand	0,35	1600	0,15
Soil	0,4	1800	0,05

In this physical model, asphalt pavement, concrete floor, broken stones, sand and soil will be considered to be homogeneous media and the fact that their thermal conductivity varies as a function of ambient conditions, namely humidity, temperature, material structure, etc. will be disregarded. Thermal processes are assumed to be slow, so a quasi-steady state is considered whereby TEG heat capacity is ignored.

Mathematical description of a physical model of TEG under asphalt pavement

The amount of heat passing through asphalt pavement (Q_1) is the difference in the amount of heat coming to asphalt surface (Q_0) and the heat reflected from it. The reflection factor of asphalt pavement is 7 %, hence the expression for Q_1 will be as follows:

$$Q_1 = 0.93 \cdot Q_0 . \tag{8}$$

Heat flows passing through the asphalt Q_2, concrete Q_3 and aluminum heat conductor Q_4 are given by the expressions:

$$Q_2 = \kappa_{asf} \cdot \frac{S_{asf}}{L_{asf}} \cdot (T_2 - T_1),\ Q_3 = \kappa_{bet} \cdot \frac{S_{bet}}{L_{bet}} \cdot (T_3 - T_2),\ Q_4 = \kappa_{Al} \cdot \frac{S_{Al}}{L_{Al}} \cdot (T_4 - T_3), \tag{9}$$

where S_{asf}, S_{bet}, S_{Al}, L_{asf}, L_{bet}, L_{Al}, κ_{asf}, κ_{bet}, κ_{Al} are the areas of heat-absorbing pads, layer thickness and thermal conductivity of asphalt, concrete and aluminum heat conductor, respectively; T_1, T_2, T_3, T_4 are the temperatures of heat-absorbing asphalt pad, "asphalt-concrete" contact, "concrete-heat-absorbing pad of aluminum heat conductor" contact, "heat-absorbing pad of aluminum heat conductor-thermoelectric converter" contact, respectively.

Heat flows on the hot Q_{hteb} and cold Q_{cteb} side of thermoelectric converter for the case of homogeneous isotropic material:

$$Q_{hteb} = \alpha_{teb} \cdot T_4 \cdot I - \frac{1}{2} \cdot I^2 \cdot \sigma_{teb} \cdot \frac{L_{teb}}{S_{teb}} - \kappa_{teb} \cdot \frac{S_{teb}}{L_{teb}} \cdot (T_4 - T_5), \quad (10)$$

$$Q_{cteb} = \alpha_{teb} \cdot T_5 \cdot I + \frac{1}{2} \cdot I^2 \cdot \sigma_{teb} \cdot \frac{L_{teb}}{S_{teb}} - \kappa_{teb} \cdot \frac{S_{teb}}{L_{teb}} \cdot (T_4 - T_5), \quad (11)$$

where α_{teb}, σ_{teb}, κ_{teb} are the Seebeck coefficients, electric conductivity and thermal conductivity of thermoelectric converter, respectively; I is current generated by converter; S_{teb}, L_{teb} are the area and height of thermoelectric converter, respectively; T_4, T_5 are "hot" and "cold" side temperatures of thermoelectric converter, respectively.

Knowing the hot and cold side temperatures of thermoelectric converter, it is possible to obtain the values of heat flows on these sides. And, with the knowledge of the flows, we can calculate converter power (W) by the following relationship:

$$W = Q_{hteb} - Q_{cteb}. \quad (12)$$

Computer simulation of TEG under asphalt pavement

To investigate the work of thermoelectric generator under asphalt pavement in the steady state (the temperature on the surface of soil was 300 K, and at the depth of 55 cm – 285 K), a three-dimensional computer model was created using the Comsol Multiphysics software package.

Computer simulation allowed obtaining temperature distributions (Fig. 6) in thermoelectric generator under asphalt pavement in the steady state.

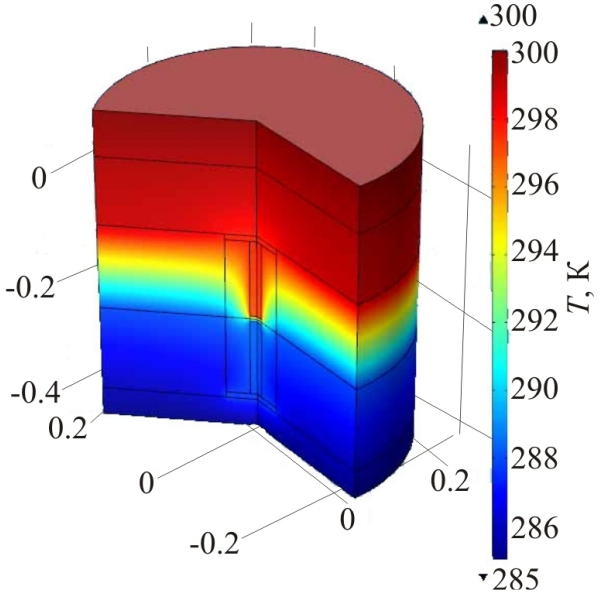

Fig. 6. Temperature distribution in TEG under asphalt pavement.

Discussion of simulation results

Figs.7 and 8 show isotherm lines obtained by computer simulation for thermoelectric generator in soil and under asphalt pavement.

From the analysis of Figs.7 and 8 it is evident that asphalt pavement brings about the increased concentration of isothermal lines passing through thermoelectric converter. In this way a greater temperature difference is obtained, which yields higher thermopower of generator. Thus, the value of temperature difference on the converter of thermal generator under asphalt pavement was ΔT=7.73 K (with a general difference of 15 K), and on thermoelectric generator in soil under identical conditions - ΔT=4.43 K. As is known, the value of generated electric power of thermoelectric converter is directly proportional to its thermopower value which is given by the relationship

$$E = \alpha \cdot \Delta T, \tag{13}$$

α is the Seebeck coefficient, ΔT is temperature difference between the upper and lower surfaces of thermal converter.

Thus, the electric power of thermoelectric generator under asphalt pavement was 1.55 mW which is almost twice greater than the electric power of soil generator (≈0.8 mW) under similar conditions.

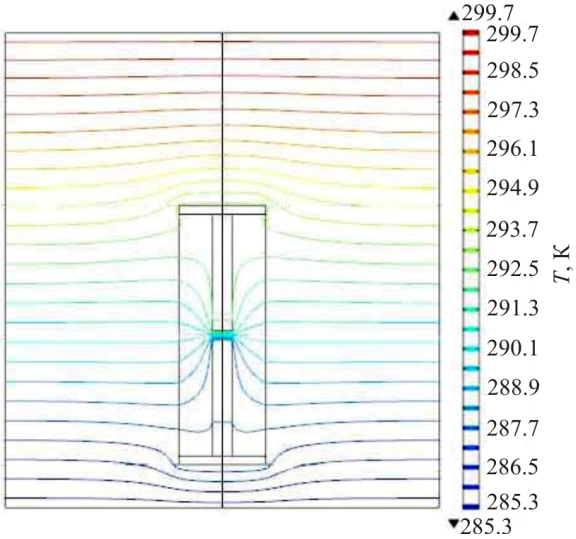

Fig. 7. Isotherm lines for thermoelectric generator in soil.

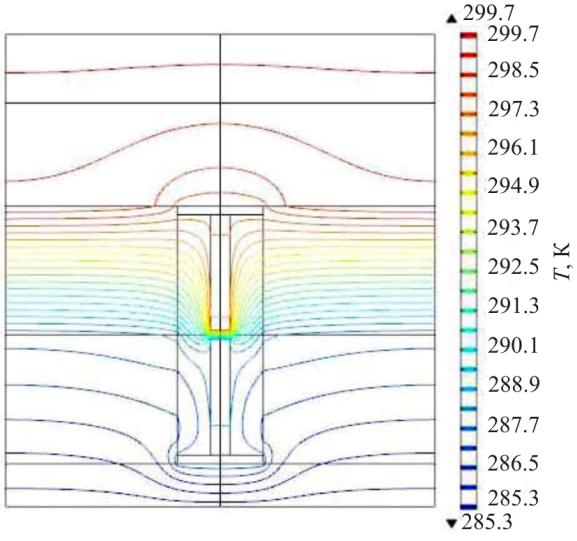

Fig. 8. Isotherm lines for thermoelectric generator under asphalt pavement.

Thus, due to the use of heat-concentrating materials, such as asphalt on the surface of heat-absorbing pad of STEG, its power can be increased considerably, which is important for low-power electronic equipment supply. Placing such generators opens up the prospects for their use in road asphalt pavement with a view to supply various sensors, light-emitting diode lamps for roadway lighting, road signs illumination, etc.

Conclusions

1. A physical model and computer simulation of thermoelectric generator in the steady state using temperature difference in soil have been developed for the case of placing the generator under asphalt pavement.
2. Based on a specific example of generator Altec-8027 it has been confirmed that the presence of asphalt pavement improves the energy parameters of generator, the voltage and power approximately 1.7 fold.

References

1. L.I.Anatychuk, P.D.Mykytyuk, Thermal Generators Using Heat Flows in Soils, J.Thermoelectricity **3**, 86-95(2003).
2. P.D.Mykytyuk, N.S.Petrenko, Thermoelectric Power Supply Using the Heat of Soil, J.Thermoelectricity **2**, 73-80 (2003).
3. P.D.Mykytyuk, Devices for Thermoelectric Conversion of Thermal Energy of Soil: PhD Thesis in Physics and Mathematics: 01.04.01, 2004.
4. L.I.Anatychuk, Thermoelements and Thermoelectric Devices. Handbook (Kyiv: Naukova Dumka, 1979), 767 p.
5. Guangxi Wu, Xiong (Bill) Yu, Thermal Energy Harvesting System to Harvest Thermal Energy across Pavement Structure, International Journal of Pavement Research and Technology **5**(5), 311-316 (2012).
6. Kanghwi Lee, Seunghoon Kim, Jaejun Lee, Cheolmin Baek, Fundamental Study to Apply Energy Harvesting Technology in Asphalt Pavement, ISAP 2104 Student Poster Competition.
7. Comsol Multiphysics User's Guide, COMSOLAB, 2010, 804 p.

Submitted 09.12.2014.

S.F. Zaparov

S.F. Zaparov
Institute of Thermoelectricity NAS and MES of Ukraine
1, Nauky Str., Chernivtsi, 58029, Ukraine

THERMOELECTRIC MATERIAL PROCESSING TOOLS AND THEIR COMPARATIVE ANALYSIS

This paper studies different methods for dimensional processing of thermoelectric materials based on Bi_2Te_3. A comparative analysis of processing tools has been made with regard to the depth of damaged surface layers of thermoelectric materials based on bismuth telluride. The benefits and drawbacks of operating practices while processing thermoelectric materials have been determined.

Key words: thermoelectric materials, processing methods, bismuth telluride

Introduction

Thermoelectric cooling and generator modules comprise the legs of semiconductor thermoelectric materials (TEM) based on Bi_2Te_3. These materials in the majority of cases are produced by vertical zone melting, the Bridgman or Czochralski methods. Extrusion method is widely used as well.

Normally, the thermoelectric materials produced by said methods are of cylinder shape in the form of samples of diameter from 10 to 30 mm at the length from 50 to 400 mm. From these samples one must manufacture *n* – and *p*–type legs shaped as parallelepipeds with their edges in the range from several tenths of a millimeter to several millimeters.

To manufacture the legs, it is necessary to perform dimensional processing of thermoelectric material samples. The main requirement to dimensional processing is retention of thermoelectric figure of merit of TEM. The cost and productivity of dimensional processing are also important.

The paper is concerned with a comparative analysis of the existing methods and tools for dimensional processing of TEM based on Bi_2Te_3.

Methods for dimensional processing of materials

Methods for dimensional processing of materials are divided into the following main groups:

- electron-beam;
- light-beam (laser);
- electroerosion;
- electrochemical;
- mechanical.

Electron-beam and laser methods for dimensional processing of semiconductor materials are widely used in microelectronics. However, they are not employed for dimensional processing of materials based on Bi_2Te_3, as long as high energy densities on interaction with bismuth telluride lead to submelting of near-surface layers and considerable reduction of the figure of merit.

Electroerosion processing methods are based on the laws of erosion (destruction) of electrodes of conductive materials on passing of pulsed electric current between them. These methods include electric spark, electric pulse processing and high-frequency electric spark, electric pulse and electric contact processing. Electric spark processing employs pulse spark discharges between electrodes one of which is a billet being processed (anode), and the other is a tool (cathode). Electric pulse processing employs electric pulses of long duration (500-10000 μsec), which results in arc discharge. Electric pulse processing is advisable to be used during preparatory work. The accuracy of dimensions and the roughness of processed surfaces depend on processing mode. High-frequency electric spark processing is employed for increasing the accuracy and reducing the roughness of surfaces processed by electroerosion method. The method is based on the use of low-power electric pulses at the frequency of 100-150 kHz.

Electric contact processing is based on local heating of billet at point of contact with tool electrode and removal of softened or even molten metal from processing zone by mechanical method, i.e. relative motion of the billet and tool. Pulse arc discharges serve as the source of heat in processing zone. Electric contact processing by fusion is recommended for large-size parts.

For the dimensional processing of TEM the major use is of electric spark method (Fig. 1).

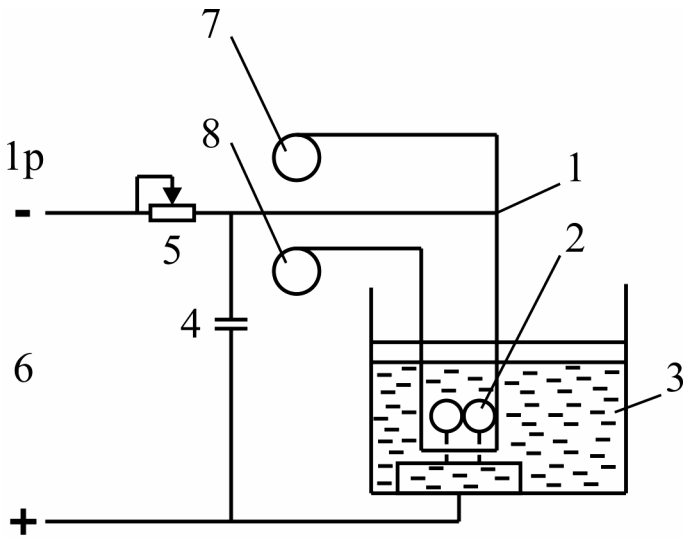

Fig. 1. Schematic of electric spark processing of TEM:
1-tool wire, 2-ingots (TEM), 3-medium where a discharge is made,
4- capacitor, 5-rheostat, 6-power supply, 7-wire coil,
8-spent wire coil 1p-electric spark processing mode.

As two electrodes 1 and 2 approach each other and voltage sufficient for break down of the resulting electrode gap is connected to them, this creates an electric discharge in the form of a narrow conducting column with the temperature measured by tens of thousands of degrees. At the base of this column, destruction (fusion, evaporation) of electrode material takes place. Tool electrode is a continuously moving brass, tungsten or molybdenum wire of diameter 0.05-0.3 mm. Processing is done in working liquid medium in the capacity of which water is employed. Liquid medium provides for the origination of dynamic forces necessary for the removal of destructed material. Cooling the electrodes, liquid stabilizes the process.

The specific features of this process are as follows: relatively low processing productivity, wire electrode wear, the use of mostly relaxation (depending on the state of electrode gap pulse) circuits

that generate pulses of duration 10-200 μsec at the frequency of 2-5 kHz and the use of direct current polarity. Near-surface damaged layers that are formed on the processed surface of thermoelectric material based on bismuth telluride reduce the figure of merit of legs. Therefore, removal of damaged layer by chemical etching is a mandatory procedure.

Electrochemical dimensional processing is characterized by high power consumption and special electrolyte needed for efficient cutting of bismuth telluride. Therefore, for mass production of TEM legs this method is not used.

Mechanical dimensional processing of thermoelectric materials has unique features. As long as bismuth telluride is characterized by low mechanical strength and fragility, the usual mechanical methods of dimensional processing are unacceptable. In fact, the only method for mechanical processing of thermoelectric materials based on Bi_2Te_3 is processing with the use of bound or free abrasives.

Cutting of thermoelectric material is made by steel blades, discs, metal wires using abrasive powder (free abrasive) or coated by diamond grains (bound abrasive).

To abrasive materials can belong any natural or artificial material whose grains possess certain properties, namely hardness, abrasive ability and mechanical durability. The main feature of abrasive materials is their high hardness as compared to other materials, which forms the basis for all machining processes.

Hardness shall mean the ability of abrasive material to resist indentation of other material that does not take permanent set.

Abrasive ability shall mean the possibility to use one material for processing the other or a group of various materials.

Mechanical durability shall mean the ability of abrasive material to withstand mechanical loads without ruptures on machining.

Diamond is the hardest known material. Its microhardness is $9.8 \cdot 10^{10}$ N/m^2. In industry, use is mainly made of artificial diamonds made of graphite processed under high pressure and temperature.

Cutting by steel blades or sets of blades with the use of abrasive suspension is schematically shown in Fig 2.

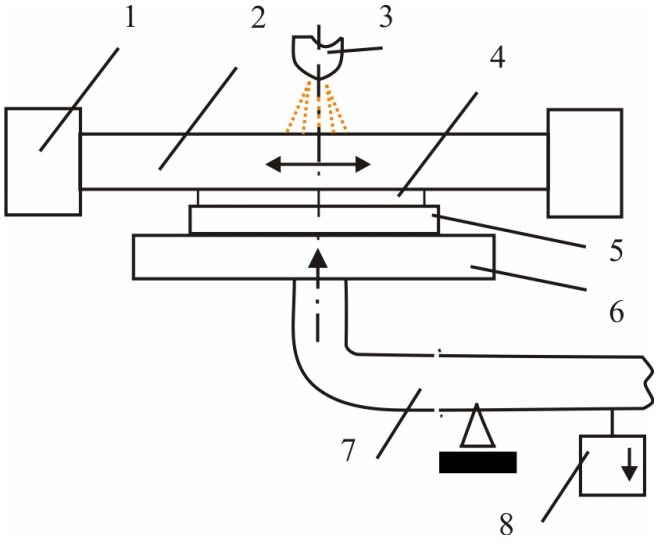

Fig.2. Cutting by steel saw blades:
1 – holder, 2 – steel saw blade, 3 – suspension feed nozzle,
4 – material to be cut, 5 – gasket, 6 – table, 7 – lever, 8 – weight.

Abrasive suspension is fed into cutting zone and, being accelerated due to motion of blades, strikes forcibly the material being processed and chips microparticles from it. Cutting process accelerates abrasive particles gradually renewable in the gap between steel saw blades and thermoelectric material. Abrasive suspension removes heat from cutting zone fairly well and does not require special cooling.

The method does not assure high productivity and quality because of the irregular tension of blades in the holder, their vibration and irregular wear.

Wire saw is a wire 0.08 – 0.10 mm thick. Cutting is executed by a set of wire saws (Fig.3) with the use of a free abrasive.

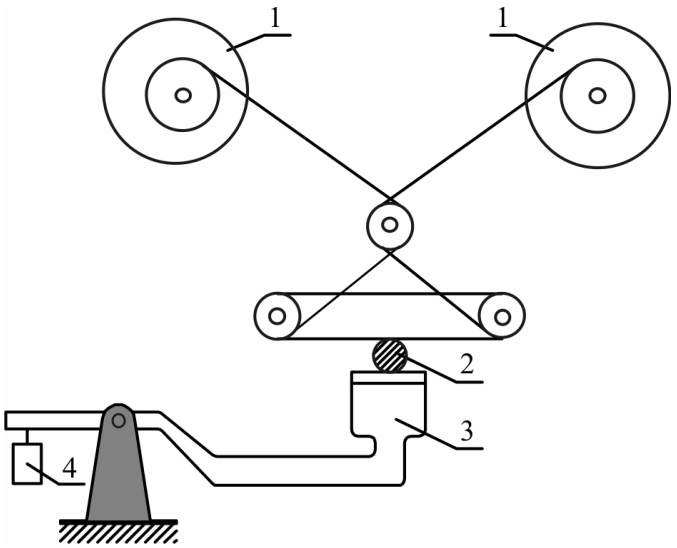

Fig. 3. Cutting by wire:
1 – wire, 2 – material, 3 – lever, 4 – weight.

Wire saw allows simultaneous cutting of billet into a large number of discs, in which case considerable saving of processed materials is achieved at the cost of the thickness of cut plates and sawcut width. But the main advantage of wire cutting is that this method yields processed samples with minimum damages of crystal structure in view of low thermodynamic stresses arising in the area of tool contact to processed material. However, there are some restrictions inherent in this method not allowing wide and efficient use of wire tools for cutting large-size crystals. They primarily include low wire stability, and wire resistance is equal in all directions, which to a large extent affects the macroprofile of surfaces in process. This method is ineffective, and its cost is rather high, so it is employed only for low-depth cutting, where efficiency is of little significance.

Cutting by disc with the outer diamond blade as compared to cutting by saw blades or a wire with the use of abrasive suspension offers higher productivity. The process is schematically shown in Fig. 4.

Diamond-bearing cutting layer is deposited on the metal disc by means of a special bond. Of all bond types (organic, ceramic, metallic) only metallic bond assures full adhesion of diamond-bearing layer to the metal disc. The central part of the disc is fastened on machine spindle. Such fastening does not assure high disc rigidity. Cutting blade protrudes beyond the outer diameter of clamping flanges not more than by 1.5 mm of cutting width. In the process of cutting disc should not vibrate and deviate from the plane, which is rather difficult to be done.

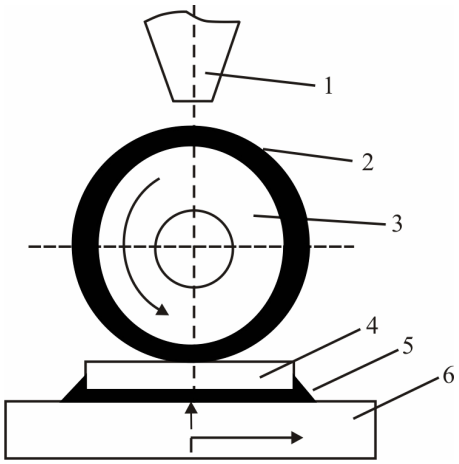

Fig. 4. Cutting by diamond disc with the outer cutting blade:
1 – lubricoolant feed nozzle, 2 – disc cutting blade, 3 – disc base,
4 – material to be cut, 5 – adhesive paste, 6 – substrate

The method of cutting by diamond disc with the inner cutting blade (Fig.5) can be used to cut ingots into discs and discs into separate crystals. The disc is based on steel foil 0.1, 0.2 mm thick whose inner blade is coated by abrasive using the above described galvanic technique.

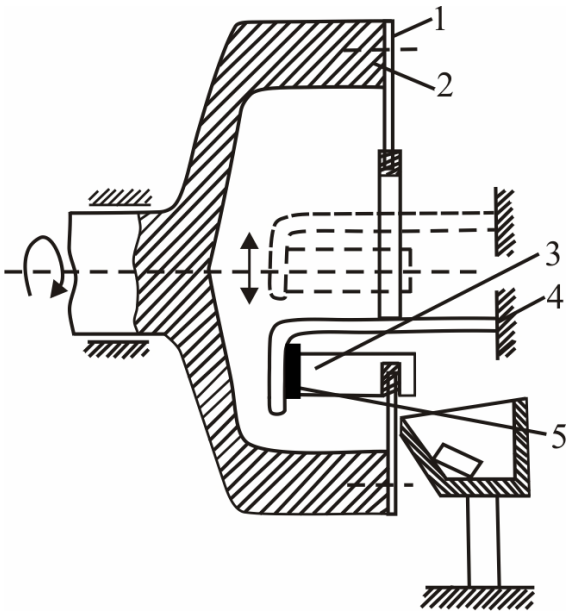

Fig. 5. Cutting by diamond disc with the inner cutting blade:
1 – diamond wheel with the inner cutting blade, 2 – cylinder,
3 – ingot, 4 – mandrel, 5 – adhesive paste

The benefits of cutting include high cutting speed, good quality of surface treatment, small thickness variation and low material waste. However, increasing disc rotation frequency above 5000 rpm causes machine vibration and temperature rise in cutting area. The drawbacks of cutting are as follows: complexity of diamond disc installation, tension and alignment, that is, dependence of treatment quality and precision on the precision and quality of the tool.

The concept of cutting by diamond-coated wires is practically the same as cutting by diamond discs, but owing to its flexibility, tension of wires along the entire instrument plane is uniform (Fig.6). Tungsten wires are arranged on a replaceable frame which serves as a cutting tool. The distance between the wires is assigned by spacer bars.

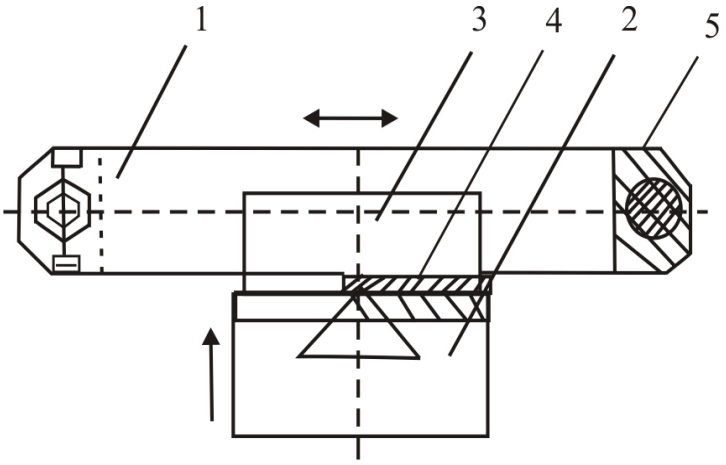

a)

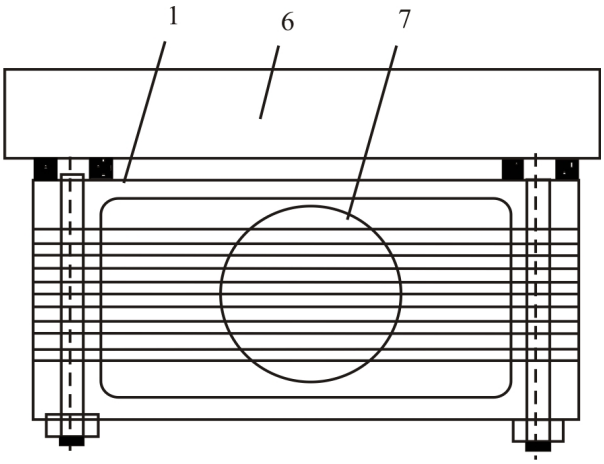

b)

Fig. 6. Diamond-coated frame:
1 – frame, 2 – table, 3 – TEM, 4 – gasket,
5 – spacer bars, 6 – carriage, 7 – diamond-coated wires.

With the above treatment methods (Table 1) the damaged near-surface layers possess degraded mechanical properties, as a result of which the adhesion strength is lowered, reducing the mechanical strength.

Comparative analysis of different types of equipment for cutting Bi_2Te_3 based materials has shown that cutting by wires with the use of free abrasive is more acceptable. However, cutting speed in this case is rather low (0.1÷ 0.3 mm/min), making such technique unviable.

Cutting by diamond-coated wires is much more efficient. The speed in this case is increased to 1 mm/min, and using a series of parallel simultaneously cutting wires increases the productivity of such cutting technique.

Table 1

Dependence of damaged layer thickness on treatment method

Cutting technique	Damaged layer thickness, μm
Wire cutting with a free abrasive	5 ÷ 15
Wire cutting with fixed diamond grains	10 ÷ 25
Electric spark cutting	20 ÷ 30
Cutting by a diamond disc with the inner cutting blade	30 ÷ 50
Cutting by diamond disc with the outer cutting blade	50 ÷ 65

Electric spark cutting is less attractive because of increased damaged layer thickness and low productivity.

The use of diamond discs with the inner and outer cutting blades is the worst method which eventually results in the degradation of thermoelectric material quality.

Thus, in the industrial production for a large-scale manufacture of thermoelectric cooling modules and generators the most promising technique is cutting by diamond-coated wires with the use of machines Altec-13005M (Fig.7).

Fig. 7 The machines Altec-13005M

High speed of cutting tool motion is provided by the use of hydrostatic guides with liquid friction. High productivity is assured by simultaneous cutting of billets on four machine worktables at a speed of 0.8÷1.0 mm/min which allows using it for mass production of thermoelectric modules.

Table 1

Main technical data and specifications of Altec – 13005M machine

1	Maximum dimensions of billets to be cut, mm	50×50×14
2	Number of wires Ø 0.14 on the frame minimum, pcs.	1
3	Number of wires Ø 0.14 on the frame maximum, pcs.	119
4	Minimum cut width, mm	0.22
5	Number of worktables, pcs.	4
6	Worktable travel, mm, not less	25
7	Worktable delivery drive	hydraulic
8	Operating pressure in worktable delivery drive, MPa	0.24-0.35
9	Frequency of cutting carriages movement, double strokes per min, up to	1400
10	Carriages travel, mm	36±0.5
11	Weight, kg, not more	150
12	Electric power requirement (without recycling water supply station), kW	0.7
13	Supply voltage of frequency 50 Hz, V	380
14	Dimensions, mm	1700×1200×500

210 000 legs of size 1.4×1.4×1.5mm can be obtained from Bi_2Te_3 based materials during 8 hours.

The accuracy of cutting legs of size 1.4×1.4mm is ±0.02mm. The distribution of deviation from given size is given in Fig. 8.

For work in laboratory conditions it is reasonable to use a small-size desktop machine Altec - 13009, where productivity is of little significance, with a possibility of using two methods of cutting with bound and free abrasive (Fig. 9).

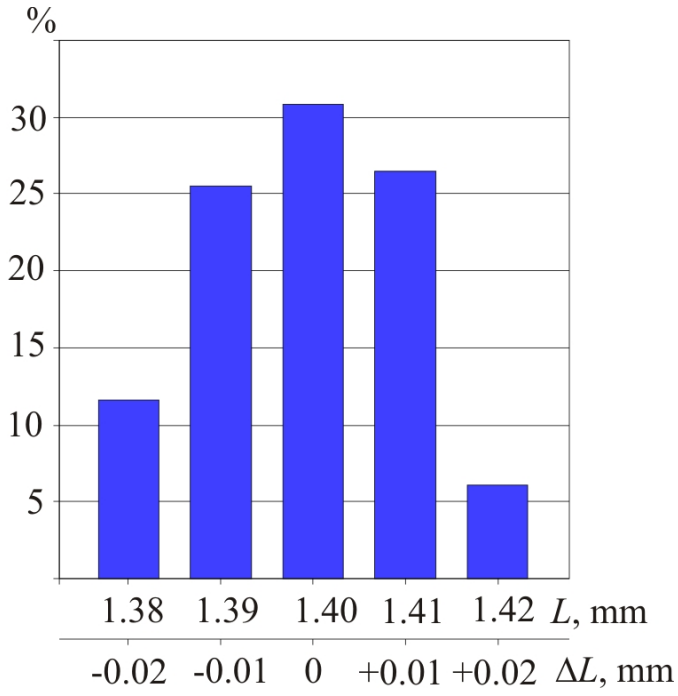

Fig. 8. Distribution of leg size deviation.

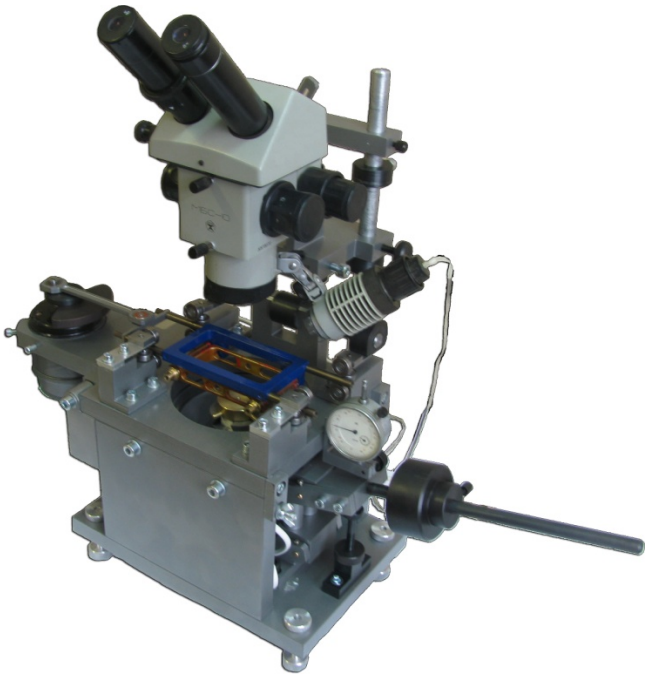

Fig. 9. Compact desktop machine Altec - 13009.

Plain bearings of carriage guides assure the accuracy and ease of their reciprocal movement.

Table 3

Main technical data and specifications of Altec – 13009 machine

1	Maximum dimensions of billet to be cut, mm	40×40×15
2	Number of wires ∅ 0.14 on a frame minimum, pcs.	1
3	Number of wires ∅ 0.14 on a frame maximum, pcs.	95
4	Cut width with a bound diamond coating, mm	0.22
5	Cut width with a free abrasive, mm	0.15
6	Weight, kg, not more	30
7	Electric power requirement, W	60
8	Supply voltage, V	14
9	Dimensions, mm	340×690×630

Small-size desktop machine is easy-to-use, energy efficient and does not require high materials costs.

Conclusions

Wire cutting machines, specially elaborated for cutting of thermoelectric materials, are an optimal tool for processing of alloys based on bismuth telluride. They assure high productivity, required cutting precision, minimum depth of damaged layer and low cost of cutting process.

References

1. L.I.Anatychuk, *Thermoelements and Thermoelectric Devices* (Kyiv, Naukova Dumka, 1979), 768 p.
2. A.B.Kamnev, B.A.Lapshinov, *Mechanical Treatment of Semiconductor Materials* (Moscow, 1990).
3. V.V.Nimchuk, S.F.Zaparov, and A.V.Satygo, High-Productivity Machine for Cutting of Thermoelectric Materials, *J.Thermoelectricity* **1**, 57-63 (2008).
4. Machine for Cutting of Semiconductor Materials Altec 13005 M. Leaflet.

Submitted 17.07.2014.

L.I. Anatychuk

L.I. Anatychuk, V.V. Lysko
Institute of Thermoelectricity NAS and MES of Ukraine 1, Nauky Str., Chernivtsi, 58029, Ukraine

V.V. Lysko

INCREASING THE RAPIDITY OF THERMAL CONDUCTIVITY MEASUREMENT BY THE ABSOLUTE METHOD

The results of computer investigations of the rapidity of thermal conductivity measurement by the absolute method are presented. Measurement errors caused by deviations from a linear distribution of temperature in the observable sample under the steady-state conditions have been analyzed. It has been established that in order to reach the acceptable values of these errors, measurement procedure must take a good deal of time, namely 10-15 hours to measure the temperature dependence of one sample. Methods for increasing the rapidity of reaching the steady state by the system have been developed. It has been established that alternating current passed through the sample under study permits to increase measurement rapidity by a factor of 3-5 due to accelerated heating of the sample central part by the Joule heat. Further increase of measurement rapidity can be achieved with a forced heating of the sample hot side by a reference heater. A combination of these two methods allows increasing measurement rapidity up to 8-10 times.

Key words: thermal conductivity, measurement error, rapidity, absolute method.

Introduction

General characterization of the problem. The efficiency of thermoelectric materials is the main efficiency factor of thermoelectric power converters. The success in technology and material research of thermoelectric materials is primarily dependent on clear correlation between the thermoelectric properties of materials and the technological features of their production. Finding this correlation is first and foremost dependent on the accuracy of measurement of the electric conductivity, thermopower and thermal conductivity of materials in given temperature range, as long as the results of impact on the substance can prove to be less than measurement error.

The most complicated process is thermal conductivity measurement over a wide temperature range. According to the analysis of the literature, the most consistent results can be obtained when thermal conductivity is measured by the absolute method [1-6]. Moreover, this method allows simultaneous measurement of thermopower and thermal conductivity, hence the thermoelectric figure of merit of material.

The use of the absolute method entails a problem of measurement rapidity. The necessity of reaching the steady-state conditions makes the measurements long-term, namely it takes 10-15 hours to measure the temperature dependence of one sample in the temperature range of 30 – 500 °C. In so doing, deviations from the steady state of experiment are an important factor that can affect the accuracy of thermal conductivity measurement. Deviations from the linearity of temperature distribution in the sample under study that occur in the process of reaching the steady state can serve the sources of errors in the determination of temperature difference on the sample ΔT, hence sample thermal conductivity

$$\kappa = \frac{Q}{\Delta T}\frac{l}{S}, \tag{1}$$

where Q is thermal power passed through the sample, l is the sample length, S is the sample cross-sectional area.

The purpose of this work is to develop methods for increasing measurement rapidity with the assured accuracy level.

Physical and mathematical models

A sample under study of length l and diameter d is fixed with one side to thermostat, as illustrated in Fig. 1. Thermostat temperature is T_0. Thermal power Q_0 from the sample heater is supplied to the other side of the sample whereby, upon reaching the steady state, temperature $T_г$ must be set on the sample hot side

$$T_г = T_0 + \frac{Q_0}{\kappa}\frac{l}{S}.$$

The lateral surface of the sample is adiabatically isolated.

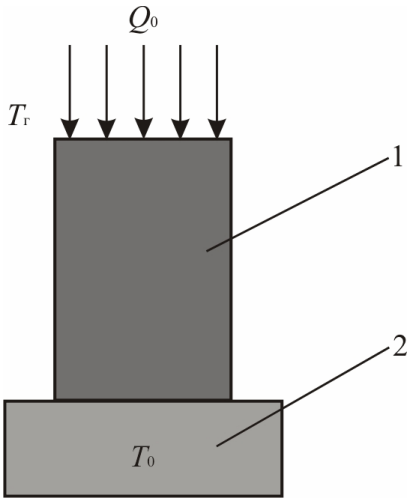

Fig. 1. Schematic of thermal conductivity measurement by the absolute method.
1 – sample under study, 2 – thermostat.

Temperature distribution in the sample upon actuation of the heater will change with time and depend on the sample properties, namely thermal conductivity κ, specific heat C and its geometric dimensions. To find this distribution at any point of the time, it is necessary to solve the unsteady-state thermal conductivity equation

$$\rho C\frac{\partial T}{\partial t} + \nabla\left(-\kappa\nabla T\right) = 0 \tag{2}$$

with the following boundary conditions:

– the sample cold side is thermostated at temperature T_0:

$$T = T_0,$$

– time-invariant thermal flux Q_0:is fed to the sample hot side

$$\boldsymbol{n}\cdot\boldsymbol{q}=\frac{Q_0}{S},$$

– the lateral surface of the sample is adiabatically isolated:

$$\boldsymbol{n}\cdot\boldsymbol{q}=0.$$

Results of investigation of measurement rapidity

To estimate the time necessary for the conduct of measurements whereby the steady-state experimental conditions are assured, it is necessary to study the effect of deviations from steadiness on measurement precision.

Time dependences of temperature distributions in the sample under study in the process of reaching the steady state by the system were obtained. Calculations were performed for a sample of *Bi-Te* based thermoelectric material of dimensions typical for thermal conductivity measurement by the absolute method – length 12 mm and diameter 8 mm. Sample thermal conductivity was 1.4 W/(m·K), heat capacity was 154 J/(kg·K). Thermostat temperature was 300 K. The heat capacity of sample heater was disregarded. If necessary, these results can be reproduced for other temperature ranges and sample dimensions.

Fig. 2 shows temperature distributions along the sample for different times of reaching the steady state by the system. It is seen that these distributions are nonlinear.

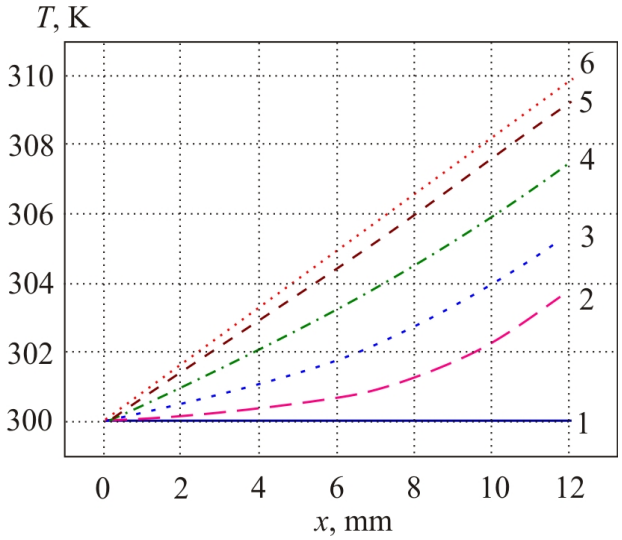

Fig. 2. Variation with time of temperature distributions along the sample
1 – 0 s, 2 – 15 s, 3 – 30 s, 4 – 60 s, 5 – 120 s, 6 – 240 s.

Deviations from the linear distribution are shown in Figs. 3 and 4. Percentagewise, the greatest deviations from the linearity will be close to thermostat. Hence, reaching the steady state by the sample hot side (sample heater) cannot serve as a guideline for the beginning of thermal conductivity measurement. This is seen in more detail in Figs. 5 and 6, showing a change in the sample hot side temperature with time and a deviation from the linear distribution of temperature along the sample at the time moment when a deviation from the expected temperature value on the sample hot side is 1% (for this case t = 224 s).

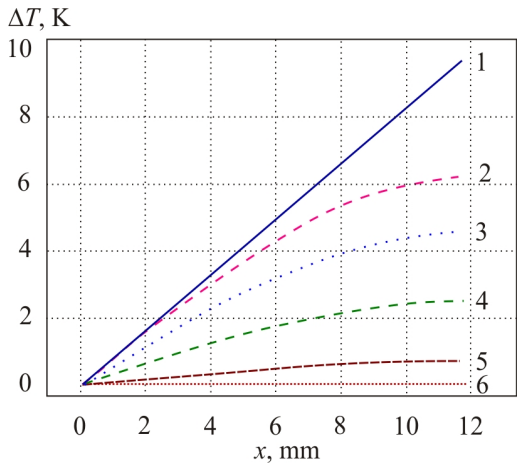

Fig. 3. Deviations from the linearity of temperature distribution along the sample upon reaching the steady state 1 – 0 s, 2 – 15 s, 3 – 30 s, 4 – 60 s,5 – 120 s, 6 – 240 s.

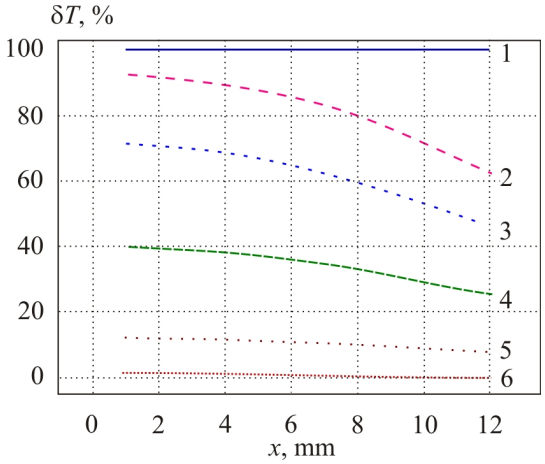

Fig. 4. Relative deviations from the linearity of temperature distribution along the sample upon reaching the steady state 1 – 0 s, 2 – 15 s, 3 – 30 s, 4 – 60 s,5 – 120 s, 6 – 240 s.

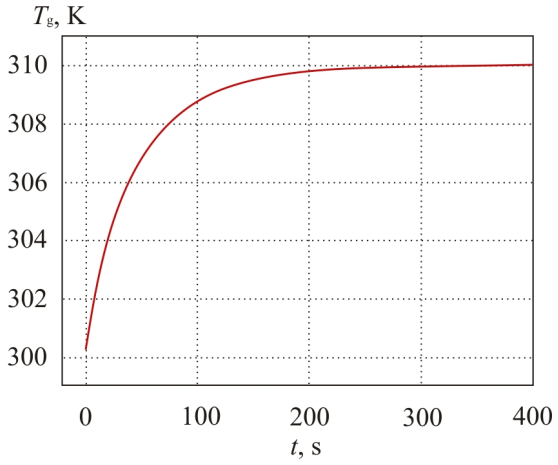

Fig. 5. Time history of the sample hot side temperature

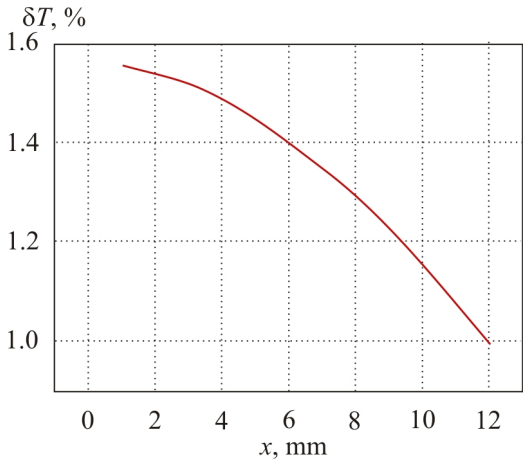

Fig. 6. Deviation from the linearity of temperature distribution along the sample (at the point of time when deviation from the steady state on the sample hot side is 1%)

Dependence of the error in thermal conductivity measurement on deviations of the sample hot side temperature from given value is shown in Fig. 7 (when measuring thermocouples are spaced 5 mm on the lateral surface of the sample).

Fig. 8 shows time dependences of the error in thermal conductivity determination, as well as the rapidity of change in the hot side temperature of the sample. A dependence of the error in thermal conductivity measurement on the rapidity of change in the hot side sample temperature is shown in Fig. 9. This dependence can serve the basis for determination of the moment of reaching the steady state by the system. Thus, for instance, to reach an error in thermal conductivity measurement less than 0.5% due to deviations from the steady state, one should wait for the time upon actuation of the heater, when the hot side temperature of the sample will change slower than 0.05 K/min.

The necessity of assuring the steady-state experimentation conditions brings up an important point of measurement rapidity. Fig. 10 shows a dependence of time t_0, during which maximum deviation from given linear temperature distribution will reduce to 1%, on the sample length.

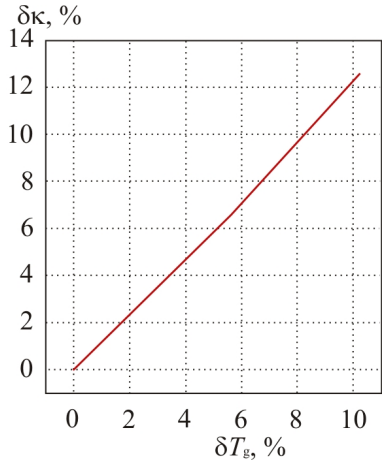

Fig. 7. Dependence of the error in determination of thermal conductivity on the accuracy of temperature stabilization on the sample hot side

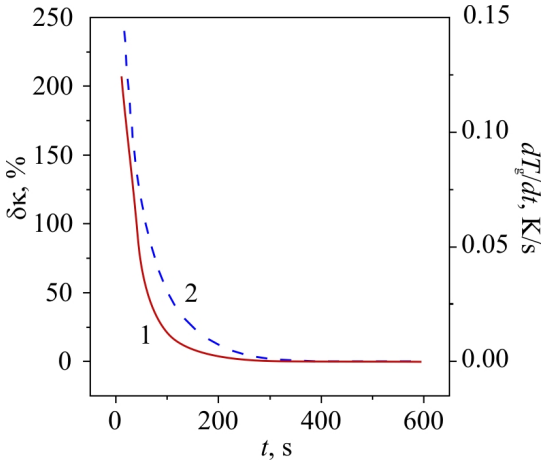

Fig. 8. Time dependences of the error in determination of thermal conductivity (1) and the rapidity of change in the hot side sample temperature (2) in the process of reaching the steady state

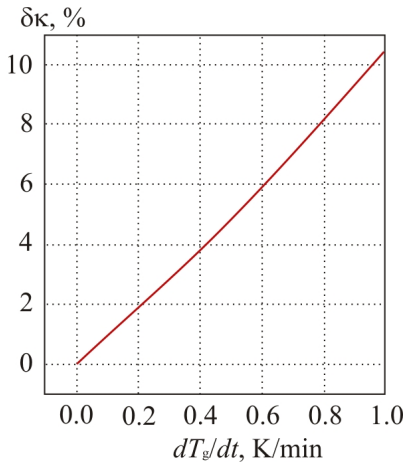

Fig. 9. Dependence of the error in determination of thermal conductivity on the rapidity of change in the sample hot side temperature upon reaching the steady state

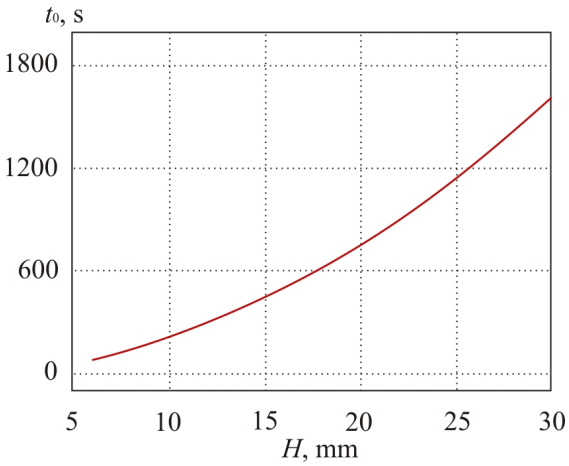

Fig. 10. Dependence of the time of reaching the steady state on the sample length

One of the variants of increasing measurement rapidity can be temporary passage of alternating current through the sample. This will accelerate heating of the central sample part due to release of the Joule heat in its bulk. Temperature distributions in the sample were studied for the case when during the initial period upon actuation of the heater an alternating current of given value is passed through the sample for some time. Thus, for instance, if during the first 30 s current 15 A is passed through the sample, then already at time instant t_0 = 96 s maximum deviation from the linear distribution will be less than 1%. These results testify that temperature distribution along the sample can reach the steady state 3 times faster compared to the case when no current is passed through the sample.

Measurement rapidity can be further increased when, alongside with alternating current passed through the sample, forced heating of the hot side of the sample is used at the initial moment upon actuation of the heater. Fig. 11 shows one of the partial cases of using this method of rapidity increase. Temperature distributions in the sample for this case are shown in Fig. 12. The time it takes for maximum deviation from the linear distribution to be within 1% is 38 s, suggesting the possibility of rapidity increase by a factor of 8-10.

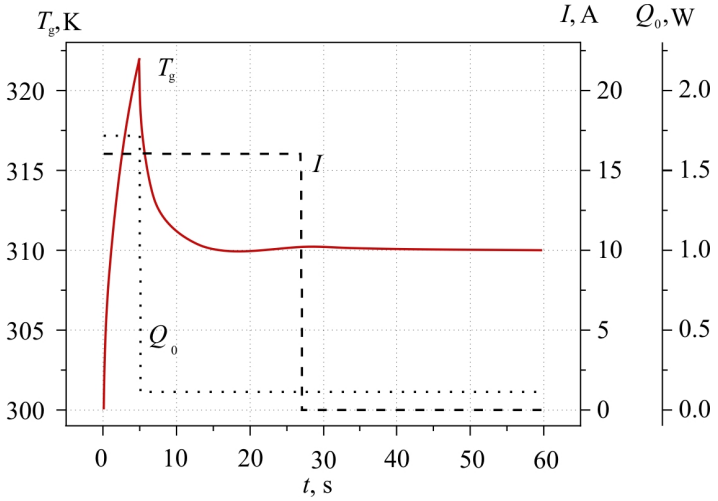

Fig. 11. Time dependences of the sample hot side temperature, current through the sample and heater power for the case of alternating current flow through the sample and forced heating of its hot side.

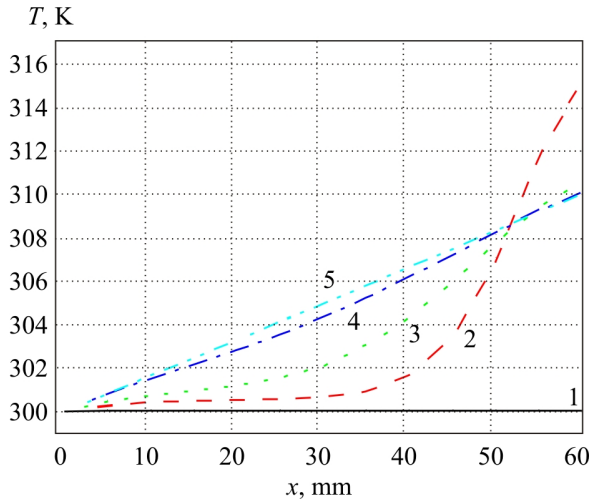

Fig. 12. Variation with time of temperature distributions along the sample for the case of alternating current flow through the sample and forced heating of its hot side. 1 – 0 s, 2 – 6 s, 3 – 12 s, 4 – 24 s, 5 – 48 s.

The above investigations serve the basis for the development of increased rapidity measuring installation which permits to expand the possibilities of using the absolute method of measurement, especially when determining the properties of large-size samples.

Conclusions

1. It has been established that a deviation of the sample hot side temperature from the given value cannot serve a criterion of reaching the steady state by the system, as long as inside the sample in this case there will be a deviation from linearity.
2. Dependences of the errors in determination of sample thermal conductivity on time in the process of reaching the steady state, as well as on deviation from the expected value of the sample hot side temperature have been obtained. It has been established that the error in determination of thermal conductivity exceeds by 20% a relative deviation from the expected value of the sample hot side temperature.
3. A method for increasing the rapidity of reaching the steady state by the system has been developed. It has been established that temporary passage of alternating current through the sample under study allows increasing measurement rapidity by a factor of 3 - 5, and in combination with forced heating of the sample hot side – by a factor of 10.

References

1. L.I.Anatychuk, Thermoelements and Thermoelectric Devices (Kyiv: Naukova Dumka, 1978).
2. A.S.Okhotin, A.S.Pushkarsky, R.P.Borovikova et al., Methods for Measuring Characteristics of Thermoelectric Materials and Converters (Nauka, Moscow, 1974).
3. J.P.Moore, R.K.Williams and R.S.Graves, Precision Measurement of the Thermal Conductivity, Electrical Resistivity, and Seebeek Coefficient from 80 to 400 K and Their Application to Pure Molybdenum, Rev. Sci. Instrum **45**(1), 87-95 (1974).
4. L.I.Anatychuk, S.V.Pervozvansky, and V.V.Razinkov, Precise Measurement of Cooling Thermoelectric Material Parameters: Methods, Arrangements and Procedures, Proc. of the 12th Intern. Conf. Thermoelectrics, Japan, 1993, p.p. 553-564.
5. L.I.Anatychuk, M.V.Havrylyuk, V.V.Lysko, Installation for Measuring Properties of Semiconductor Thermoelectric Materials, J.Thermoelectricity. – 2010. – № 3. P. 41-49.
6. L.I.Anatychuk, V.V.Lysko, Investigation of the Effect of Radiation on the Precision of Thermal Conductivity Measurement by the Absolute Method, J.Thermoelectricity. 2012. – № 1. – P. 65-73.

Submitted 03.11.2014.

NEWS
OF INTERNATIONAL THERMOELECTRIC ACADEMY

LYUDMYLA MYKOLAIVNA VIKHOR

(Dedicated to 60th anniversary)

December 26, 2014 is the date of 60-th anniversary of Lyudmyla Mykolaivna Vikhor, corresponding member of the International Thermoelectric Academy, Doctor of Science in Physics and Mathematics, chief research scientist of Institute of Thermoelectricity of the National Academy of Sciences and Ministry of Education and Science of Ukraine, a well-known specialist in thermoelectric cooling and electric energy generation.

Lyudmyla Mykolaivna Vikhor was born in Kolomyia, Ivano-Frankivsk region (Ukraine) in the family of public officials. Having finished secondary general school, she entered the Faculty of Physics and Mathematics of Chernivtsi State University (1972), Department of thermoelectricity and physical metrology) that she graduated in 1977 in the major "Physics, teacher of physics". On graduation from the post-graduate course, in 1981 she defended PhD thesis in the specialty "Physics of semiconductors and dielectrics" done in the Basic Research Laboratory of Chernivtsi University guided by Prof.A.G.Samoilovich, honoured worker of science of the USSR.

In 1980-83 she worked as a junior research scientist in Basic Research Laboratory of Chernivtsi University, and in 1984-1990 – as a senior engineer of "Phonon" Design Bureau in the department responsible for the development of thermoelectric coolers.

Since 1991 L.M.Vikhor has worked at the Institute of Thermoelectricity of the National Academy of Sciences and Ministry of Education of Ukraine and occupied positions of senior research scientist, leading research scientist, chief scientific scientist, and sector leader. Concurrently, she has been teaching at the Department of Thermoelectricity of Chernivtsi National University.

In 2007, before the members of the Academic board of Institute of Thermoelectricity she defended her doctoral thesis in the specialty "Physics of devices, elements and systems" on the subject "Theory of functionally graded thermoelements and modules on their basis". The research advisor of the thesis was L.I.Anatychuk, academician of the NAS of Ukraine.

The academic career of L.M.Vikhor includes such research priorities as theory of semiconductors, theoretical aspects of heat and current transport phenomena, theory of thermoelectric coolers and generators and devices on their basis, elements of optimal control theory and their application for optimization problems of thermoelectric devices, some of the aspects of theory of thermoelectric material science.

Lyudmila Mykolaivna is a co-author of the monograph "L.I.Anatychuk, L.M.Vikhor, Functionally-Graded Thermoelectric Materials (2012), as well as of the chapter "L.M.Vikhor, L.I.Anatychuk, V.Ya.Mikhailovsky, L.T.Strutynska, Innovations in Organic-Fueled Thermoelectric Generators Development" in the book "Thermoelectric Power", Ed. by William P. Dempsey, Nova Science Publishers Inc., N.Y.

L.M.Vikhor is the author of more than 90 scientific publications in leading home and foreign periodicals and international conference proceedings. She is the author of 8 patents of Ukraine, science editor of "Journal of Thermoelectricity".

For achievements in work Lyudmyla Mykolaivna was awarded with the honorary certificate of the Presidium and Central trade union committee of the National Academy of Sciences of Ukraine (2008), as well as with the honorary certificate of Chernivtsi regional council (2009).

International Thermoelectric Academy, Institute of Thermoelectricity, "Journal of Thermoelectricity" Editorial Board sincerely greet the esteemed Lyudmyla Mykolaivna Vikhor on her 60^{th} jubilee and wish her sound health, new progress in work, happiness and abundance.

ARTICLE PREPARATION RULES

The article shall conform to the journal profile. The article content shall be legible, concise and have no repetitions.

The article shall be submitted to the editorial board in electronic version.

The text shall be typed in text editor not lower than MS Word 6.0/7.0.

Page setup: "mirror margins"- top margin – 2.5 cm, bottom margin – 2.0 cm, inside – 2.0 cm, outside– 3.0 cm, from the edge to page header – 1.27 cm, page footer – 1.27 cm.

Graphic materials, pictures shall be submitted in color or, as an exception, black and white, in .opj or .cdr formats, .jpg or .tif formats being also permissible. According to author's choice, the tables and partially the text can be also in color.

The article shall be submitted in English on A4 paper sheets; the number of pages shall not exceed 12. By agreement with the editorial board, the number of pages can be increased.

To accelerate publication of the article, please adhere to the following rules:

- the authors' initials and names are arranged in the centre of the first page at the distance of 1 cm from the page header, font Times New Roman, size 12 pt, line spacing 1.2;
- the name of organization, address (street, city, postal code, country) – indent 1 cm below the authors' initials and names, font Times New Roman, size 11 pt, line spacing 1.2, center alignment;
- the title of the article is arranged 1 cm below the name of organization, in capital letters, semi-bold, font New Roman, size 12 pt, line spacing 1.2, center alignment. The title of the article shall be concrete and possibly concise;
- the abstract is arranged 1 cm below the title of the article, font Times New Roman, size 10 pt, in italics, line spacing 1.2 ,center alignment;
- key words are arranged below the abstract, font Times New Roman, size 10 pt, line spacing 1.2, justified alignment. The title "Key words" – font Times New Roman, size 10 pt, semi-bold;
- the main text of the article is arranged 1 cm below the abstract, indent 1 cm, font Times New Roman. size 11 pt, line spacing 1.2, justified alignment;
- formulae are typed in formula editor, fonts Symbol, Times New Roman. Font size is "normal" – 12 pt, "large index" – 7 pt, "small index" – 5 pt, "large symbol" – 18 pt, "small symbol" – 12 pt). The formula is arranged in the text, centre aligned and shall not occupy more than 5/6 of the line width, formulae are numbered in round brackets right;
- dimensions of all quantities used in the article are represented in the International System of Units (SI) with the explication of the symbols employed;
- figures are arranged in the text. The figures and pictures shall be clear and contrast; the plot axes – parallel to sheet edges, thus eliminating possible displacement of angles in scaling;
- tables are arranged in the text. The width of the table shall be 1 cm less than the line width. Above the table its ordinary number is indicated, right alignment. Continuous table numbering throughout the text. The title of the table is arranged below its number, center alignment;
- references should appear at the end of the manuscript. References within the text should be enclosed in square brackets. References should be numbered in order of first appearance in the text. Examples of various reference types are given below.

– L.I. Anatychuk, *Thermoelements and Thermoelectric Devices: Handbook* (Kyiv: Naukova Dumka, 1979), p.766. (Book)
– T.M. Tritt, Thermoelectric Phenomena, Materials, and Applications, *Annual Review of Materials Research* **41**, 433 (2011). (Journal paper)
– U. Ghoshal, *Proceedings of the XXI International Conference on Thermoelectrics* (N.Y., USA, 2002), p. 540. (Proceedings Conference)

The article should be supplemented by:

• letter from the organization where the work was performed or from the authors of the work applying for the publication of the article;

• information on the author (authors): last name and initials; full name and postal address of the institution where the author works; academic degree; position; telephone number; E-mail;

• author's (authors') photo in color or, as an exception, in black and white. With the number of authors more than two their photos are not given;

• author's application to the following effect:

We, the undersigned authors, … transfer to the founders and editors of "Journal of Thermoelectricity" the right to publish the article…in Ukrainian, Russian and English. This is to confirm that the present publication does not violate the copyright of other persons or organizations.

Date Signatures

Below is given an example of article preparation.

Author's photo 3 × 4 cm

A.I. Casian[1], B.M. Gorelov[2]

[1]Technical University of Moldova,
168, Stefan cel Mare Ave.,
Chisinau, MD-2004, Moldova;
[2]Institute of Surface Chemistry of National Academy
of Sciences of Ukraine, 17, Gen. Naumov Str.,
Kyiv, 03164, Ukraine

Author's photo 3 × 4 cm

STATE OF THE ART AND PROSPECTS OF THERMOELECTRICITY ON ORGANIC MATERIALS

The aim of the paper is to analyze the expected thermoelectric opportunities of organic materials, including some highly conducting quasi-one-dimensional crystals. It is shown that interest of investigators in these materials has been growing recently. Quasi-one-dimensional organic crystals have high prospects for thermoelectric applications. These materials combine the properties of multi-component systems with more diverse internal interactions and of quasi-one-dimensional quantum wires with increased density of electronic states. It is shown that the values of the thermoelectric figure of merit ZT ~ 1.3 – 1.6 at room temperature are expected in really existing organic crystals of tetrathiotetracene-iodide, TTT_2I_3, if the crystal parameters are approaching the optimal ones.

Key words: thermoelectricity, tetrathiotetracene-iodide, polarizability.

Introduction

It is known that conducting organic materials usually have much lower thermal conductivity than the inorganic materials. Moreover, the organic materials can be fabricated by simpler chemical methods, and it is expected that such materials will be less expensive in comparison with the inorganic ones. Exactly these properties attracted attention to such materials for the use in thermoelectric (TE) applications long time ago [1, 2]. In spite of relatively high value of the thermoelectric figure of merit $ZT = 0.15$ at room temperature observed in polycopper phthalocyanine [2] as early as 1980, the thermoelectric properties of organic materials are still weakly investigated. This situation has the only explanation that thermoelectricians are still weakly interested in organic materials, and organic chemists are also weakly interested in thermoelectric materials. Moreover, in order to seek good organic thermoelectrics, it is necessary to organize multidisciplinary consortiums of physicists, organic chemists and engineers in the field of thermoelectricity. …

The aim of this paper is to present briefly the state-of-the-art of investigations in the area of new organic thermoelectric materials and to describe the nearest expected results for really existing quasi-one-dimensional organic crystals of tetrathiotetracene-iodide, TTT_2I_3.

Quasi-one-dimensional organic crystals of TTT_2I_3

The structure of quasi-one-dimensional organic crystals of tetrathiotetracene-iodide, TTT_2I_3, has been briefly described in [34]. These needle-like crystals are formed of segregate chains or stacks of planar molecules of tetrathiotetracene *TTT*, and iodine ions. The chemical compound TTT_2I_3 is of mixed-valence: two molecules of *TTT* give one electron to the iodine chain which is formed from I_3^- ions. The

conductivity of iodine chains is negligibly small, so that only *TTT* chains are electrically conductive and holes serve as carriers. The electrical conductivity σ along *TTT* chains at room temperature varies between 10^3 and $10^4\ \Omega^{-1}\text{cm}^{-1}$ for crystals grown by gas phase method [35], and between 800 and $1800\ \Omega^{-1}\text{cm}^{-1}$ for crystals grown from solution [36]. Thus, the conductivity is very sensitive to crystal impurity and perfection which depends on growth method. In the direction perpendicular to chains σ is by three orders of magnitude smaller than in the longitudinal direction and is neglected. …

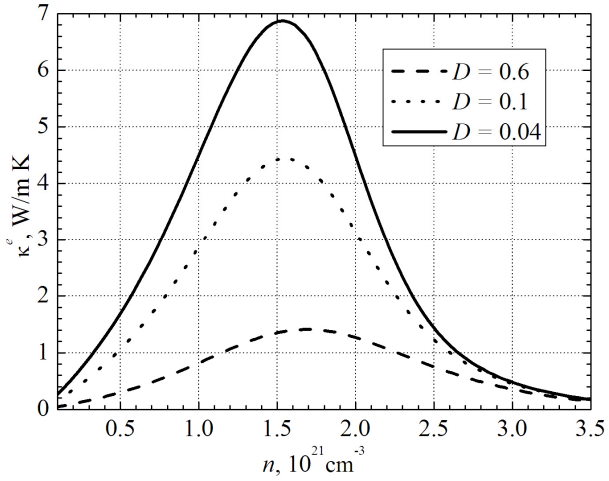

Fig. 1. Dependences of electron thermal conductivity κ^e on n.

$$\sigma = R_0,\ S = R_1 / eTR_0,\ \kappa^e = \left(e^2T\right)^{-1}\left(R_2 - R_1^2 / R_0\right), \tag{1}$$

Thermoelectric properties

Expressions (2) – (3) have been calculated in order to determine the thermoelectric properties of quasi-one-dimensional organic crystals of TTT_2I_3 with different degrees of purity….

Conclusions

The state-of-the-art of research on new organic materials for thermoelectric applications is analyzed. It is shown that the interest of investigators in these materials has been growing in recent years. The highest value of $ZT \sim 0.38$ at room temperature has been measured in doped acetylene, with the only problem that this material is not stable. Accurate control of the oxidation level in poly (3, 4-ethylenedioxythiophene) (PEDOT) gave the power factor $324\ \mu\text{W}\cdot\text{m}^{-1}\text{K}^{-2}$ and in combination with its low intrinsic thermal conductivity ($\kappa = 0.37\ \text{W}\cdot\text{m}^{-1}\text{K}^{-1}$) yielded $ZT = 0.25$ at room temperature, and this material is air-stable….

References

1. Ali Shakouri, Recent Developments in Semiconductor Thermoelectric Physics and Materials, *Annu.Rev.Mater.Res*.**41**, 399-431 (2011).
2. L.I. Anatychuk, *Thermoelectricity, Vol.2, Thermoelectric Power Converters* (Kyiv, Chernivtsi: Institute of Thermoelectricity, 2003), 376p.
3. M.E. Bengen, *German Patent Appl*. OZ 123, 438, 1940; *German Patent* 869,070, 1953, Tech. Oil Mission Reel, 143,135, 1946.